The fluid mechanics of convection and diffusion in medical devices for visualization in arteries and clearing of urea in hemodialysis. Analysis, design, and optimization via CFD and experimental analysis

Syed Faisal

A dissertation

submitted in partial fulfillment of the

requirements for the degree of

Doctor of Philosophy

University of Washington

2022

Reading Committee:

Alberto Aliseda, Chair

Eric Seibel

James J. Riley

Program Authorized to Offer Degree:

Mechanical Engineering

University of Washington

Abstract

The fluid mechanics of convection and diffusion in medical devices for visualization in arteries and clearing of urea in hemodialysis. Analysis, design, and optimization via CFD and experimental analysis

Syed Faisal

Chair of the Supervisory Committee:

Dr. Alberto Aliseda

Mechanical Engineering

This thesis explores the understanding of convection and diffusion transport mechanisms in medical devices. The specific goals for this thesis is understanding the fluid mechanics of two different biomedical systems – visualization in the cardiovascular system and urea removal in hemodialysis. This study investigates the fluid dynamics of saline flushing in endovascular catheters used in the treatment and diagnosis of atherosclerotic plaque in arteries. This section of the thesis focuses on the convection-dominated physics, which are observed during saline flushing. The process involves saline injection, mixing with blood, and advection of the mixture away from the region of interest to provide a clear optical path for imaging. The objective of the study is to achieve clearance in the artery for optical imaging without the use of a balloon occlusion to obstruct antegrade flow into the imaging region of the artery. Computational fluid simulations (CFD) simulations are used as a rapid turn-around tool for the understanding of the influence of different parameters on the flow process that control the transport and mixing of saline and blood, leading to an evolutionary design process of an endovascular catheter that combines imaging

forward-viewing element with saline flushing lumens. A novel design and control technique is developed that provides the method to regulate the pressure in a blocked artery during saline flushing, so only small deviations from physiological pressure are exerted on the damaged artery wall, minimizing risk of rupture. In vitro experiments carried out saline flushing to achieve optical clearing in phantoms simulating chronic total occlusions in coronary arteries, as well as in partially occluded coronary arteries with an opaque blood surrogate. Different plaque-catheter configurations, including plaque size, distance from the catheter, injection flow rates and orientation of the catheter with respect to the plaque and occlusions near bifurcations, are studied via CFD. An additional optical ray analysis provides confirmation of the clearing of the artery occluded by plaque. A new catheter design is demonstrated to produce optical clearing via saline flushing, leading safely and effectively to a clear optical imaging field, and an improved technique is outlined that overcomes some practical challenges and limitations commonly encountered in angioscopy.

The second part of this thesis investigates the fluid physics of urea transport in photo-catalytic urea oxidation channels, for portable hemodialysis in kidney disease patients. This section of the thesis focuses on inducing mixing at low Reynolds numbers to overcome the diffusion-limited urea transport from the bulk dialysate flow in the channels to the catalyst surface. The study is inspired by recent advancements in photo-electrochemical oxidation of urea by TiO_2. A numerical CFD model is used to analyze the impact of the design and operational parameters on the performance of the dialysis system. This involved a grid independence study to resolve the high Peclet number transport of urea and different models to represent the oxidation of urea and its effect of urea transport to the catalyst surface. Innovative channel designs (thin channel, wavy channel and

chevron channel) were studied for performance, and their metrics compared to improve dialysis efficiency, contributing to the development of novel wearable dialysis devices.

TABLE OF CONTENTS

Page

LIST OF FIGURES

diffusion coefficient, primarily influenced by the concentration. The three values for the diffusion reported different results as seen in the longitudinal section view of the first couple mm of the channel (b), where the urea concentration is dramatically different and the subsequent daily urea removal rates are different (c). The variable diffusion coefficient model is selected for future investigation, despite the increase in computational cost.

8.6 Influence of urea removal rate. 101

9.1 The splitting in the inlet manifold causes the dialysate to prefer some channels over others leading to different flow rates in different channels. As the flow rate reduces from (a) 250 mL/min, (b) 150 mL/min, and (c) 100 mL/min, the inter-channel variations reduce. The inlets are smaller than the channel sizes leading to expansion of the flow as seen in the case of (d) 250 mL/min, where the fluid jumps as it expands, resulting in inefficient urea transfer. These regions reduce again as the flow rate decreases (e) 100 mL/min. The inlet/outlet manifold and channels need to be optimized to avoid such inefficiencies. 106

9.2 The pressure drop for 150 mL/min is about 30 Pa. This increases with increase flow rate. 108

9.3 As the flow rates are reduced to (a) 5.00 mL/min, (b) 3.10 mL/min and (c) 0.54 mL/min a uniform flow profile exists in the channel. The channels have minimal stagnation regions which are away from the TiO2 plates, showing an effective shape and design for the channels. 109

9.4 The mass fraction of urea at the mid plane (thickness/2) shows the free stream urea concentration (mass fraction of urea = 0.0006) persists at high flow rates (a) 5.0 mL/min and (b) 3.10 mL/min. In comparison, a nice decreasing concentration gradient of urea is seen at a flow rate of (c) 0.54 mL/min. 110

9.5 When the thickness of the panels is reduced from (a) 1 mm to (b) 0.5 mm, the free stream urea concentration (0.0006 mass fraction of urea) is brought closer to the TiO2 plate. This causes more reaction at the plate and a reduction in urea concentration through the flow. The effect is compounded when the flow rate 112

reduces (less concentration with low flow and low thickness) and shows a similar trend as the 1 mm channel.

ACKNOWLEDGMENTS

Alhamdullilah (all praises to God) for blessing me with this incredible opportunity and assisting me to learn and produce this work. Over the course of six wonderful years, I had the incredible opportunity to work with Dr. Alberto Aliseda, who took me under his tutelage for which I am deeply grateful. From helping me acclimatize with the education system in the United States of America, to teaching me industry standards employed in research, he has been invaluable as a mentor to me. I thank Dr. Eric Seibel, whose ingenious ideas and vision, created a platform for me to work and provided me with the opportunity that led to this research. I also thank Dr. James Riley for assisting me in my research as well as teaching me the tools I need for this work. Dr. Dana Dabiri has been an invaluable asset as my graduate school representative on my committee, cheering, supporting and providing his technical insight to complete this work. I am indebted to my wonderful parents who have been supporting me, blessing me with their wisdom, and helping me achieve everything in my life. My incredible wife, for her continuous love, patience, and support through every step of this work and being a source of welcoming joy during some of my arduous times. My family and friends who've helped me in my times of difficulty, for which I am grateful. I thank my peers and colleagues working in our lab, from whom I sought help and guidance in working on my thesis and my research and were always readily available for whenever I needed them.

DEDICATION

To my dear mother and father,

whose continuous sacrifice inspires me

to keep contributing to making a difference.

And to my loving wife, family and friends who helped me in achieving my dream.

PREFACE

Transport Phenomena in the human body

Convection and diffusion are two distinct transport phenomena that play key roles in the concentration of a biological molecule in blood or other biofluids of importance in human health. In convection, substances or particles are transported due to the bulk motion of the fluid and are directly affected by fluid velocity. Diffusion of substances occurs at a molecular level due to a gradient between regions of higher concentration regions and regions of lower concentration regions tending towards uniformizing the concentration field. In biological systems, both these phenomena occur in interaction with each another. Frequently, one dominates over the other and controls the concentration field. In the lungs, oxygen is brought in convectively by air entering our lungs and then diffuses into the blood stream through the alveoli. CO_2 transport in the lungs follows a similar convection-diffusion pathway in the lungs. Another example is urea removal, which is transported to the kidneys via convection and purification of blood takes place via diffusion into the glomeruli (specialized clusters that collect urea).

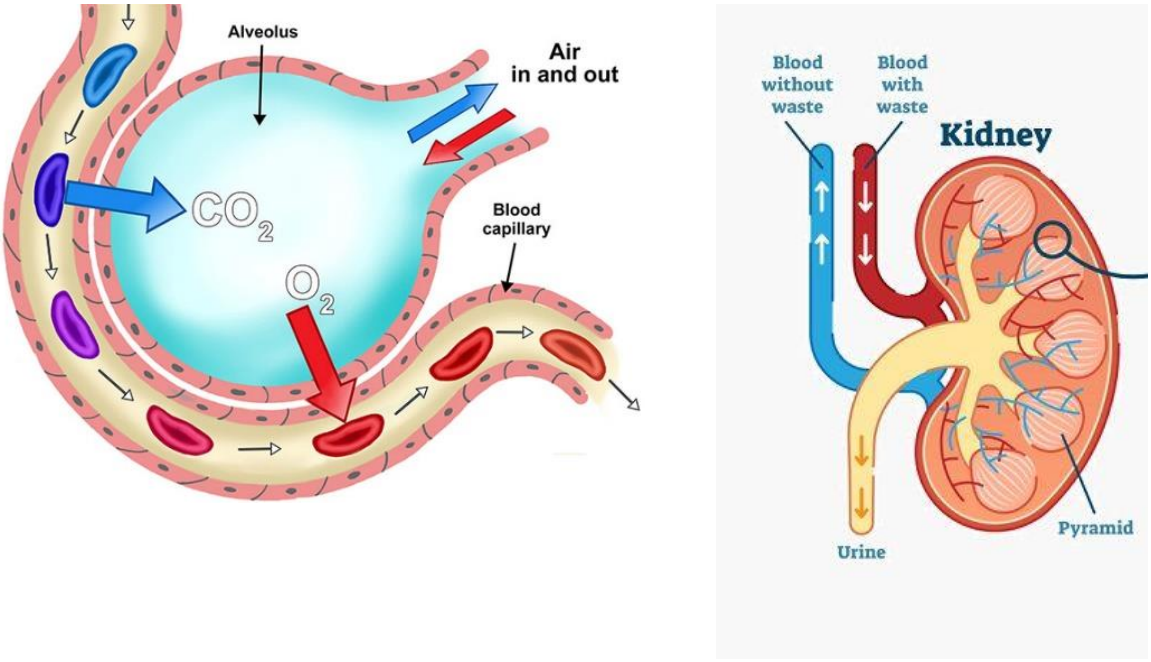

(a) *(b)*

Figure 1: (a) O_2 diffuses into the bloodstream while CO_2 diffuses out from the blood and are convective transported by blood and air, to other cells and outside of the human body, respectively. (b) Filtration of urea in the kidneys also involves both transport processes where urea enters the kidneys via convection due to the blood and diffuses into the kidneys to form urine.

Understanding these interacting phenomena, the fluid substrate and chemical species properties, and their effects in biological system enables the development of new and improved medical technologies that can capitalize on efficiently using these phenomena.

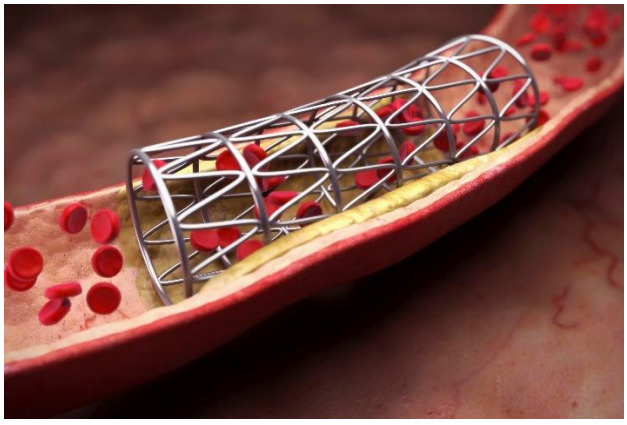

(a) *(b)*

Figure 2: Drug eluting stents (a) utilize the diffusion-convection phenomena where the drug diffuses into the blood and is convected away by blood. Dialysis systems are continuously looking to maximize diffusion of urea from blood to enable effective dialysis leading to better quality of life.

Thesis Outline

This thesis is divided into two major sections: Visualization of the interior of arteries via saline flushing incorporated in the optical fiber endoscope catheter, and the oxidation of urea in low Reynolds number (but high Peclet number) channels coated with a photocatalyst in the design of a portable hemodialysis machine.

The first part of this thesis investigates the physics of blood flows (hemodynamics) and its interaction with saline to dilute the red blood cells. Here, the process of convection dominates, and our study focuses on the mixing of saline with blood to provide a transparent optical medium to visualize the interior of the artery. The understanding obtained from this part of the study is used to design and develop a novel saline flushing system to obtain clear optical regions in arteries to image plaque. This enables clinicians to diagnose and treat cardiovascular disease.

In the second part of this thesis, the advection-diffusion of urea in dialysate (saline solution) is examined. As dialysate flows through urea-oxidizing elements, diffusion of urea limits the flux of urea that can be removed from dialysate and thus the performance of the dialysis system. The analysis of the fluid mechanics of the microchannels and the introduction of mixing through changes in the channel geometry are used to optimize urea oxidation from the dialysate

(intermediate working fluid that exchanges urea with blood before bringing it to the photo-catalytic oxidation channel to enable removal of urea from the body in the portable dialysis machine).

The thesis is divided in two parts, each with its own introduction, methods, results and discussion. The saline flushing in the cardiovascular system is described first, with the urea transport problem in the dialysis system described in the second part. Each result is presented individually and explained in the discussion. The conclusions are presented separately, with the limitations of the study at the end of each part. The references to all published literature are given at the end of the thesis.

Thesis Part 1:

Saline flushing of arteries for endoscopic imaging of plaque

Chapter 1

INTRODUCTION

1.1 Cardiovascular Disease

Cardiovascular disease occurs within the circulatory system of the human body, namely, the heart, blood vessels, and blood. With the global change in diet, nutrition, and exercise, cardiovascular disease continues to be a growing concern in societies, for both developed and developing countries. Over the past decade, cardiovascular disease has increased by 12.5% globally with atherosclerosis being the underlying cause for about 50% of all deaths.[1, 2] Cardiovascular disease continues to be the leading cause of death worldwide with mortality rates estimated to increase by thirty six percent by 2030.[3] The heart and blood vessels are affected by numerous problems, many of which are caused directly or indirectly by atherosclerosis. Atherosclerosis is an inflammatory disease where plaque deposits inside arteries, leading to reduced supply of blood to critical organs such as the heart. Over 600,000 Americans die due to atherosclerosis every year.[4-6]

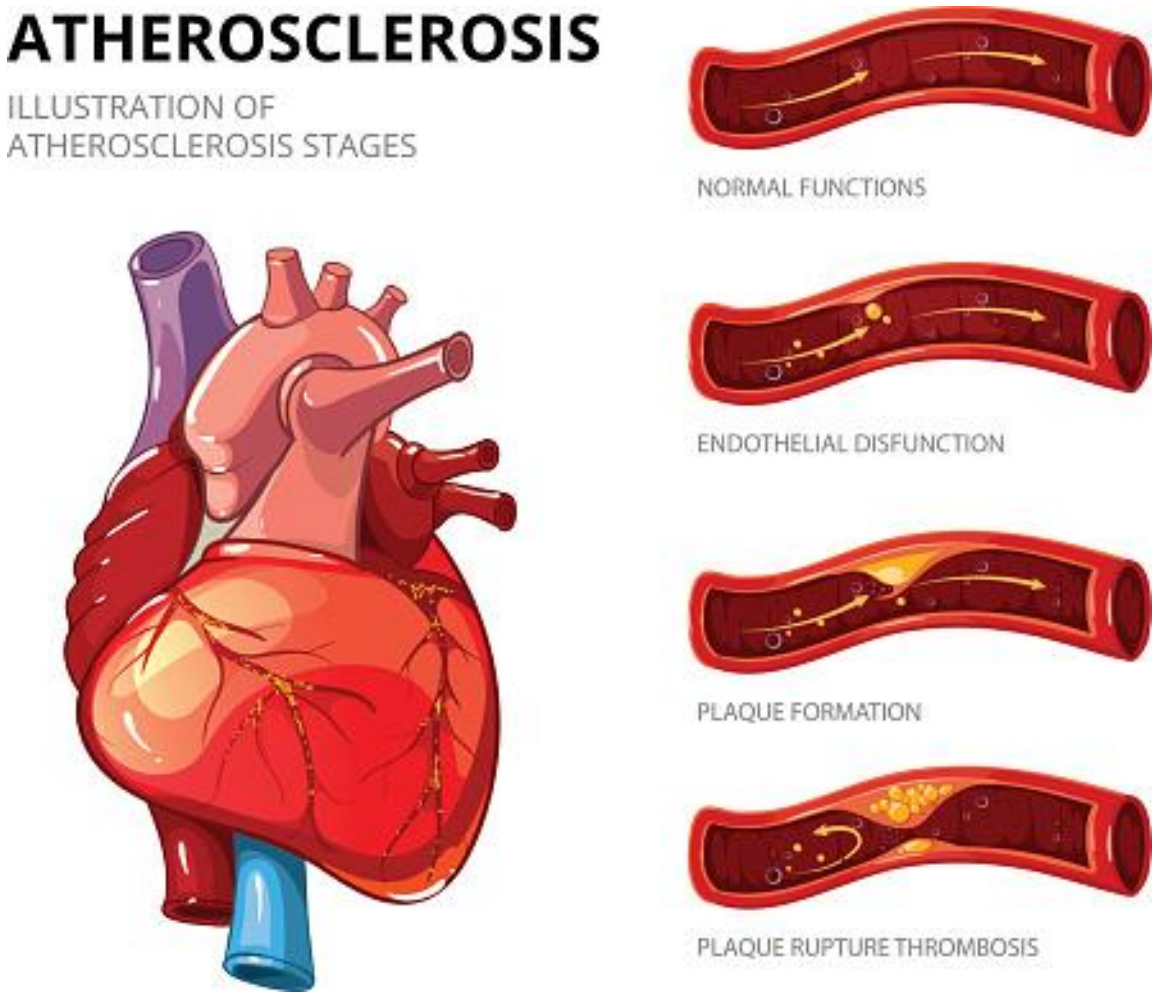

Figure 1.1: An illustration of the stages of atherosclerosis.

1.2 Partially occluded arteries and chronic total occlusion

In severe cases, the plaque development may continue within the weakened artery and result in complete blockage, with zero or little blood flow and the formation of a chronic total occlusion (CTO). Chronic total occlusions are primarily found in coronary arteries, which is a common site for atherosclerotic plaque to develop. Coronary arteries are the blood vessels that provide oxygen rich blood to the cardiac muscle to keep up the pumping action of the heart and whose etymology is derived from the crown like fitting around the heart. They originate from the cusp of the aortic

valve at the junction of the aorta and left ventricle. These total occlusions may exist in the coronary arteries for greater than three months.[7] Flow within the arteries beyond the occlusion may be TIMI 0 (Thrombolysis in Myocardial Infarction) where antegrade flow may be absent or TIMI 1 (a faint antegrade flow of blood).[8] It is not uncommon for multiple CTOs to be formed within the same individual which can result in angina (chest pain) or even a heart attack. It is suggested that around 19% of patients with coronary artery disease have one or more CTOs.[9]

1.3 Diagnosis and treatment of occlusions

State of the art imaging of atherosclerosis

Diagnosis of atherosclerosis is mainly divided into two: non-invasive and minimally invasive techniques. The current major diagnostic techniques include direct coronary angiography, coronary computed tomography angiography, and magnetic resonance imaging. Magnetic resonance imaging utilizes radio waves in an applied magnetic field to image the artery and the plaque without exposure to ionizing radiation.[57] However, MRI scans are time consuming, not widely available and sometimes unsafe for certain patients who have claustrophobia or implants.[57] In a direct coronary angiogram, contrast agent are utilized to highlight the flow of blood through the arteries when imaged via x-ray radiation. This is routinely performed globally and can even differentiate CTOs from high grade stenosis.[58] However, direct angiography is limited in defining the vessel morphology within the occluded (or in the occluded region) and coronary computed tomography angiography (CCTA) circumvents this. In CCTA, a fusion of computed tomography and x-ray technology along with contrast agent are used to image the occlusion. [58-60] CCTA uses more contrast agent - usually injected at the heart - than conventional direct angiography, and image acquisition is delayed for several seconds. Thus,

CCTA can image distal collateral vessels in addition to describing the vessel morphology within the plaque. Additionally, CCTA can help identify the extent of calcium in the plaque and its location. This results in better description of the CTO lesion morphology.[58, 59] However, CCTA does have low resolution (0.5-0.6 mm) and cannot distinguish CTOs from high-grade stenosis.

CCTA and direct angiography are the current gold standards used to identify plaque and coronary artery vessel wall. However, higher resolution images can be obtained via minimally invasive techniques which include optical coherence tomography (OCT), intravascular ultrasound (IVUS) and scanning fiber endoscopy (SFE).[57, 61] IVUS uses ultrasound to image arterial wall and provides a good description of the flow velocity inside the vessel. OCT is similar to IVUS but instead uses visible light imaging to define the arterial wall. Both of these imaging techniques are approved by the Federal Drug Administration (FDA) for diagnostic use. Another technique, NIRS-IVUS involves the synthesis of infra-red imaging and ultrasound in the same device to provide information of the plaque morphology, without the need for clearance of blood.[62] While these techniques improve image resolution, their expanded use is delayed due to the invasiveness of the procedure. In the scanning fiber endoscope, high resolution images of the artery were obtained along with histology of plaque. [12, 15, 63] The SFE is a forward-viewing device, and thus circumvents the problem of accidentally causing damage to the plaque or its dislocation during side-view imaging along a previously placed guidewire. While the current SFE technique is promising – as seen in the proof-of-concept studies – the rigid tip length is 9 mm long, which may prevent access to smaller and tortuous arteries. However, with advancements in microfabricated scanners and thin meta-optics, the rigid tip length can be reduced, which positions the SFE as a promising future technology to be use adjunctly with CCTA or direct angiography to improve atherosclerotic plaque diagnosis and treatment.

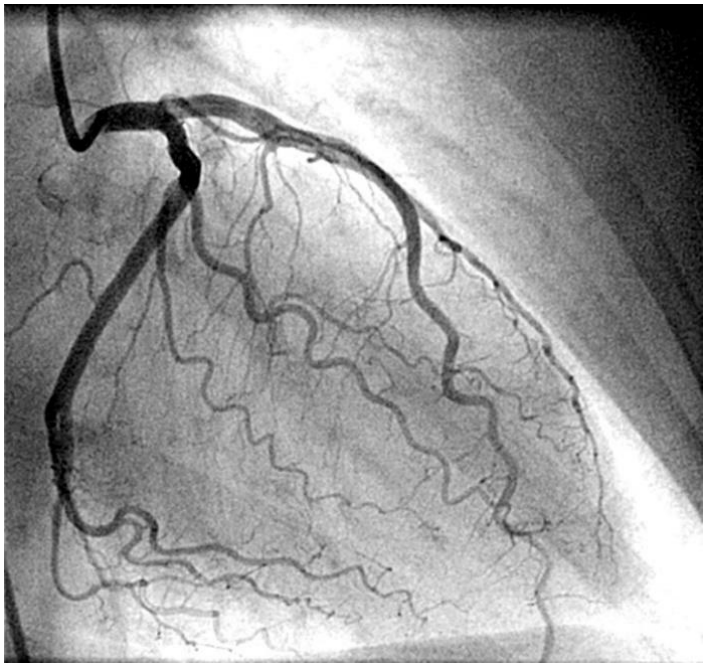

(a)

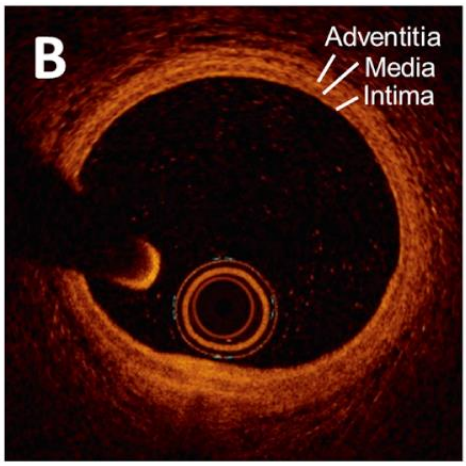

(b) *(c)*

Figure 1.2: Images showing the different diagnostic techniques for plaque. (a) Coronary angiograms are the most common that require catheterization followed by contrast agents and radiation for imaging external to the vessel. (b)[19] An endoluminal imaging technique is using optical coherence tomography which typically scans near infrared laser light from the catheter shaft containing an internal rotating core to the arterial side-walls and a cross-sectional view is acquired, while (c) is full-color intraluminal video frame from the tip of an imaging catheter, such as a scanning fiber endoscope [61] or using an angioscope containing a coherent fiber bundle.

It has been proven that treatment of plaque has improved the quantity and quality of life in patients, while also enhancing the functioning of the heart and reducing symptoms like angina.[20, 21] Treatment of atherosclerotic plaque is done using different methods such as angioplasty, percutaneous coronary intervention, coronary artery bypass surgery, or even atherectomy which involves surgical removal of the plaque.[20] Clearing of blockage using interventional techniques is relatively intrusive in comparison to creating a detour in the blood vessels using a coronary artery bypass surgery. In an angioplasty or a percutaneous coronary intervention (PCI), a catheter is inserted into the body, driven all the way through the blockage, and a stent is deployed at that location. The stent expands inside the artery pushing the plaque outwards, towards the distal region of the lumen, hence opening up the artery for the flow of blood. A significant number of patients with CTO or partial occlusion choose to undergo a PCI, with its high success rates associated and a favorable risk/benefit ratio.[22] PCIs are generally performed on partial occlusions with about 30% of the procedures done on CTOs.[20] In patients where PCI failed to clear the plaque or CTO, laser atherectomy can be used to re-canalize the artery. Laser atherectomy is considered the final method to treat undilatable lesions in coronary arteries.[23] Laser catheters employed in this treatment help soften or loosen the plaque and prepare for subsequent angioplasty if required.[24, 25] Treatment of atherosclerotic plaque has been proven to improve quality and quantity of life with better left ventricular function and reduction in angina [20, 21, 26]. Catheter-based treatments of CTOs is considered as the final frontier in interventional cardiology.[27]

1.4 Angioscopy using imaging catheters

Catheters are a medical device consisting of a thin tube composed of different medical grade materials, to be inserted into body cavities, vessels, or ducts. Catheters serve a wide range of functionalities but are primarily used for administering fluids or gases, assist in drainage of fluids, or provide access to diagnose organs located in hard-to-reach regions. Catheters are usually tailored in design to meet their functional requirements which can vary such as urological, cardiovascular, gastrointestinal, and neurovascular applications. Cardiologists make use of catheters for coronary angiograms and other contrast injection techniques. In addition, interventional cardiologists use them for treating different cardiovascular diseases like aneurysms and CTOs by gently steering guide wires and catheters toward the site of the disease. Typically, cardiac catheterization takes place by entering the body either via the radial artery in the arm or the femoral artery or vein in the leg. As technological advancements continue, catheter design continues to grow more complex and intricate with smaller sizes available that are now able to reach narrow vessels like the coronary arteries located on the heart.

Catheters are manufactured in a large variety of designs. Some have a flexible tube that is driven using a guidewire which helps provide a path that the catheter can follow to reach the desired location. Catheters consist of one or more channels through which substances can be either administered to, or withdrawn from, the region of interest in the procedure. Some catheters are equipped with an inflatable balloon that restricts flow, e.g. of blood, in the lumen that the catheter is in, for the course of the procedure. Catheters may be equipped with fiber optics to transmit therapeutic laser power or visualize the lumen using a coherent fiber bundle, with the objective of either diagnose or treat a condition. Specialized catheter tool tips also exist that have auxiliary instruments and attachments required for the various procedures which are specific to different medical operations.

1.5 Improvements in angioscopes

Over the past few years, technological advancements in the fields of biomaterials, optics, instrumentation, and control, have led to improvements in catheters. An intravascular catheter system was developed in and patented in 2000, in which occlusions are treated using opening members that are actuated using external plungers. It contained multiple optical fibers and a rotating imaging shaft. The optical ends of the catheter are designed to close when flushing takes place using a suitable fluid.[28] Another catheter procedure was developed involving a pulsed laser beam to thermally degrade the atherosclerotic plaque or occlusion within the artery. A balloon is used to occlude the artery and prevent entry of blood from the heart, with saline used as a medium to fill the balloon. The catheter consists of a single optical channel which is primarily used for the laser.[29] Previously, a catheter was developed specifically for angio-surgery. The key feature of this device, invented by a team at the Massachusetts Institute of Technology, was the presence of an optical shield at the distal end of the catheter. The shield is mainly used to 'displace' the blood proximal to the atherosclerotic disease, in addition to protecting the catheter and fiber optics from intravascular substances. This also helps in avoiding any accidental damage to the patient vessel from the catheter tip. The optic shield maintains contact with the plaque tissue while a laser is used to degrade it. The parameters of the laser are optimized using an auxiliary computer.[30] Using similar technology, catheters with spherical lenses were developed. The spherical lens helps focus the laser onto a small, concentrated region to interact with the plaque. With the help of an end cap on the catheter tip, residual energy from the laser is dispersed, which increase the rate at which the plaque is burnt away. The catheter is also equipped with electrodes for ablation of electrical conducting tissue in heart treatment operations. Here, sapphire and silica are utilized in the lens for clearing of the plaque.[31] A different catheter design incorporated the

use of a similar semicircular shield. It also contained a converging nozzle for the irrigation or flushing mechanism to increase the velocity of the flushing jet. This design, however, did not have an optical lens for imaging the plaque during treatment.[31] Another system was developed that used techniques involving different catheters. Initially, a laser is used to create a drilled core within the plaque. The drilled core provides room for a flexible element to attach itself onto the plaque. The plaque is then removed pulling on this flexible element attached to the drilled core, and the artery is cleared with the retraction of catheter.[32]

1.6 Saline flushing of blood

In an endovascular endoscopic or angioscopic procedure, the catheter is inserted into one of the major blood vessels connected to the site of operation and driven to the desired location usually with the help of a guidewire. Once at the proximal location of the cardiovascular disease, operation or treatment can take place. However, in comparison to gastrointestinal endoscopic operations, the lumen of blood vessel is opaque and contains multiple constituents such as erythrocytes or red blood cells, proteins, which do not allow for light to propagate through the blood or interfere with incident light/radiation resulting in inaccurate diagnosis. This complicates optical diagnosis and treatment of the condition. In such cases, a clear fluid is injected to displace the blood and its constituents, providing a uniform optical medium for the acquisition of data either in the form of direct optical images or images produced from near-infrared light (NIR). In the case of OCT, contrast agents work well to displace the blood and provide a good media for imaging the arterial wall.[10] Additionally saline flushing can be utilized for OCT imaging during the PCI, instead of using an iodine-based radiopaque contrast agent.[14] The contrast agent, used for flushing blood for X-ray image acquisition, can lead to acute renal failure in high risk patients. [33, 34] Pre-clinical studies showed saline flushing imaged slightly reduced area in comparison to contrast

agents.[35] Recent clinical studies show that saline can be used as a safe alternative to contrast agents for OCT image acquisition while other studies prove the saline is a superior agent for flushing blood and cheaper than contrast agents.[10, 36, 37] “Saline flushing” involves injection of saline is injected via one of the lumens present in the catheter to clear or push the blood away. Saline flushing fills the catheter lumen with saline, which can be used to push contrast medium and other medication to the site of the catheter. Saline is known to help in scanning of sections of the body by reducing the artifacts that arise during visual analysis.[17, 38-40] With a higher emphasis on direct visualization of the plaque causing CTOs through optical techniques, via OCT or side-viewing angioscopes, saline flushing is a promising methodology to flush out blood from the imaging path and provide a transparent medium through which to image or treat the CTO.[16, 18, 23, 41] For high resolution full-color forward-viewing angioscopy, saline or with the additive of low-density dextran flushing is the exclusive technique to clear the blood. This enables full-color or RGB imaging of the artery and plaque provides more detailed information of the plaque and its composition as clinicians have a clear view of the plaque inside the artery, leading to improved treatment outcomes [12, 13, 15, 16, 42]

In laser atherectomy, saline flushing not only allows for propagation of the laser from the catheter tip to the plaque, but also helps reduce the temperature from the heat generated by the laser, keeping temperatures within the artery close to physiological levels.[43] Incomplete clearance of blood restricts imaging and diagnosis of plaque, which mainly arises due to varying parametric and geometric conditions of the blood vessels.[24, 28] Previous studies have provided suggestions on how to improve saline flushing to obtain better quality images in endoscopic procedures, but damage to vessel walls has been observed in occlusion-infusion catheters.[24] These

complications that arise during the treatment of atherosclerotic plaque beckons the need for understanding of saline flushing mechanics within arteries.

1.7 Motivation for current research

Anatomical and operational variability in the procedures can result in incomplete clearance of blood and limited imaging and diagnosis of the CTO.[24, 43] Some studies have suggested using larger volumes of saline for higher quality of the imaging during the angioscopy.[24] Additionally, these large volumes are facilitated with large flow rates which require bigger lumens in catheters. [10, 12] As medical technology evolves and catheter sizes reduce, such larger lumens no longer remain viable to assist in saline flushing. The use of occlusion-infusion catheters for angioscopy has been known to cause damage to the arterial wall either from the high pressure infusion process or from the inflation of the occlusion balloon.[24, 44, 45] Parametric CFD studies have been previously conducted to improve the saline flushing process and other flushing agents.[46] For imaging plaque and arterial walls, higher saline injection rates are favorable along with the position of the catheter, however the speed of injection is critical in preventing damaged arteries. [40, 47]

Additionally, a team at the Human Photonics Lab at the University of Washington, has been working on developing imaging techniques used in endovascular catheters.[11-13] The innovative technology developed at this research lab is creating new avenues in terms of optical imaging and sensing of disease inside different lumens in the human body. Recently, a scanning fiber endoscope sized 1 mm housing a full-color imaging wide-field lens was designed by the team. Their innovation produced remarkable results and can be integrated into different diagnostic modalities.[15] However, the improvements in this direction account primarily for technical

advancements in the imaging. By introducing improvements in the dynamics of blood and fluid interactions influencing the flow of blood revolving around the area of interest, further technological advancements in these catheters can take place in parallel.

A new physics-driven approach to designing catheters provides a platform to understand the fluid mechanics involved. By exploring the saline-blood interaction, catheter design can be optimized to maximize the space requirements on the catheter cross section. Pressure analysis within the entire flushing system is crucial and is has not been investigated in detail previously. In an already weakened artery, the development of overpressure due to injection of a new fluid is a risk in the diagnostic or surgical operation. Rupture of the artery can take place during treatment, exacerbating the risk factor and increasing the complications associated with the technique.

With growing need to develop smaller angioscopies facilitated by groundbreaking progress in optical technology, the bottleneck exists in the fluidic system.[15, 48] There is an urgent need to understand and improve saline flushing systems to improve diagnosis and treatment of atherosclerotic plaque. Additionally, enhancing visibility of plaque improves the probability of success as limited visibility and incomplete clearance has prevents proper examination of the plaque. As such, a better understanding of the dynamics of saline flushing within arteries affected by a plaque would improve diagnosis, enable treatment, and reduce risk.

1.8 Outline of the study

In this work, the fluid mechanics of saline flushing during angioscopy are analyzed, primarily with consideration to the diagnosis of CTOs, partially occluded vessels and finally CTOs near bifurcations in simulated human coronary arteries. Chapter 2 includes a comprehensive summary of the in vitro experimental setup for complete and partially occluded vessels, optical experiments,

and numerical model employed to provide actual and predictive understanding of imaging of occlusions. The numerical simulations are complemented with optical ray tracing analysis that provides a better perspective into the performance metrics of the study. In Chapter 3, the result from chronic total occlusions is first presented, which forms the basis of our novel catheter system. Chapter 3 also contains a detailed discussion on the application of the catheter to idealized anatomical and physiological conditions representative of the complete occlusion. The efficacy of this system on partially occluded vessels and occlusions near bifurcations is explored in Chapter 4, along with a review of the results and the significance of the results are highlighted with direct correlation to clinical applications. Finally, the cardiovascular system study is summarized and concluded, along with the limitations of this work and suggestions on prospective future studies.

Chapter 2

METHODOLOGY

The aim of this study is to understand hemodynamics of saline flushing inside coronary arteries and driving the development of fluid injection catheter system to enable a forward viewing high resolution scanning fiber endoscope to visualize the artery and the plaque.[16] The study employs a mixture of experimental and numerical techniques to determine the performance of different fluid systems and predict their efficacy in clinical settings.

2.1 In vitro planar laser induced fluorescence (PLIF) experiments – for total occlusions

An in vitro phantom of an idealized coronary artery lumen was casted in silicone. The phantom, with dimensions 2.7 mm ID was immersed in a glycerol, salt, and water mixture that matched its

refractive index of the silicone cast. A plug simulating the CTO was placed blocking one end of the lumen. The artery phantom was filled with a solution of water, glycerol, and salt mixture (47.5 %, 35.8%, and 16.7% respectively to match the viscosity of blood) containing five parts per million (PPM) rhodamine B. The two-lumen suction-injection catheter was placed at the entrance to the artery phantom lumen. The saline lumens (ID = 0.35 mm) were connected to synchronized syringe pumps that regulated the injection and suction flow rates. A planar laser induced fluorescence setup was used to image the injection of saline and the flushing of the blood-mimicking fluid. A Coherent Genesis STM CX Laser (532 nm) was focused into a thin beam and then fanned out into a plane, 1.1 mm in thickness, using a series of spherical and cylindrical lenses. Fluorescent light emitted by the rhodamine dye was captured by a high-speed camera (Phantom v711, Vision Research, Trenton, NJ) after passing through a long-pass filter that removed reflections of incident light. The image sequences (recorded at 250 frames per second) were analyzed using MATLAB (MathWorks Inc., Natick, MA).

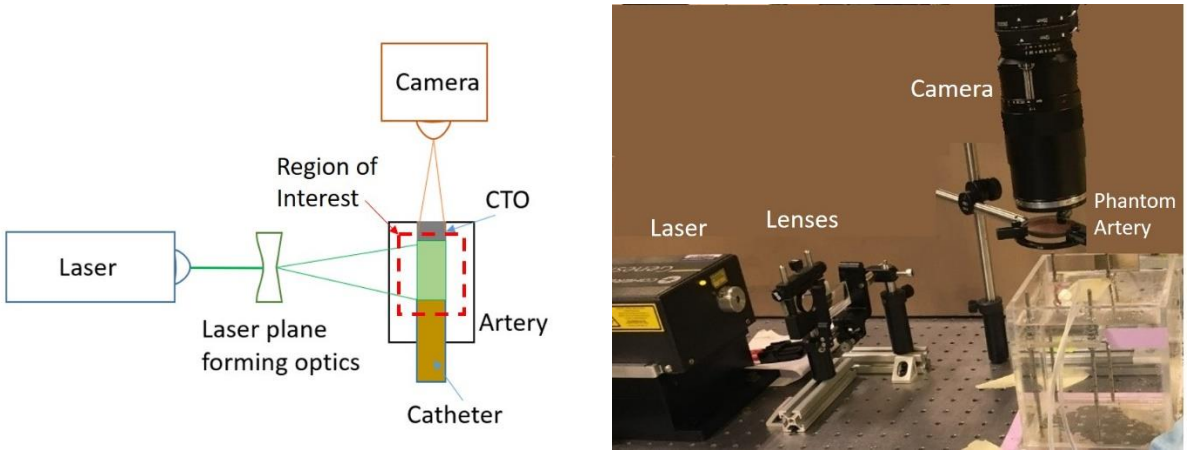

(a) *(b)*

Figure 2.1: The experimental setup consists of a 532 nm continuous laser illuminating a thin plane of an artery phantom containing a blood-mimicking fluid dyed with rhodamine. The resulting

fluorescence is captured by a high-speed camera (orthogonal to the laser plane) as shown in the (a) schematic, and (b) actual experimental setup.

2.2 In vitro planar laser induced fluorescence (PLIF) experiments – for partially occluded vessels

A 97% idealized partially occluded artery print was cast in silicone to produce an in vitro artery phantom. The 3.5 mm sized artery phantom was connected to a flow loop with a solution of water, glycerol, and salt at 47.5%, 38.5% and 16.7% ratio respectively, to match the density and viscosity of blood. The solution is pumped via a Harvard Apparatus Pulsatile Blood Pump at a flow rate that matches a patient derived flow profile published in literature previously. Two hypodermic needles of ID 0.3 mm are inserted from each side into the artery phantom to replicate the catheter lumens. The needles are connected to a two-channel syringe pump which injects saline into the artery to clear the blood mimicking fluid. The saline contains rhodamine B at concentration of one hundred parts per million (PPM). The injection of saline and flushing of blood mimicking solution is imaged via a planar laser induced fluorescence setup. A Coherent Genesis STM CX Laser (532 nm) was focused into a thin beam and then fanned out into a plane, 1.1 mm in thickness, using a series of spherical and cylindrical lenses. Rhodamine B is excited by the laser and emits fluorescence which is captured by a high-speed camera (Phantom v711, Vision Research, Trenton, NJ) after passing through a long-pass filter. The image sequences (recorded at one hundred frames per second) were analyzed using MATLAB (MathWorks Inc., Natick, MA).

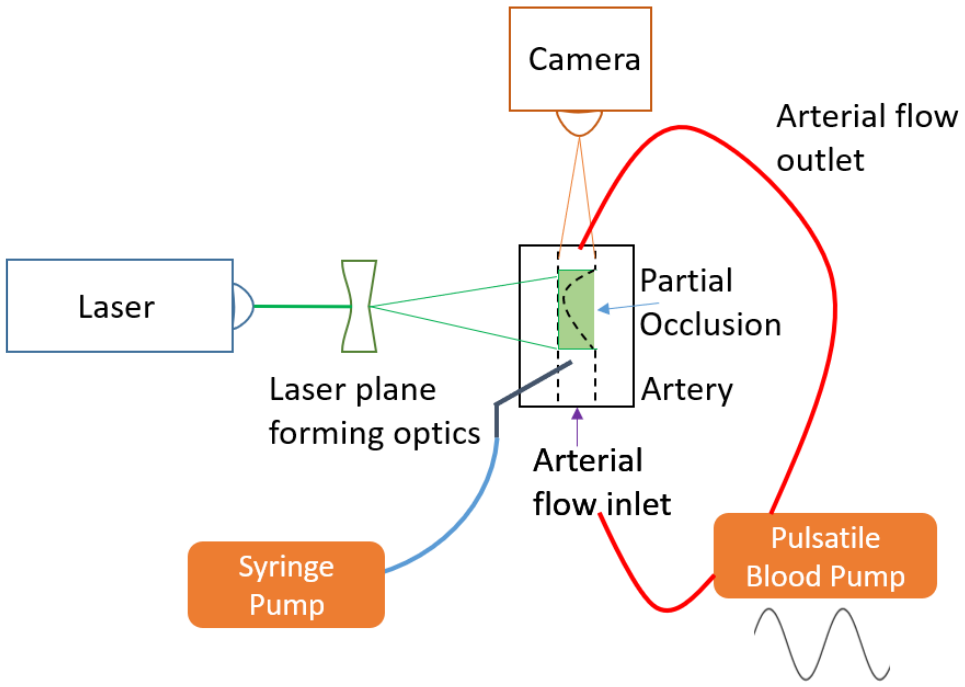

Figure 2.2: The experimental setup consists of a 532 nm continuous laser illuminating a thin laser plane inside a partially occluded artery phantom. Blood is pumped via a Harvard apparatus pulsatile pump through the artery. Saline dyed with rhodamine B at a concentration of 100 ppm is injected into the artery upstream of the partial occlusion to flush the blood away. As saline interacts with the laser plane rhodamine emits fluorescence which is captured by a high-speed camera orthogonal to the laser plane as shown in the schematic.

2.3 In vitro optical experiments

The PLIF experiments show clearance of blood from a fluid's perspective since the blood mimicking fluid matches the viscosity and density of blood. In vitro optical experiments explain the actual visualization of the artery and plaque. An idealized straightened artery phantom was cast in silicone. The downstream end was plugged with a checkered target. The proximal upstream end was plugged with a 1.6 mm scanning fiber endoscope with two hypodermic needles of 0.3 mm diameter representing the injection and suction lumens. Blood mimicking phantom consisting of a solution of water, India ink and intralipid 20% solution was injected into the artery phantom before

sealing the region with the catheter plug. The hypodermic needles are connected to a syringe pump via thin tubing. As saline is injected via the syringe pump into the artery, along with suction of the saline and blood mimicking fluid mixture, the display from the scanning fiber endoscope is recorded.

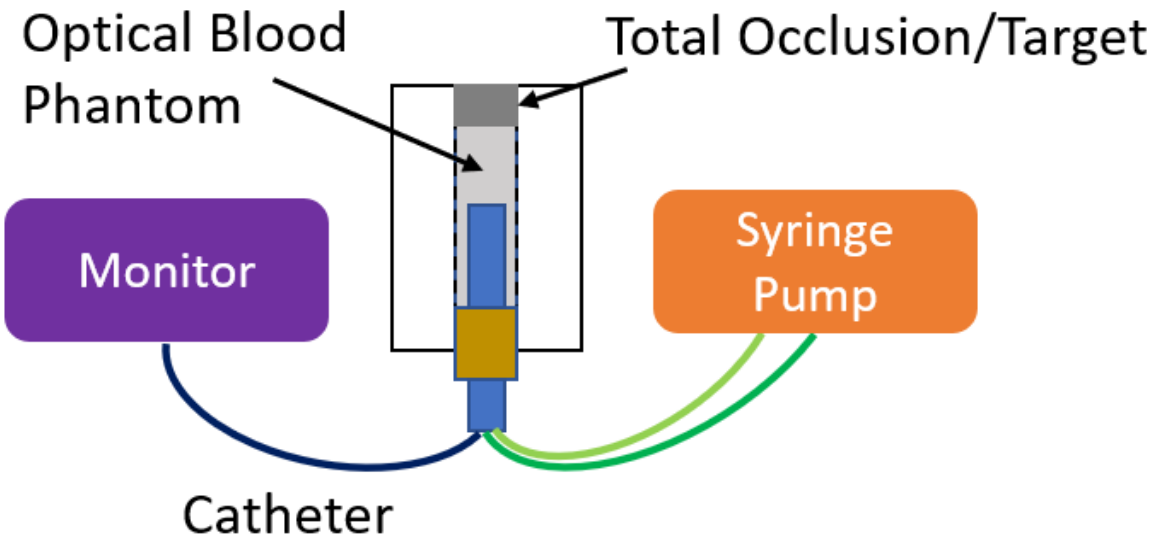

Figure 2.3: Blood mimicking fluid that matches the absorption and scatter of light is filled into an silicone arterial phantom with one end plugged by a checkered target representing the CTO and the other end plugged by the scanning fiber endoscope along with hypodermic needles representing the suction-injection lumens.

2.4 Numerical modelling and analysis

Catheter and artery geometries

For the CTO simulations, the required geometries for the catheter models were created using the in-built CAD modeler in Star-CCM+ (CD-Adapco/Siemens, Melville, NY). ` Three different catheter designs were examined. A co-axial annulus injection catheter, diametrically opposed suction-injection lumens, and adjacent suction-injection lumens (the synchronized suction-

injection method used this last geometry). The design process took an evolutionary approach, to improve the flushing mechanics and simultaneously maintain sufficient space, between 1.0 mm^2 to 2.0 mm^2, to house additionally elements. The three designs had additional cross-sectional area of (a) 0.95 mm^2 and (b), (c) 1.9 mm^2, with the latter having more contiguous space as seen in Figure 2.

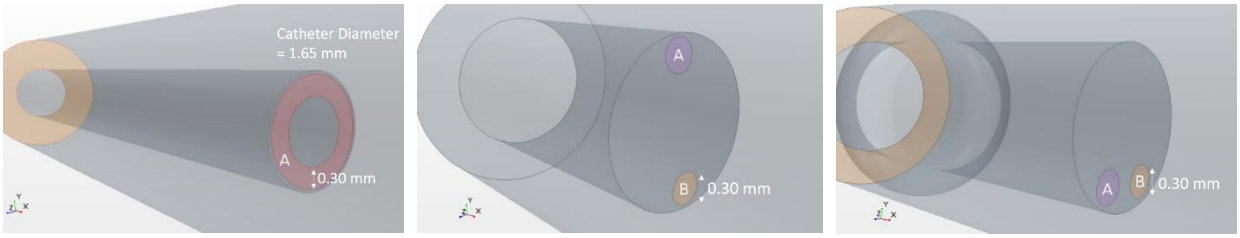

(a) *(b)* *(c)*

Figure 2.4: Different configurations of saline injection (A) and suction (B) lumens on the catheter tip (5 Fr or 1.65 mm diameter). The design process involved starting with a simple catheter with saline injection only (left). A suction lumen was introduced diametrically opposite to a smaller injection lumen (middle). And finally, the two lumens were placed adjacent to one another in the last configuration (right) which is part of the synchronized suction-injection system.

For the partial occlusions and occlusions near bifurcation models, the arterial and catheter geometries were designed and developed in Solidworks (Dassault Systemes, Velizy-Villacoublay, France) and the simulations were modelled in StarCCM+ (CD-Adapco/Siemens, Melville, NY). Three different arterial morphologies were investigated - 97%, 95%, and 90% occluded vessels. In each morphology, a 6 Fr (2 mm) catheter is placed with two lumens, each with a diameter of 0.5 mm. For modelling occlusions near bifurcations, an idealized model of the left main coronary artery which bifurcates into the left anterior descending artery and the left circumflex artery was chosen. The artery diameter changes from 5 mm in the left main into 3.5 mm in the left anterior

descending and 3.0 mm in the left circumflex artery, with the occlusion commonly found in the left anterior descending artery.

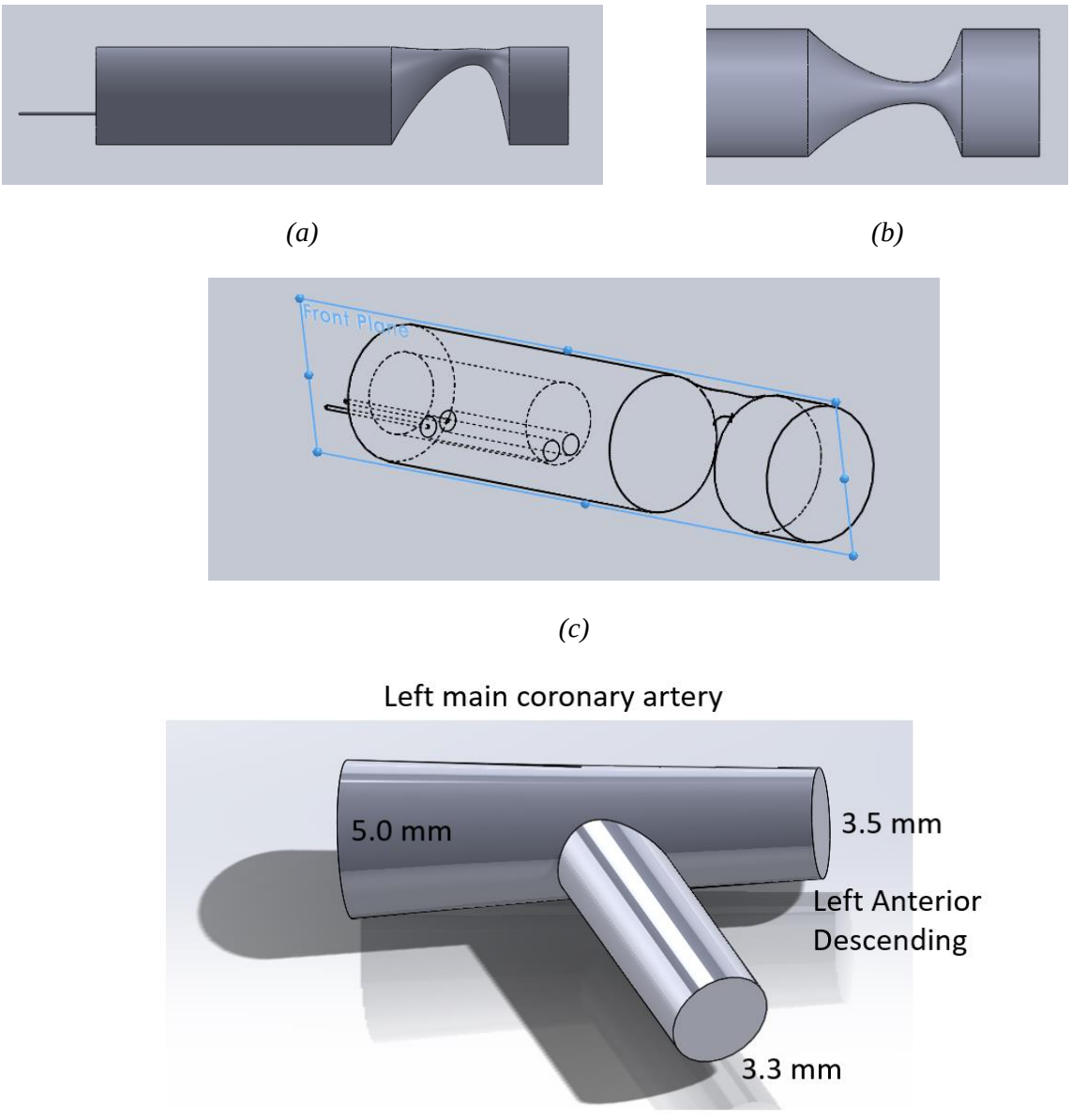

Figure 2.5: The partially occluded and bifurcated arterial CAD geometries were developed in Solidworks. The occlusion size was varied to block 97%, 95% and 90% of the original arterial cross-section. The idealized occlusion reduces the are in 3D as can be seen in the (a) side view and the (b) top view. The saline injection lumens are directed towards the occlusion and away from the arterial

opening (c). For modelling occlusions near bifurcations (d), an idealized model of the left main artery was used, with the total occlusion present in the left anterior descending branch.

Grid convergence and time step

The number of mesh cells used to discretize the fluid domain was between 0.8 to 1.4 million. The characteristic cell size was 75 microns. The depth of the prismatic layer along the walls was limited to 4, while the grid filling the core of the artery lumen was composed of tetrahedral cells. The mesh density was satisfactorily evaluated for grid independence. The grid independence study was performed for a small volume (steep taper case) using three different mesh sizes with 500k, 720k, & 2.2 million cells, with base cell sizes of 0.1 mm, 0.075 mm, & 0.05 mm, respectively. Average velocity and mass fraction of saline were compared in a small spherical domain of 0.05 mm radius. The results from the convergence study are available in the supplementary materials. The time step was set at $1x10^{-5}$ s, consistent with the spatial discretization to satisfy a strict CFL condition. Inner iterations were conducted till the residual converged to an error of $1x10^{-6}$, before proceeding to the next time step. Simulations were performed on a distributed-memory cluster at University of Washington.

Boundary conditions

The artery, plaque and catheter walls were modelled with rigid no slip walls. Inlet and outlet boundary conditions included constant flowrate and constant pressure at the saline inlet based on the type of injection control studied. Coronary artery, time-dependent pressure between 12.2 kPa and 12.8 kPa, was used as the boundary condition for the proximal artery in all cases, except the

annulus injection catheter where a normalized pressure outlet was prescribed. This is a patient derived, left anterior descending, time dependent pressure used in a previous study This pressure condition was used in all cases except when simulating the annulus injection catheter which lacked any outflow channel. Constant pressure (always lower than the hemodynamic pressure in the artery) or constant flowrate were set at the suction catheter end. In the partially occluded vessels and bifurcating vessel, a normalized pressure outlet was prescribed at the downstream arterial exit.

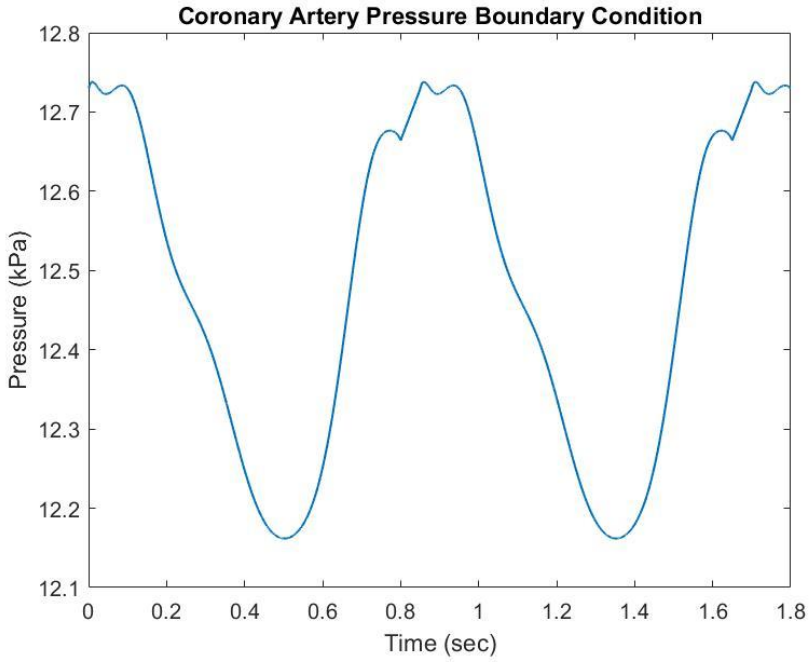

Figure 2.6: Pulsatile coronary arterial pressure wave form used for the pressure boundary condition at the proximal end of the artery.

Simulation physics

The simulations are setup as a multi-component liquid, where the two components are blood and saline. Each individual component is simulated with constant density. The conservation of mass

and momentum equations are solved to obtain the velocity and pressure values throughout the domain:

$$\nabla . u = 0$$

$$\frac{\partial u}{\partial x} + u \,.\nabla u = \, -\nabla P + \mu \nabla^2 u$$

Using StarCCM++ 12.02.010 (CD-Adapco/Siemens, Melville, New York, USA), the incompressible Navier stokes equations are solved in three dimensions. The flow properties within the simulation are such that the flow remains laminar through the entire simulation. To advance the time step, a first order implicit time-stepping scheme is applied, which provides the required unsteady conditions for the simulations. The time step for each simulation is $1x10^{-5}$ seconds and the simulations run for about one second, or till clearance is achieved. Clearance in the simulations is considered when there exists 98% saline concentration by mass fraction between the tip of the catheter and the CTO. Saline is modeled as a liquid with physical properties like water, while blood is assumed to have a density of 1050 kg/m3 with a viscosity of 3.5 cP. The fluids are selected to be non-reactive in terms of their chemical properties.

Multi-component fluid mechanics

A multi-component mixture is a miscible mixture of two or more pure substances in the same phase. Each individual fluid is initially defined in terms of its density, viscosity, and molecular weight. Subsequently, the mixture properties are to be specified to predict how the two fluids will interact with each other. The mixture properties are defined as the combined density, dynamic viscosity, molecular diffusivity, and molecular weight.

Combined density

The density of the mixture is calculated based on the volume-weighted mixture function. The function can be described as:

$$\theta_{mix} = \frac{1}{\sum_i^N (\frac{y_i}{\theta_i})}$$

where θ_{mix} is the density of the mixture, N=2 for our case, y and θ are the volume fraction and density of the specific component at that location, respectively.

Combined dynamic viscosity

The dynamic viscosity of the mixture is calculated based on the mass-weighted mixture function. The function can be described as:

$$\emptyset_{mix} = \sum_{i=1}^{N} y_i \emptyset_i$$

where $\emptyset_{mix}$ is the dynamic viscosity of the mixture, N=2 for our case, y and $\emptyset$ are the mass fraction and dynamic viscosity of the specific component at that location, respectively.

Molecular Diffusivity

The molecular diffusivity of the two fluids is defined in terms of the Schmidt number. The Schmidt number is a non-dimensional defined as the ration of momentum diffusivity and mass diffusivity. It characterizes fluid flows that have both mass and momentum diffusion convection processes. Ideally it denotes which of the two processes, i.e., the molecular or momentum diffusion, is predominant The Schmidt number is defined as:

$$Sc = \frac{\nu}{D} = \frac{\mu}{\rho D}$$

$$Sc = \frac{viscous\ diffusion\ rate}{molecular\ (mass)\ diffusion\ rate}$$

where *Sc* is the Schmidt Number, ν is the kinematic viscosity, *D* is the mass diffusivity, μ is the dynamic viscosity of the fluid, and ρ is the density of the fluid.

For the simulations presented here, the Schmidt Number was set to 1. A Schmidt number of unity signifies that the molecular diffusion process is comparable to the momentum diffusion process. However, in the physics concerning the problem of catheter imaging and optical clarity of the fluid between the catheter tip and CTO, the molecular diffusion process is negligible. By establishing the Schmidt number to unity, our simulations grossly overestimate the molecular diffusion process, which will have a minor influence in the actual physics studied. This helps to make the simulation time manageable even if it ignores the mixing of saline and blood at the cellular or molecular levels, which will not affect the optical transparency.

The initial conditions prescribed within the simulation are realistic arterial conditions. The fluid within the entire domain is blood. The average blood pressure is set to 70 mmHg.

2.5 Simulation parameters of interest

Mass fraction of saline

Mass fraction of saline is the ratio of the amount of saline that exists at a particular location by mass over the total mass of the combined fluid (Blood and saline). It gives us an understanding of the transparency of the blood-saline mixture in front of the plaque, which is required to image the plaque and artery. The required mass fraction to obtain clearance using saline flushing is 98% between the catheter and the plaque.

$$Mf_i = \frac{m_i}{m_{total}}$$

where Mf_i is the mass fraction of species *i*, m_i is the total mass of species *i*, and m_{total} is the total mass of all the species in the mixture.

Clearance time

The time required to completely flush the blood using saline is a key parameter that is used to understand the saline flushing mechanism. The flow rate of saline into the artery is regulated to obtain the clearance within optimum time levels. It is primarily defined as the time when the blood-saline mixture reaches an average mass fraction of 98% in the volume between the catheter tip and the plaque.

Reynolds number

Reynolds number is a non-dimensional number that helps characterize the fluid flow. It broadly serves to describe flow as either laminar or turbulent. Laminar flow has smooth streamlines and is represented by low values of Reynolds number while higher values of Reynolds number describe a complex and non-parallel turbulent flow. The Reynolds Number is designated as

$$Re = \frac{\rho V d}{\mu}$$

where Re is the Reynolds Number, ρ is the density of the fluid, V is the velocity of the fluid, *d* is the characteristic length, μ is the viscosity of the fluid, and ν is the dynamic viscosity of the fluid.

2.6 Optical ray tracing

Once the saline solution begins to push the blood away from the CTO, the transparency of the saline-blood mixture in front of the CTO increases. As light transmittance increases, the CTO can

be imaged by the clinician for treatment. To understand the light propagation involved in the procedure, an optical ray tracing study was conducted.

Cone of view

The optical analysis assumed that the center of the catheter houses two optical fibers adjacent to one another. The optical fibers transmit light from a light source to the arterial cavity and return reflected light from the cavity to a sensor/monitor in the treatment room. This way, the region under visual inspection is a cone of view with the center of the catheter acting as a vertex and the base of the cone represented by the CTO. The fluid residing within this cone of view influences the visibility of the CTO while the adjacent mixture has negligible effect on the technique.

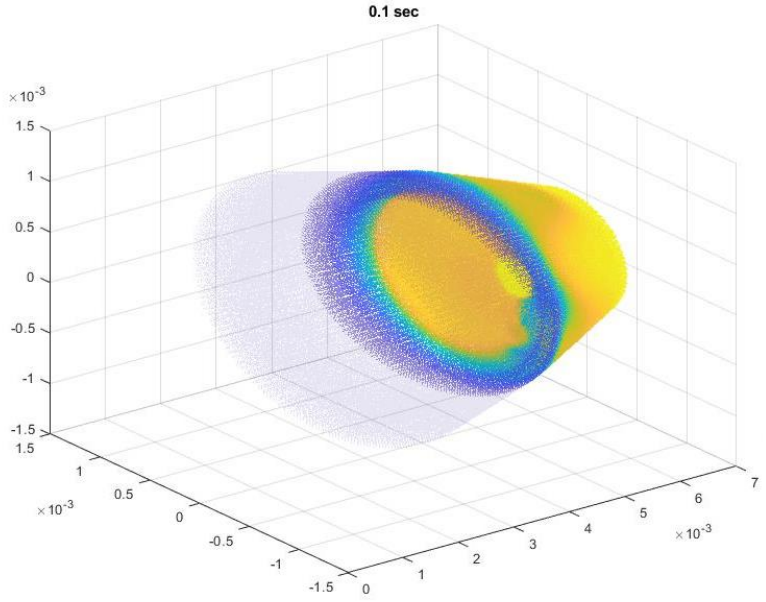

(a)

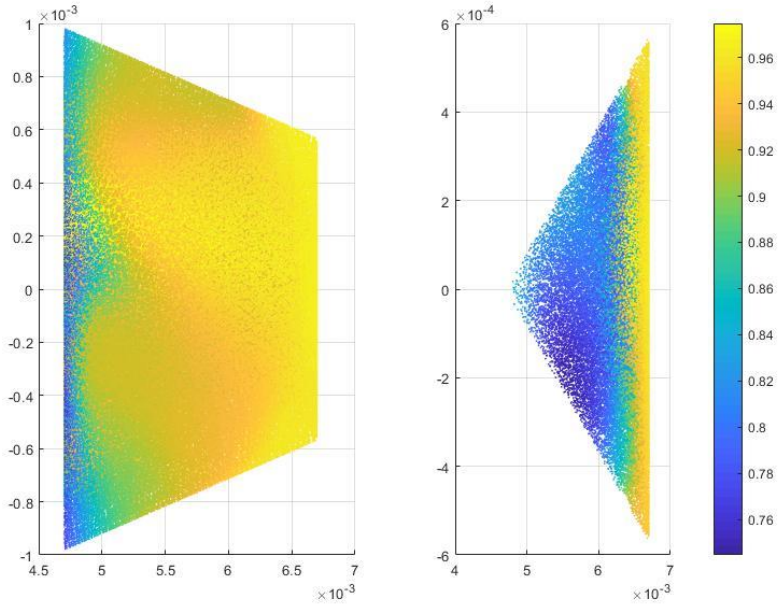

(b)

Figure 2.7 Developing the cone of view. The saline mass fraction data is extracted into MATLAB (a). The region behind the face of the catheter is removed (b) (left) and then trimmed to the cone of view with the center of the cone at the catheter and the edge defined by the edges of the CTO (b) (right). The color bar represents the intensity of light.

The mass fraction of saline from each simulation was sampled and extracted at every 0.01 seconds. The sampled data was introduced into MATLAB (MathWorks Inc., Natick, Massachusetts, United States) where the data is trimmed to represent the cone of view. The height of the cone is equal to the standoff distance between the catheter and the CTO. This standoff distance varied based on the plaque morphology of the simulation and was equal to 0.128 mm, 0.2 mm, 0.37 mm for zero clearance, steep wedge, and shallow wedges, respectively.

Optical map

An optical map was generated based on interpolation of data derived from a study conducted earlier. The wavelength of light selected for the optical analysis was 505 nm. The optical map

generated provided the optical density of the blood mixture depending on the optical distance of through which the light would travel as well as the hematocrit concentration of the blood. About 408 light rays were projected from the center of the catheter to the CTO and the endpoints of these rays were uniformly distributed on the CTO surface. Each ray was broken down to about 0.0379 mm which represented an individual segment. The mass fraction of saline was used to determine the hematocrit of the blood present in each individual segment using the formula

$$HC = \frac{(1 - Mf_s) * 45 * 0.6206}{3}$$

where HC is the hematocrit of the segment, Mf_s is the mass fraction of saline, the original hematocrit of pure blood in the patient is set to be 45%, the divisional factor of 3 is used to convert the hemoglobin number to hematocrit. The factor 0.6206 is used to incorporate the unit conversion from g/dL to mmol/L when dealing with the hematocrit number.

The optical density was then calculated individually based on the hematocrit and the segment distance from the optical map developed earlier. The optical transmittance of each segment was then summed over the entire travel length and doubled to incorporate the reflectance of light from the CTO. This optical transmittance was using the equation

$$Tm = \frac{10^{(2-OD)}}{100}$$

where Tm is the Transmittance of light, and OD is the optical density or absorbance of light by the saline blood mixture.

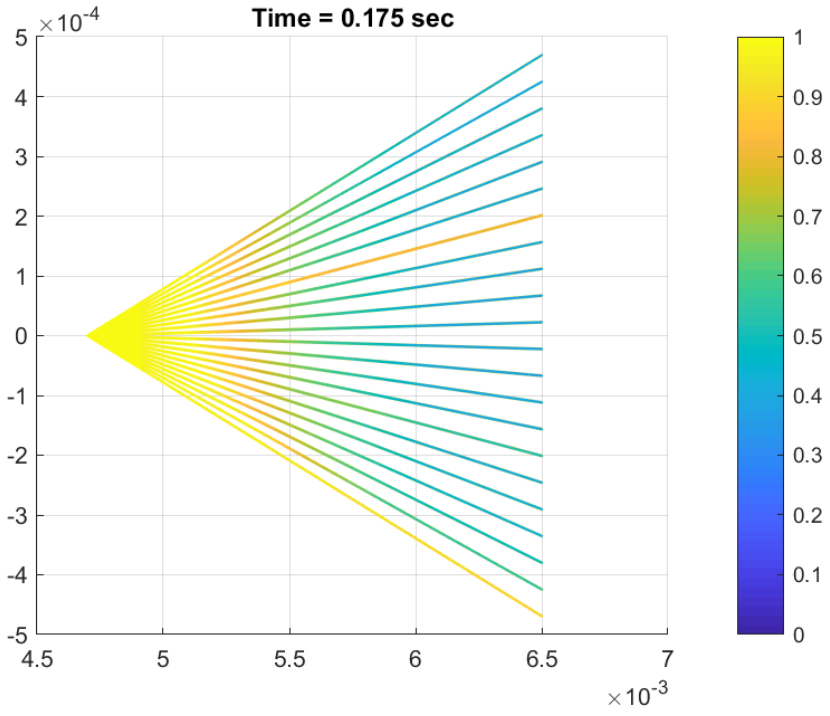
Time = 0.175 sec
×10^-4
5
4
3
2
1
0
-1
-2
-3
-4
-5
4.5
5
5.5
6
6.5
7
×10^-3
1
0.9
0.8
0.7
0.6
0.5
0.4
0.3
0.2
0.1
0

(a)

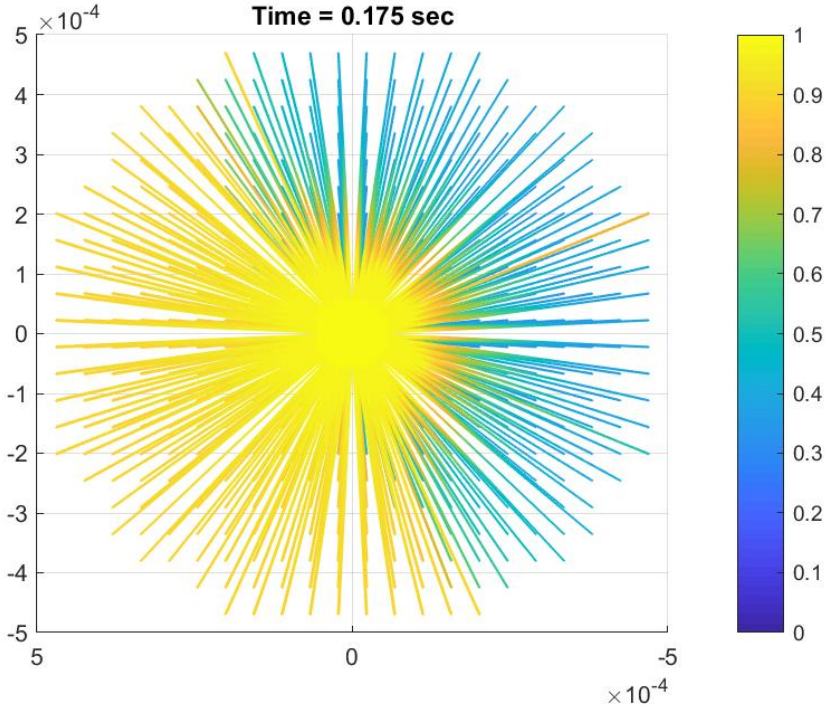
Time = 0.175 sec
×10^-4
5
4
3
2
1
0
-1
-2
-3
-4
-5
5
0
-5
×10^-4
1
0.9
0.8
0.7
0.6
0.5
0.4
0.3
0.2
0.1
0

(b)

Figure 2.8 Ray tracing from the center to the CTO using the optical transmittance. The side view (a) and the front view (b) of the ray tracing is shown. The color bar denotes the intensity of light that returns to the sensor after being reflected of the blood or the CTO.

Target analysis

A checkered blue and white target was created that represented the visualization of the CTO. As the opacity of the mixture increased, the target is better visualized and the adjacent colors of blue and white are distinguishable from one another. A transparency level of 80% was selected as the threshold above which the CTO could be visualized. By comparing different images of the target, comparisons were made on the feasibility of the flushing technique and the characteristics of the catheter visualization technique were defined. When adjacent squares are clearly distinguishable as blue and white, the flushing or clearance is achieved.

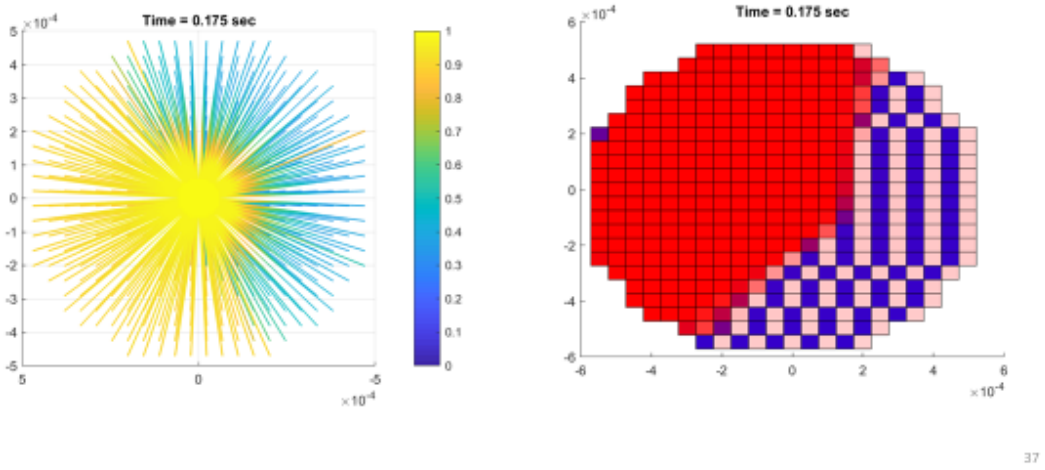

(a)

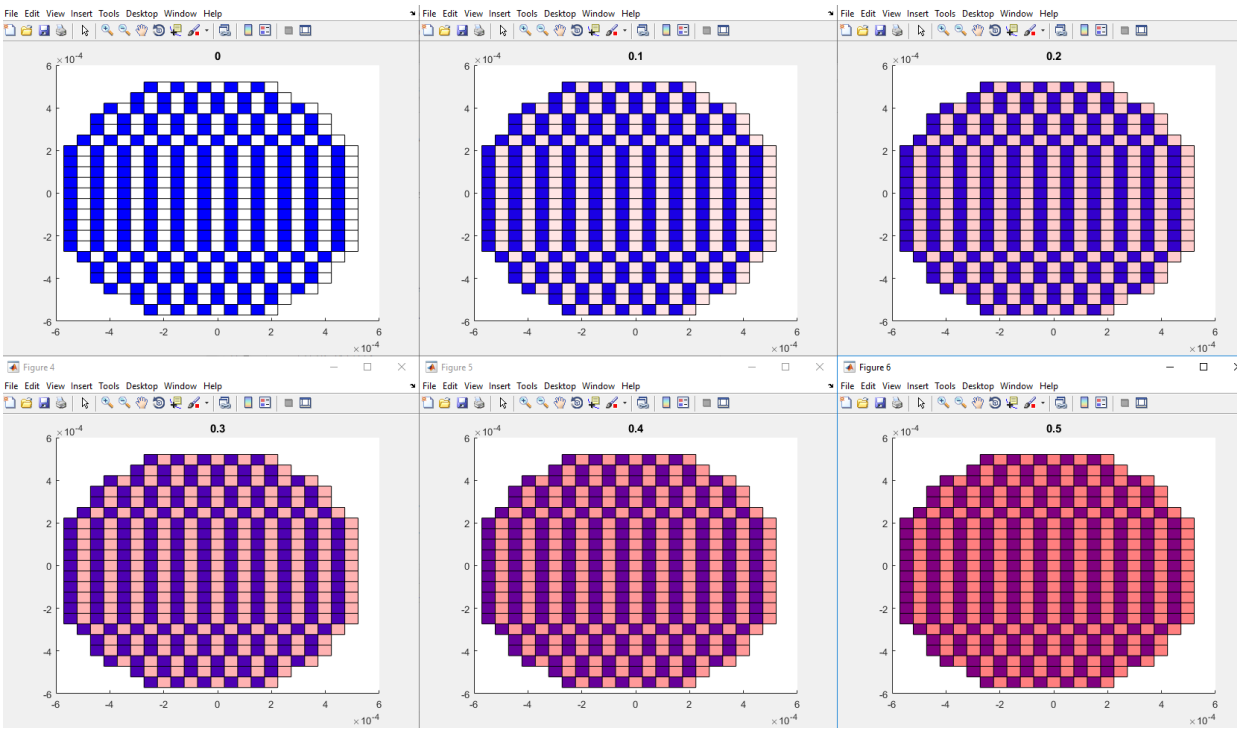

(b)

Figure 2.9 Target visualization to determine clearance of blood. The rays from the optical analysis are mapped onto the target to understand the region where blood interferes with the diagnosis (a) The red region represents the undiluted blood which prevents the viewing of the CTO. The right image is a mirror image of the ray tracing on the left. In (b) the various levels of clearance are displaced. The clearance threshold was selected to be 0.2 or (80% intensity of light) determined by comparing various levels of clearance where the red hue due to the blood is minimal.

Chapter 3

CATHETER CONCEPT, DESIGN, & INNOVATION

Synchronized suction-injection catheter system

The work presented in the thesis is a novel approach to developing flushing catheters dictated by the fluid mechanics to improve visibility of the CTO to the interventionists. The design of the catheter took an evolutionary process as improvements were continuously added to enhance the flushing technique. Some of the designs showed promise hydro-dynamically but were later rejected for being associated with practical limitations.

3.1 Simulation based catheter design

Central Injection Catheter

The first catheter employed in the simulations consisted of a straightforward design. The model included a long straight artery, with a catheter housing a circular lumen coaxial with the catheter. Saline flushing is fast, however, the intra-arterial pressure was high along with extremely high injection pressures (~1.2 MPa). To reduce these high injection pressure, the injection lumen area is increased.

Annulus injection design

The initial annular lumen proposed had a large hydraulic diameter, resulting in low injection speeds and Reynolds numbers. Thus, there was room for a significant reduction in the injection lumen diameter, as seen in Figure 2. From a fabrication and manufacturing standpoint, the annulus design provided challenges and practical limitations.

Suction Lumen injection

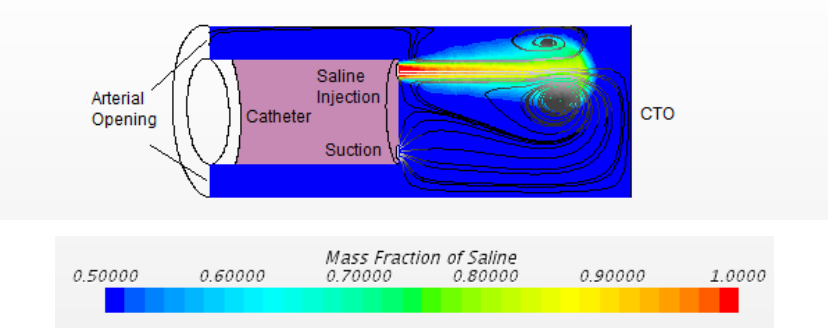

Figure 3.1. The introduction of a suction lumen drastically reduces the time required for optical clearance. The two lumens are placed diametrically opposite to each other as shown in Figure 3.2 (c). Image captured right after injection at 0.006 sec.

A suction lumen was introduced in the catheter prototype and placed diametrically opposite to the saline injection lumen as shown in Figures 3.2(c). The injected saline displaces the blood in coordination with the suction into the upper lumen. As illustrated in Table 2, the introduction of the suction lumen reduces the time required for saline flushing of the blood in the gap between the

tip of the catheter and the CTO, even with lower injection flow rates. In the novel flow configuration, blood (or blood/saline mixture) is displaced from the CTO by being sucked into the catheter frontal face, not only by the injection pushing the blood out of the gap. Instead of having to flow away from the CTO moving around the imaging element in the narrow gap between the catheter side wall and the arterial walls, blood/saline mixture is suctioned out of the artery. Finally, the two lumens were placed adjacent to each other increasing space available for optical elements on the catheter, resulting in a robust catheter design.

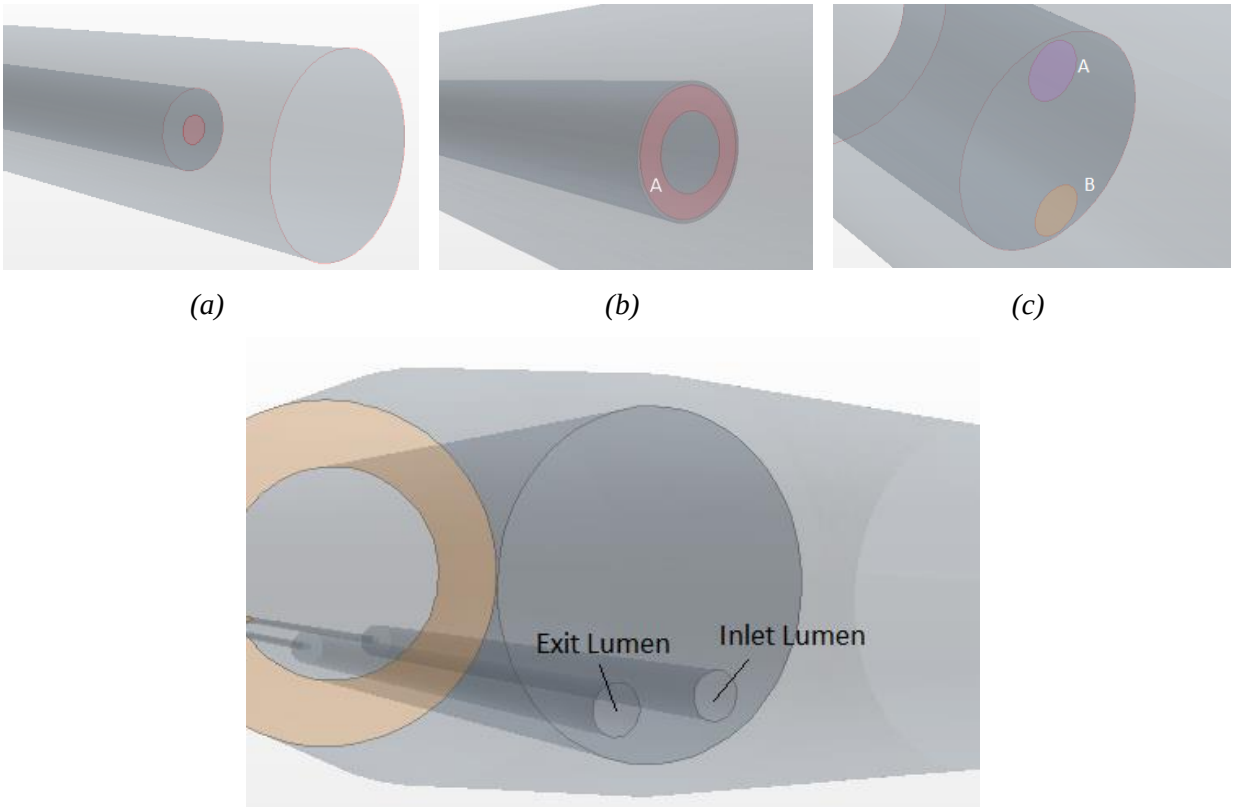

(a) *(b)* *(c)*

(d)

Figure 3.2: The CFD inspired evolutionary design process started with (a) central injection catheter. Due to high injection pressures, the injection area was increased in the (b) annulus injection design. To improve the robustness and the flushing physics a suction lumen was introduced (c). Finally, the suction and injection lumens were placed next to each other(d) to provide more space for optical elements.

3.2 Synchronized suction-injection catheter: saline flush control

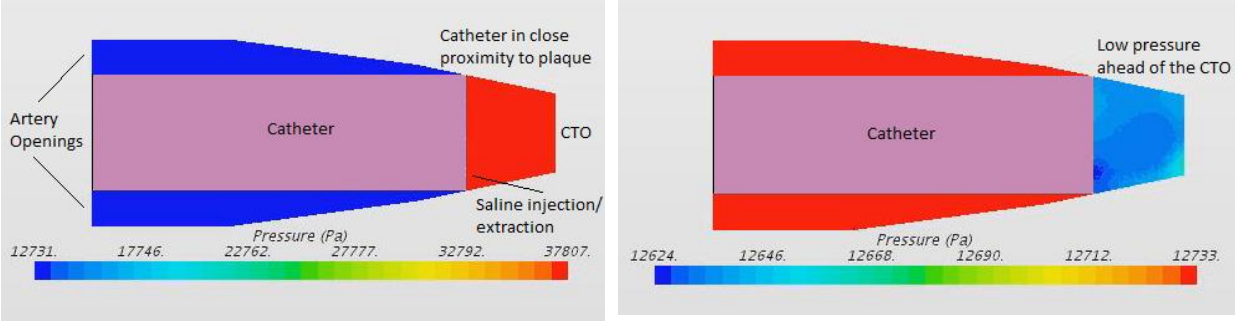

(a) *(b)*

Figure 3.3. Cross-sectional view of the domain displaying the pressure values between the catheter (left side of each image) and the CTO (right end of each image) at 2 sec from injection. a) the intra-arterial pressure in the space between the catheter tip and the CTO is approximately 300 mmHg >3 times the normal arterial pressure (about 100 mmHg or 13 kPa). b) the novel method to synchronize injection and suction of saline significantly reduces the pressure increase in the pre-CTO space (overpressure) to less than 1 mmHg. The adjacent lumen catheter is used (Figure 2(c)). A small clearance gap exists between the catheter tip and the artery.

Injection of saline for flushing involves a pump that sets either the injection flow rate or the injection pressure. The two different strategies for saline injection for adjacent lumen catheter are analyzed: Constant pressure injection/suction vs constant flowrate injection/suction. Pulsatile arterial blood pressure is applied at the proximal artery boundary (artery opening on the left in Figure 3.3). For the case of constant flow rate, the injection and suction rates were synchronized so that the amount of fluid suctioned by the catheter per unit time is identical to the rate of saline injected into the artery. Throughout the study two different pressures are discussed: injection pressure and intra-arterial pressure. The injection pressure is the pressure applied by the pump, which acts on the lumens of the catheter. This pressure is not shown in the figures because it is found at the site of injection of saline into the catheter (outside the body's catheter insertion site) but is computed in our simulations. The intra-arterial pressure develops inside the artery, in front of the CTO, when saline is injected to flush the blood. When the pressure for injection and suction

are fixed, a large overpressure (intra-arterial) developed, especially when the catheter was located close to the atherosclerotic plaque, reaching values up to 300 mmHg (38 kPa). This overpressure was negligible, on the other hand, when saline injection and suction were controlled to maintain constant and equal flow rates. This disappearance of the overpressure has crucial significance in the clinical value of this saline flushing technique, as any overpressure outside of the normal physiologic systolic and diastolic values within the artery puts the atherosclerotic plaque and surrounding arterial tissue at risk of rupture. The clearance time for both control strategies were within 2 s of each other, with faster clearance by 0.2 s in the constant flowrate injection/suction modality. This study demonstrates the feasibility and advantages of saline flushing with this catheter design with adjacent lumens and the control strategy of synchronizing the suction and injection to maintain constant and equal flow rates.

3.3 In vitro experimental results

(a)

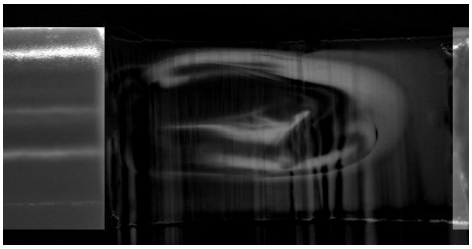

(b)

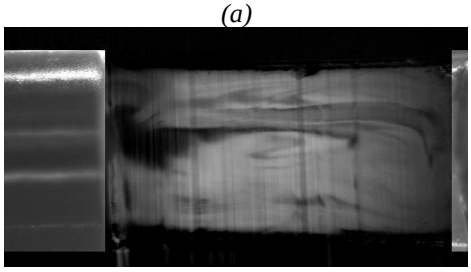

(c)

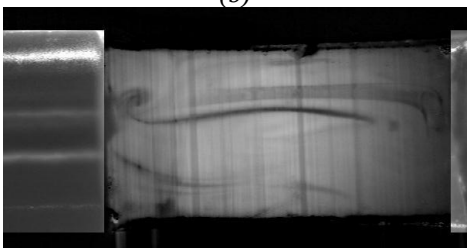

(d)

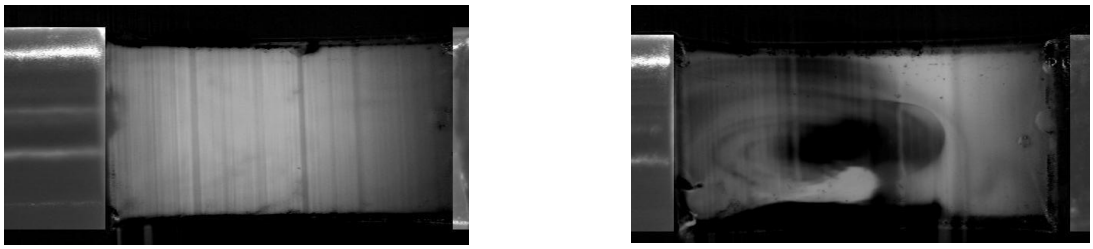

(e) *(f)*

Figure 3.4: Images showing the clearance of blood-mimicking fluid (dark) using saline solution (bright) at a flow rate corresponding to Re = 140 at the exit of the infusion lumen. The catheter housing the suction and injection lumens (adjacent to each other, Figure 2(c)) is on the left, and the CTO is on the right. As synchronized saline injection and suction progresses, the amount of clearance (bright) increases until complete clearance is seen from quasi-uniform bright concentration (in e). Image acquisition times from start of injection: (a) 0 sec, (b) 1 s, (c) 2 s, (d) 3 s, and (e) 3.4 s. For flow Re = 70 (f) a small recirculating region exists, which collapses eventually (>6 s) leading to clearance.

The experiments demonstrate that complete clearance of blood using the proposed synchronized suction-injection technique is completed in times consistent with clinical requirements, as seen in Figure 3.4. The two lumens were placed adjacent to each other (Figure 3.2(c)). For a fixed stand-off distance (distance between the catheter face and the CTO) of about 3.3 mm, the flow rates were varied to achieve three different Reynolds numbers: 210, 140 and 70, defined with the velocity, lumen diameter and viscosity at the catheter injection outlet. The optical clearance times were 3.1 s, 3.4 s, and 7.2 s, respectively. The clearance times were measured by plotting the percentage of "cleared" area, defined as pixels with a brightness intensity higher than 95% of the maximum (nearly pure saline) against time, and then setting a threshold at 99% of "cleared" area. Due to an anomaly in the largest Reynolds (Re = 210) the experimental threshold was set to 95% for the experiments since it provided a more robust threshold as seen in Figure 3.5(a). The cleared area curve follows a sigmoidal distribution and flattens out when most of the area (representing the volume between the catheter center and the CTO) has been flushed of blood and replaced with transparent saline, as seen in Figure 3.5(a). When the injection-suction flowrate was reduced to the

minimum value (Re = 70), a small recirculation region was formed at the center of the lumen (visible clearly in Figure 3(f), while the injection-suction cleared the area near the wall of the artery and CTO, the center of the lumen was still opaque (dark) due to the recirculation of blood that "escaped" the clearance by avoiding mixing with saline in this low Reynolds number recirculation. This vortex persisted for a few seconds before collapsing when full clearance took place. Additionally, the stand-off distance was varied to 2.8 mm, 3.3 mm, and 4.1 mm, for the injection rate corresponding to Re= 140. The clearance times for these three stand-off distances were 2.8 s, 3.1 s, and 3.4 s (the corresponding cleared volumes were 16.1 mm^3, 18.9 mm^3 and 23.5 mm^3).

3.4 Experimental comparison with CFD simulations

In the first analysis of the CFD simulations, the time for the saline injection to achieve a mass fraction ≥ 98% (vertical dashed lines) everywhere in the plane of interest is considered the time required for optical clearance. Ray tracing analysis refines this estimate and will be discussed later. The experimental and computational studies were conducted for the same sets of parameters and catheter design values. These experiments bind the uncertainties under realistic conditions. The simulations are done under realistic conditions such as, perfectly steady suction and injection pressures, absence of flow fluctuations, smooth geometries etc. These imperfections are accommodated within the experiments which helps complement the CFD simulations.

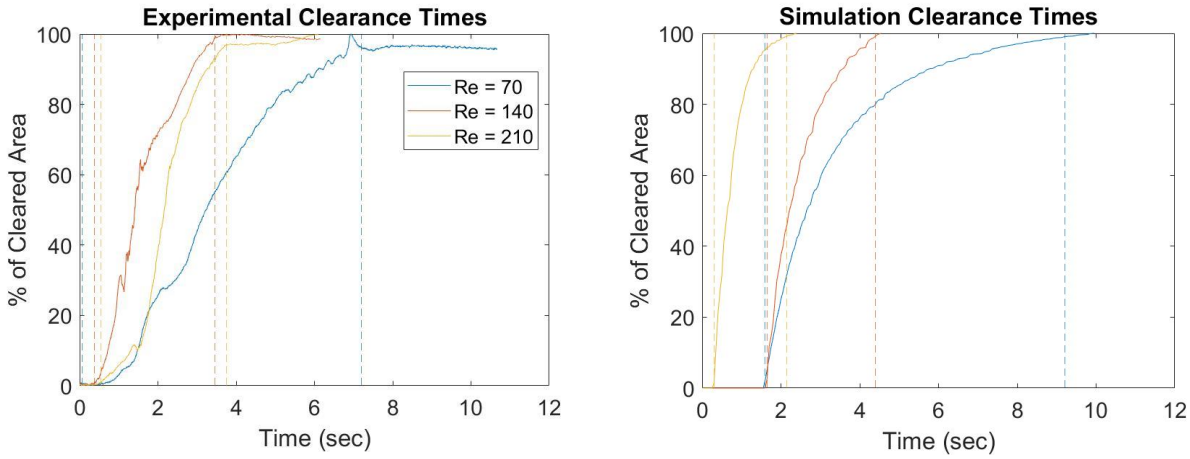

(a) *(b)*

Figure 3.5: Comparison of the percentage of area cleared as a function of time, for simulations and experiments. The dashed lines are thresholds between when the time flushing starts and when clearance is considered complete. The interval between the same color lines is considered the clearance time.

The experimental clearance times were compared with the results from the simulations, defined in the same way. The clearance times for Re = 210, 140 & 70 were 1.85 s, 2.75 s, and 7.6 s, respectively. Compared to the experimental values of 3.1 s, 3.4 s and 7.2 s, we observe good agreement for the lower Reynolds numbers (less than 20%), with a slightly larger discrepancy for the highest Reynolds number studied. This discrepancy is discussed in section 3.5.

3.5 Optical experiments using blood phantoms

The scanning fiber endoscope (SFE) was used to perform in vitro experiments that provide an optical insight into the study. While the PLIF experiments use a blood phantom composed of water, glycerol and salt that match the density and viscosity of blood, the solution does not mimic the optical properties of real blood. A solution of Intralipid 20% and India ink in water was used to create a blood phantom. The intralipid solution mimics the light scattering properties of blood and the India ink mimics the light absorption properties. This phantom is injected into an artery lumen, with the SFE and suction injection lumens.

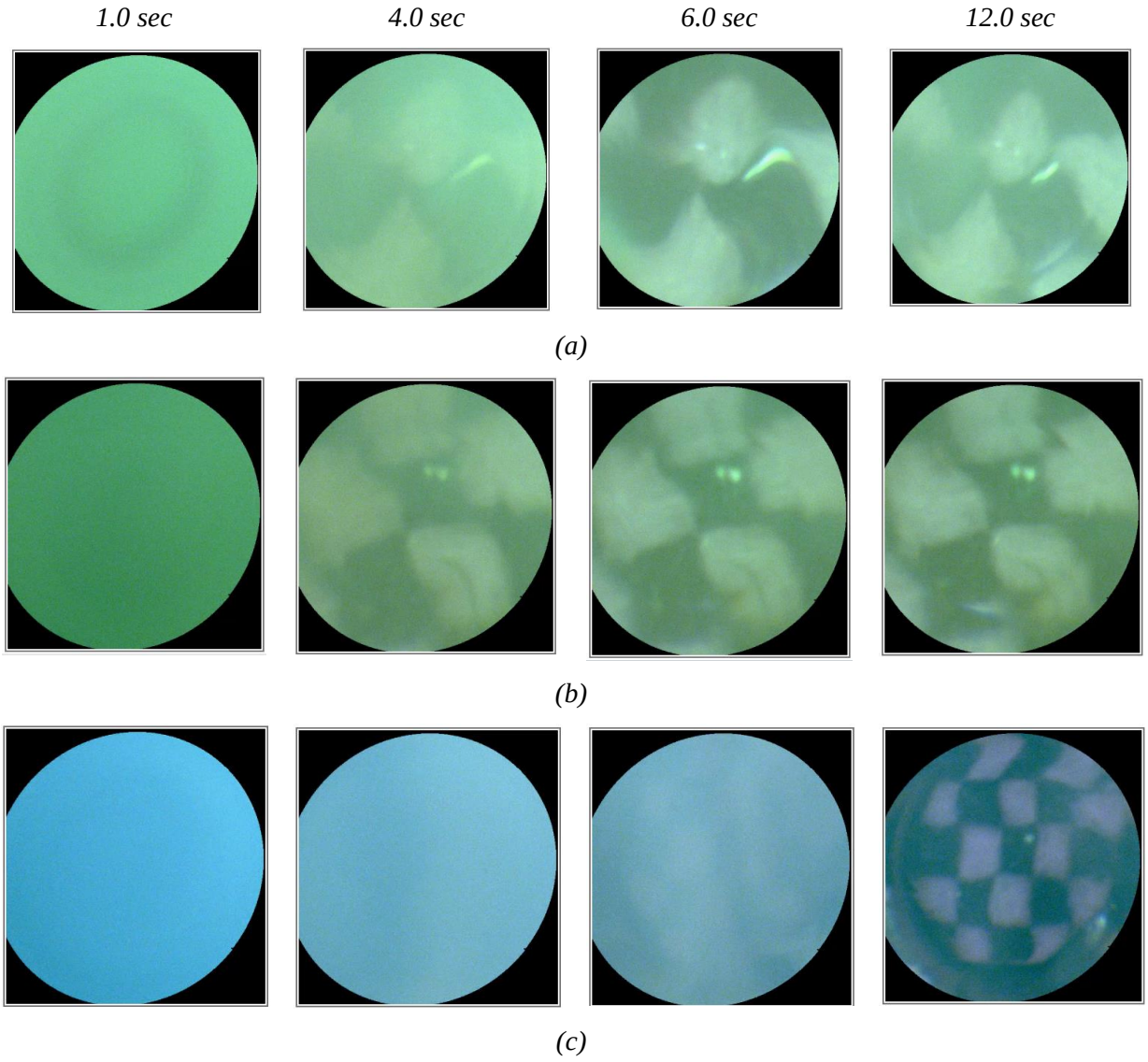

Figure 3.6: Images acquired using scanning fiber endoscope and two suction/injection lumens during in vitro experiments using a silicon artery phantom and a blood phantom (solution of water, India ink and intralipid 20%). Using a synchronized flow rate of 1.68 mL/min for suction-injection, the stand-off distance between the catheter and the checkered target (occlusion) was (a) 4.37 mm, (b) 5.37 mm, and (c) 6.37 mm.

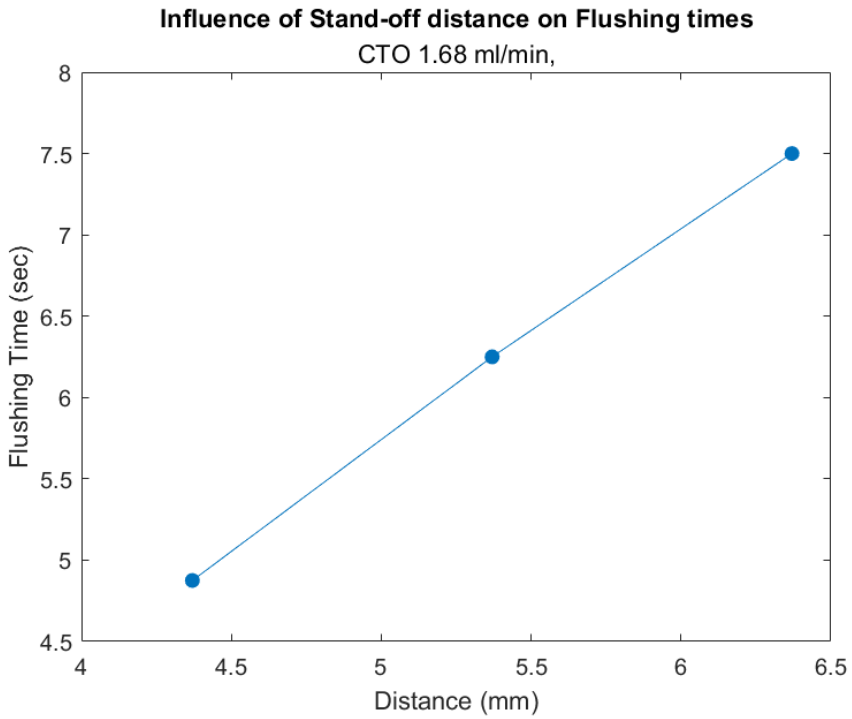

Figure 3.7: A linear relationship exists between stand-off distance and flushing times. As the distance increases, the volume of blood required to be flushed increases proportionately, resulting in increasing flushing times within the same fluid regime.

With a synchronized suction injection flow rate of 1.68 mL/min, the stand-off distance (between the catheter and the CTO) was varied between 4.37 mm, 5.37 mm, and 6.37 mm. As the distance is increased, the time required to flush the blood increases linearly as seen in Figure 3.6 and Figure 3.7. The increasing time for flushing is balanced out with a larger field of view of the CTO, possible at larger distances. This shows that the suction-injection catheter can be used for greater stand-off distances.

3.6 Discussion

Atherosclerosis causes development of plaque and can result in the formation of CTOs. Among the different existing techniques such as MRI, CT, ultrasound, OCT etc., diagnoses and treatment

of CTOs can be done using vascular endoscopy.[41] To image the CTO, clear saline solution is injected to flush the blood and provide a transparent imaging medium between the catheter imaging instruments and the CTO. Once the blood is flushed and clearance is achieved, visualization of the CTO begins immediately. The injection of saline can be continued to maintain the clearance till either the occlusion is completely imaged or treatment of the plaque using a laser is performed on the occlusion to clear the blocked artery.[26] Recognizing the factors involved in the entire process provides understanding to develop new and improved catheters, as well as to solve complications that can arise during the procedure. This study elucidates some effects of the parameters involved in the process of saline flushing in different albeit highly simplified geometries. Nonetheless, these results provide insight into a novel method for controlling catheter-based saline flushing.

Although, a shorter clearance time is preferred, since it reduces the risk of ischemia especially in open arteries, single interventions for 25-30 seconds in the artery under endoscopy is considered inconsequential. At low flow rates, this results in low blood dilution and is acceptable by clinical standards.[49] Therefore, a clinical benchmark for catheter-based saline flushing is obtaining clearance well below this amount of time to allow for safe visualization of the plaque and the artery wall by the interventional clinical team. During interventional procedures that may last more than a minute, a series of clearing events of brief duration would be required to visually guide therapy. In arteries containing CTOs, the flow is already obstructed, and the tissue obtains blood from other vessels, so the risk of ischemia may not exist for prolonged clearing. However, short clearance times are still useful since these reduce intervention risk, as well as associated costs of the procedure, both in economic and resource availability terms. The experiments and numerical

simulations in this study aim to study the process of blood flushing using injected saline and obtaining clearance within clinically relevant times.

The experimental study verifies the proposed synchronized suction-injection system working in vitro under controlled flow rate conditions. The synchronized system can provide sub-second clearance times for visualization of the CTO. Clearance has been demonstrated for a wide variety of flow rates (Re = 210, 140 and 70). At lower flow rates, as expected, the clearance times are longer. However, an interesting observation is the development of a thin blood recirculating region, which persists for a few seconds before collapsing and disappearing, resulting in full clearance. There appears to be a non-linear relationship of the clearance time with the flow rates. This is due to the mixing of saline and blood, which results in blood's dilution, after which the blood/saline mixture is cleared. This mixing of blood and saline is not directly proportional to the Reynolds number of the flow, hence it non-linearly affects the clearance times. This contrasts with non-mixing clearance of volumes, where the clearance time is more linearly dependent on the injection/suction flow rate (Reynolds number) as the injected fluid simply pushes blood out of the catheter-CTO gap. The experiments were also conducted for a small range of standoff distances, and a linear relationship is recorded between clearance times and standoff distance. This is easily explained since only the volume of the clearance region is changed while the Reynolds number is kept constant. The experiments were then compared with simulations to understand the accuracy of the simulation study. The effective clearance provides confirmation of the innovation and verifies optimal performance of the endoscopic-saline flushing system using blood surrogates that mimic the optical properties of blood, which will be conducted in a follow-up study.

The comparison of relative performance of the two different catheter control systems Figure 3.3(a), illustrate several advantages to the synchronized suction-injection system. In diagnosis or

treatment of the CTO, the catheter is usually manually driven into the artery. Thus, the standoff distance between the catheter and the occlusion depends on the catheter operation.[50, 51] In cases where the catheter is close to the plaque, a small volume exists between the catheter tip and the CTO. As shown in Figure 3.3(a), the pressure control system leads to the development of large pressures - of the order of about three times the normal arterial pressure – inside the artery which is already weakened due to atherosclerotic plaque. In contrast, as shown in Figure 3.3(b), regulating the flow using the synchronized suction-injection system maintains normal arterial pressures. This control can be clinically implemented with the help of a syringe pump or dual power piston injectors with two syringe channels regulated to push and pull the syringe pistons. The synchronized suction-injection system additionally obtains slightly faster clearance. The coordination of the suction and injection enables the withdrawal of equal amounts of saline/blood mixture from within the artery and injected saline. The resulting avoidance of any overpressure in the use of the catheter prevents any risk of rupture of the coronary artery due to any mechanically stresses that may be induced in the arterial walls.[52, 53] Additionally, high pressures within the artery may result in dislodging of the CTO or its disintegration, also known as plaque fissure. Further complications can arise, which may lead to embolism and occlusion of smaller vessels. [54, 55] The innovative technique of using synchronized saline flow control may be able to completely avoid such complications.

Introducing higher flow rates and consequently higher jet velocities raises the concern of the possibility of fragmenting the CTO or even dislodging it from its location and pushing it further downstream of the artery into a new location.[53, 55] CFD studies have shown that catheter size, position, angle of injection and speed of injection are critical in dictating damage to the artery.[47] Maximum jet velocities occur inside the catheter just before injection and lower injection velocities

are preferred.[56] Increasing saline injection flow rate produces the expected pressure differences in the catheter lumen, as computed by Poiseuille flow in the lumen. The higher jet velocity results in faster clearance of the blood ahead of the CTO but increases the intra-arterial pressure and requires a higher injection pressure at the site of injection (usually the femoral artery).

While the initial annulus injection design provided extremely low overpressures within the artery, and manageable flushing times, the design of the catheter is inherently complicated from a manufacturing perspective. Producing an annular lumen in an extremely small catheter also reduced the space available for the optical elements used in the arterial endoscopy, and hence reduces the viability of this catheter in clinical applications. The introduction of the suction lumen improves the saline flushing mechanics. Additionally, reducing lumen size for saline injection, enabled by the suction lumen, increases the area that can be occupied with optical diagnostic tools, and plaque removal apparatus, within the catheter. This also opens venues to reduce the catheter size to maintain an appropriate ratio between the catheter and artery diameter. Thus, the suction lumen enables flushing of blood in smaller arteries which may not have been possible with earlier designs. An alternate arrangement to the position of the injection and suction lumen was investigated while studying the effect of different diameters for the lumens. The advantage of placing the two flow lumens adjacent to each other in the catheter is that this configuration provides a larger surface area in the catheter for the imaging elements.

Chapter 4

MORPHOLOGICAL VARIABILITY

Partially occluded arteries & occlusions near bifurcations

Operational variability in the diagnosis of plaque is common and depends on plaque morphology where complete or chronic total occlusions (CTOs) can be successfully visualized via the novel technique discussed in the previous chapter. This chapter of the study aims at expanding the understanding of saline flushing for partially occluded arteries which are more common than CTOs but present a new set of challenge wherein the flow of blood is reduced but still existent. An upstream proximal balloon occlusion can be used to plug the artery prematurely but infusion of saline in such cases has led to problems related either with the high-pressure infusion of saline or inflation of balloon or both.[24, 44, 45]

In this chapter, the hemodynamics of saline flushing of partially occluded coronary arteries is investigated via in vitro PLIF experiments and numerical simulations. Subsequently we review preliminary simulations to explore the hemodynamics of occlusions near bifurcating arteries with

some optical analysis to confirm clearance of the artery. Finally, the observations of this section of the study are reviewed, and the significance of the results are highlighted with direct correlation to clinical applications.

4.1 In vitro PLIF experiments – influence of flow rate

Experiments show the flushing of blood leading to clearance by dual injection of saline without the use of an upstream balloon occlusion with flushing times well within the clinical requirements (for experimental setup see section 2.1 & Figure 2.1). Flushing time is defined as the time from saline injection to complete clearance between the catheter (or lumens) and the occlusion. The top-view images show gradual growth of the 'plaque' within the arterial phantom resulting in an eventual constriction of the artery as in Figure 2.5. Pulsatile patient derived flow rate-based blood mimicking fluid enters the artery. Saline is injected via the two lumens at a constant flow rate (Figure 3.2 (d)). With an injection Reynolds number of Re_{inj} = 1200, the saline pushes the blood, dilutes it, and clears the volume between the lumens and the 'plaque' resulting in complete visualization of the 'plaque'. Furthermore, it maintains this clearance due to continuous injection of saline and prevents fresh blood mimicking fluid from re-entering into the cleared volume. At injection Reynolds number of Re_{inj} = 600 the injected saline pushes the blood and clears the volume between the lumen and plaque, however, as the blood pressure in the arterial phantom increases from diastole to systole fresh blood mimicking fluid enters the volume re-obstructing the visualization of the plaque. This happens during 30% of each cardiac cycle, where the plaque is visualized for 60% of the cycle. A similar effect is seen at an injection Reynolds number of Re_{inj} = 300, where the time of complete clearance is reduced to 30% of the cardiac cycle. At all three injection Reynolds numbers, the flushing times to achieve clearance are well within the clinical requirements of less than 20 s. A linear relationship is observed between the flushing times and

injection Reynolds number as the flow is within the same flow regime as seen in Figure 4.1. At an injection Reynolds number of Re_{inj} = 150, the saline injected is unable to overcome the high-pressure blood mimicking fluid pumped into the artery even at diastole. This leads to incomplete clearance of blood and incomplete visualization of the plaque.

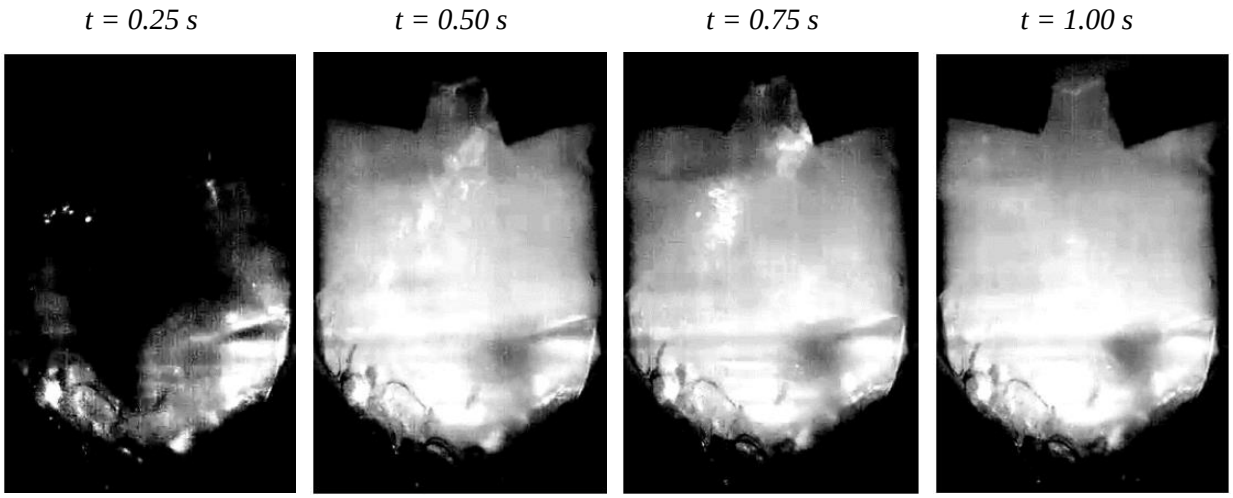

(a)

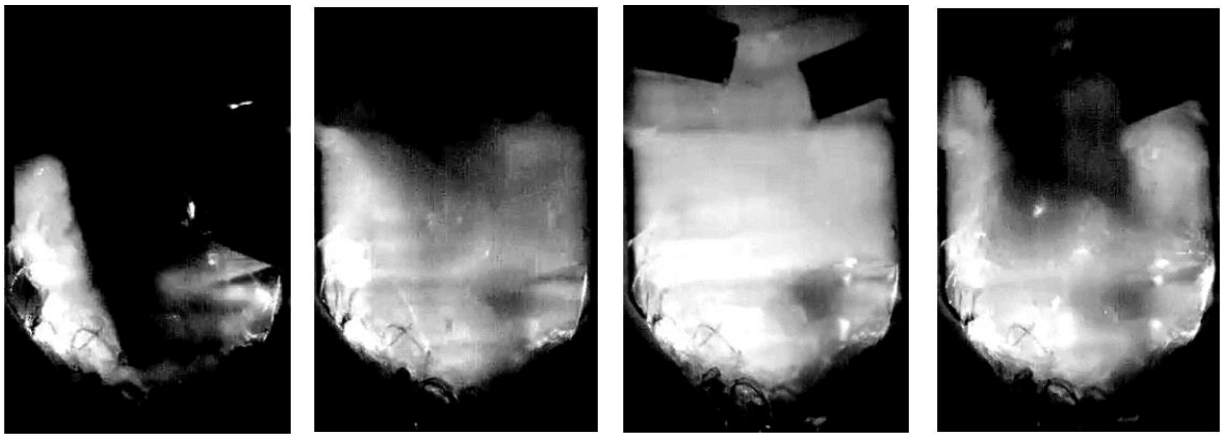

(b)

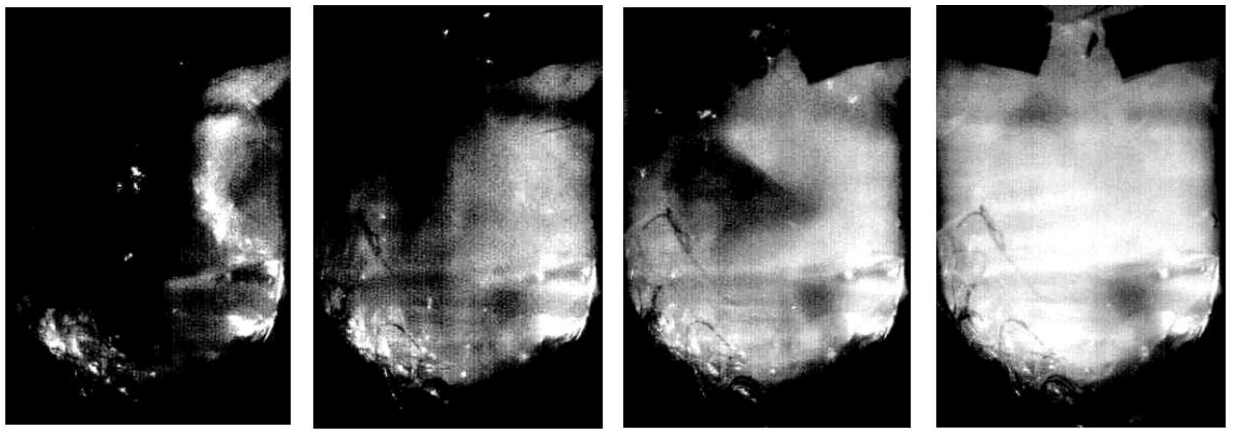

(c)

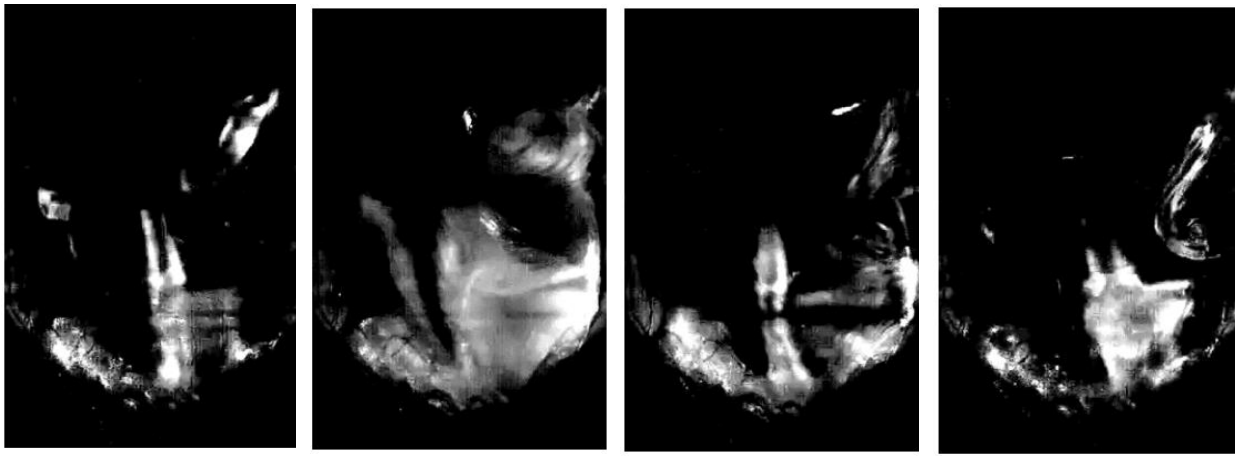

(d)

Figure 4.1: Images show the clearance of blood in a partially occluded coronary artery phantom. Blood mimicking fluid is pumped via a pulsatile pump into the artery where two hypodermic needles of 0.3 mm diameter are inserted (easier to spot at t = 0.75 s for both (a) and (b)). Saline dyed with rhodamine B is injected via both lumens to flush blood and clear the artery, which can be seen as the rhodamine emits fluorescence when excited by the laser plane. At (a) Re_{inj} =1200, saline flushes the blood and maintains clearance while fresh blood is unable to enter the optical region. However, at (b) Re_{inj} = 600 and (c) Re_{inj} = 300, saline injection results in the dilution of blood achieving clearance, but as blood pressure increases from diastole to systole, blood enters parts of the region resulting in partial clearance. With variation in blood pressure, clearance and visualization of the plaque and artery cycles. At (d) Re_{inj} = 150, the saline is unable to overcome the pumped blood.

4.2 In vitro PLIF experiments – influence of stand-off distance

As clinicians may be unaware of the proximity of the plaque from the catheter, the stand-off distance was increased from 5 mm to 7 mm and also to 11 mm for an injection Reynolds number of Re_{inj} = 1200 and linear relationship was observed between flushing times and stand-off distance. This can be explained by a linear increase in the volume of blood required to be flushed with increase in stand-off distance while the fluid flow is in the same regime. Additionally, in a specific case where misalignment of the injection lumens occurred as shown in Figure 4.2(c) due to human error during the experimental setup, saline injected from one lumen interfered with the other lumen resulting in incomplete clearance of blood. While experimentally this may occur at all stand-off distances, the effect is unnoticeable when the catheter is close to the plaque. However, at large stand-off distances ≈ 11 mm, this interference can prevent complete visualization of the occlusion as shown in the Figure 4.2(c).

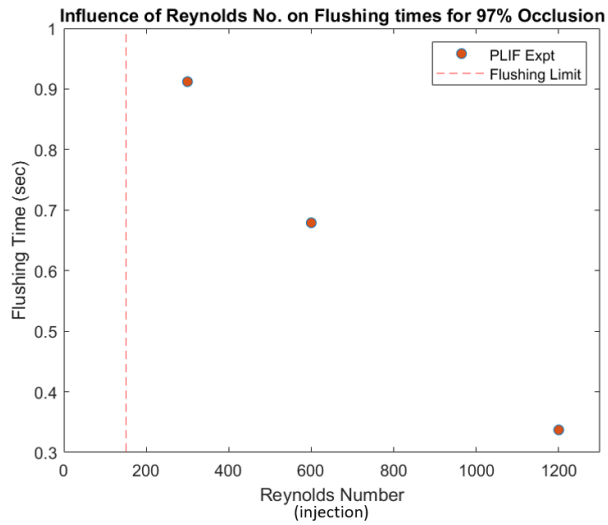

(a)

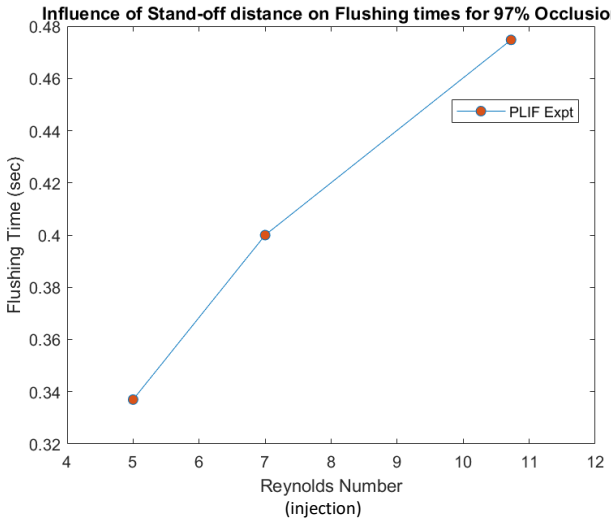

(b)

(c)

Figure 4.2: A linear relationship was observed between flushing times and injection Reynolds number. At Re_{inj} = 150 clearance is not achieved, denoted by the red dashed line. Flushing times also increase linearly with stand-off distance between the catheter and the plaque as the volume of blood required to flush increases linearly (b). At larger stand-off distances the orientation of the lumens plays a crucial role. This is seen in (c) where misalignment of lumens affected the saline injection (as show by this and that – explain because not clear to reader), leading to only partial clearance of the artery even at higher injection flowrates.

4.3 Numerical modelling - Influence of flow rates

CFD simulations expand the understanding of the local hemodynamics at play in and around the lumens, catheter, and the plaque. Figure 4.3 shows a central planar view of saline injection at injection Reynolds number of Re_{inj} = 300 in a 3.3 mm artery with a 97% occlusion via two 0.5 mm lumens, which matches the experimental conditions. Saline injected dilutes the blood as it mixes with it and uses its injection momentum to push the blood via the downstream arterial exit. Interestingly, as saline injection continues, saline additionally moves upstream. This is explained by the pressure map in the artery which shows overpressure varies between only 5-70 Pa above normal arterial pressure. This is a soft tamponade, of less than 1 mmHg inside the artery, that

prevents blood pumped from the heart entering the artery and avoiding saline flushing and optical clearing within one cardiac cycle. As soon as saline injection stops, blood flow is reestablished, in less than a second, avoiding ischemia. In comparison with the experiments for a 97% occluded artery, the simulations closely match the experimental data and exhibit the linear relationship previously observed between injection flowrates and flushing times.

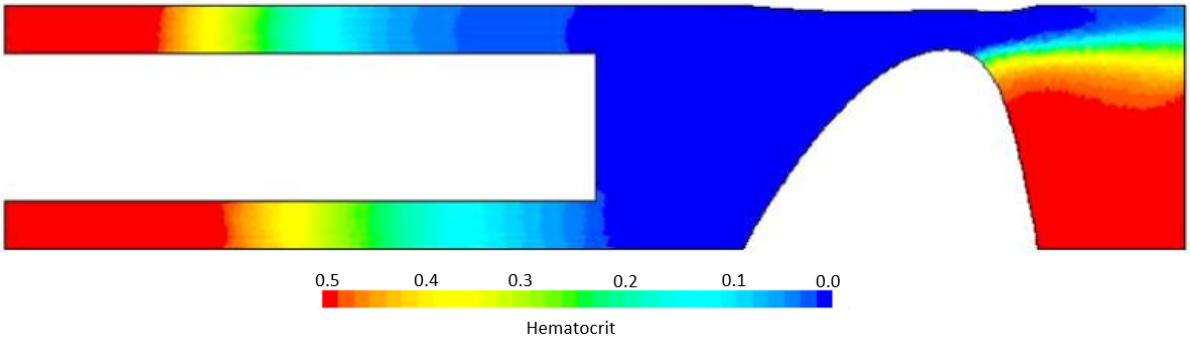

(a)

High pressure (Systole)

Low pressure (Diastole)

(b)

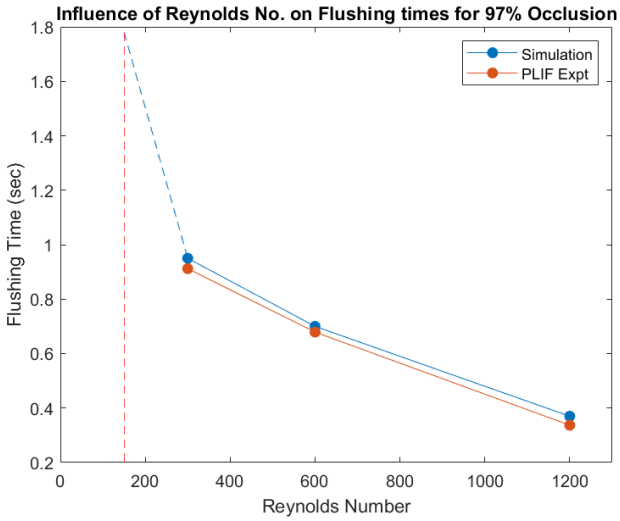

(injection)

(c)

Figure 4.3: Saline injection at Re_{inj} = 300 completely flush blood and provide a clear fluid volume between the catheter and the occlusion (a). As blood pressure varies between systole and diastole, (b) injection of saline into the partially occluded artery results in a soft tamponade with an over-pressure of only between 70 Pa to 5 Pa. This overpressure prevents blood from entering the optical region and enables clearance of the artery. In comparison with the experimental results, (c) the simulations show a similar linear relationship between flushing times and injection Reynolds number, with a slight increase in the simulation flushing time values.

4.4 Flow physics of saline flushing in a partially-occluded artery: the role of saline "tamponade"

As the pressure in the artery varies from systole to diastole the flow of blood matches this change Figure 4.4 at t < 1.7 s. When saline is injected into the constricted artery at t > 1.7 s, both the upstream and downstream arterial openings see an increase in fluid flow due to the conservation of mass but interestingly a larger volume of saline and blood exits upstream of the artery which prevents new blood to enter the volume of interest and impede the clearance of the volume. This reversed flow of blood and saline occurs due to the presence of the occlusion itself which is seen in the comparison of partially occluded and healthy (unobstructed) artery. In the latter case, as saline is injected into the completely un-occluded artery at t > 1.7 s, all the saline injected exits the downstream arterial exit with no change in flow at the upstream arterial opening, which is in stark contrast to what is observed when saline is injected into a diseased partially occluded vessel.

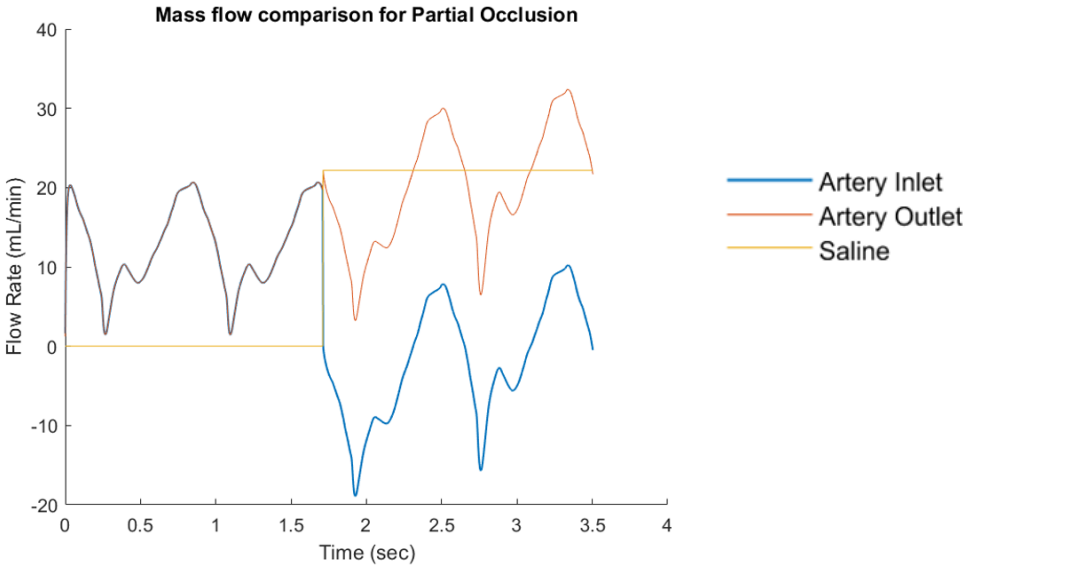

(a)

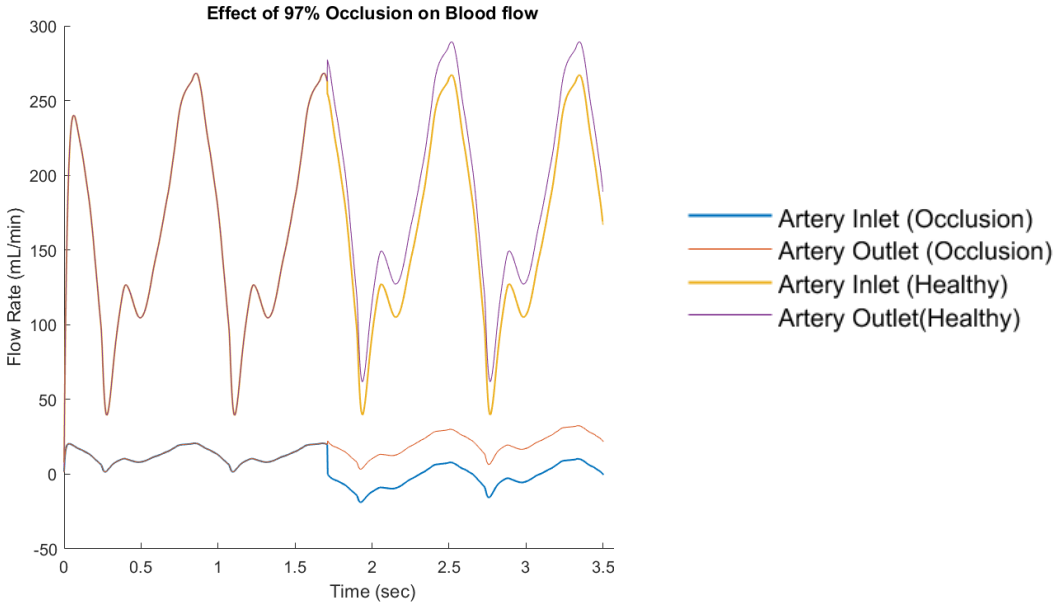

(b)

Figure 4.4: Saline injected into the diseased artery at time t > 1.7 s results in reverse flow at the upstream arterial opening. The fluid overpressure developing in the artery increases both flow downstream and reversed flow upstream preventing fresh blood from entering the optical region (a). This contrasts with what happens if saline is injected into a healthy artery (b), where the flow upstream remains unaffected and only increased flow is seen at the downstream arterial opening.

4.5 Influence of Plaque size

If the size of the plaque reduces from a total occlusion, and the artery lumen restriction becomes less pronounced, more blood flows through the artery, and potentially saline, altering the efficiency of saline flushing. Previous injection Reynolds numbers may not necessarily lead to flushing of blood and complete clearance as seen in Figure 4.5. Saline dilutes the blood but is carried away from the narrowing through the downstream arterial opening, after mixing with the blood entering the artery proximal to the narrowing. This confirms that there is a limiting threshold over which the injection Reynolds number must be to achieve clearance based on the size of the atherosclerotic narrowing. This is the direct result of change in the pressure inside the artery which is dictated by the size of the constriction. With reducing pressure drop over the constriction, saline injection leading to flushing is more difficult. Additionally, flushing times increase with reduction in size of the narrowing.

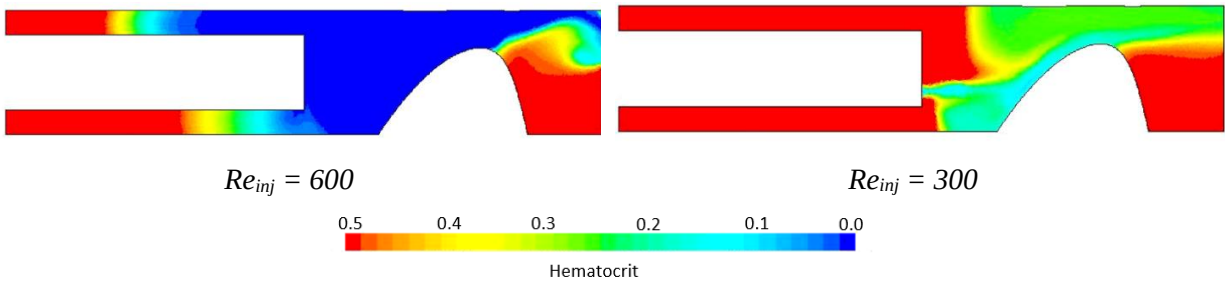

(a)

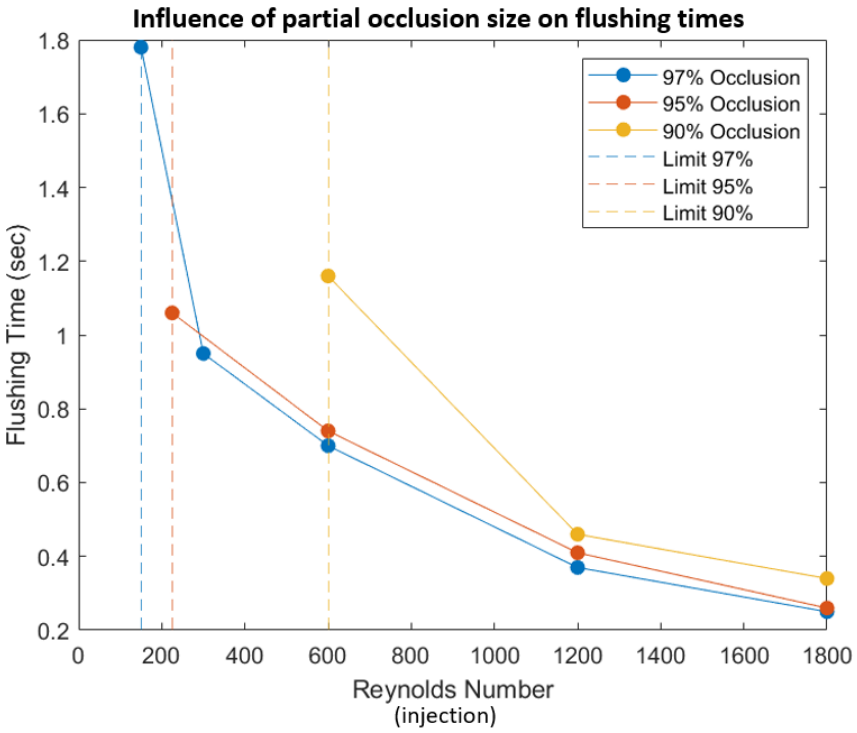

(b)

Figure 4.5: A lesser narrowing results in increased flow of blood/fluid through the artery. This makes saline injection for visualizing the plaque and the treatment more challenging. With a 90% narrowed artery (a), injection Reynolds number of Re_{inj} = 600 produces clearance while Re_{inj} = 300 is unable to flush the blood to achieve clearance. This suggests an injection threshold exists above which the injection flowrate is required, and the threshold is dictated by the size of the narrowing (b).

4.6 Stand-off distance

The stand-off distance dictates the volume of blood that needs to be cleared to visualize the partial occlusion. As stand-off distance increases, there is a linear increase in flushing times, as the volume of blood to flush also increases linearly and the fluid regime continues to be the same as seen in Figure 4.6. These results are in close agreement to what was seen earlier in the in vitro experiments and are well within clinically relevant flushing times (< 20 s).

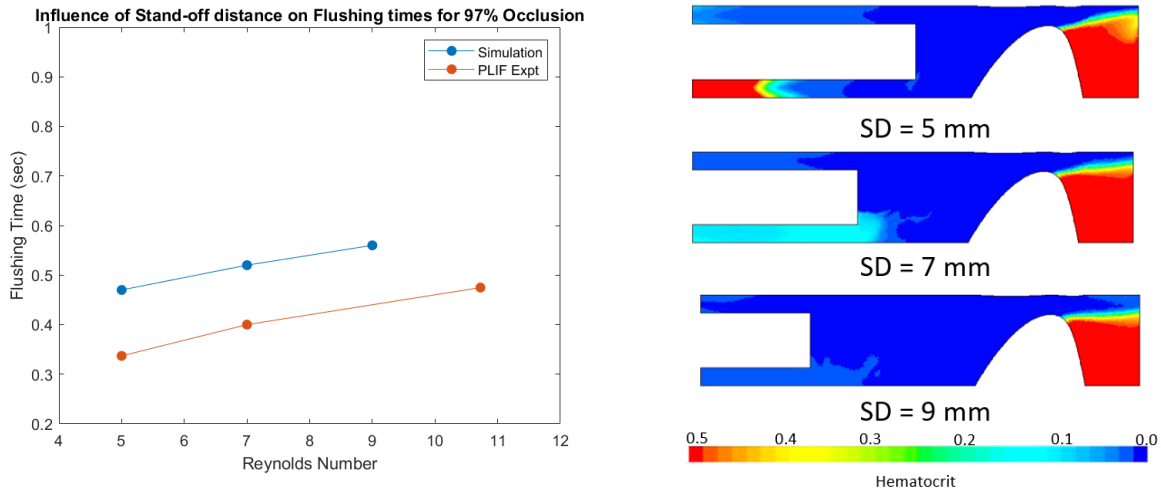

(injection)

(a) *(b)*

Figure 4.6: (a) The simulations confirm a linear trend in flushing times and injection flow rates like what is observed in experiments. The flushing of blood at longer stand-off distances (b) between the catheter and the occlusions enables clinicians to be further away before injecting saline.

4.7 Orientation of the catheter

The position of the catheter and injection lumens were simulated to observe if clearance required flushing closer to the occlusion than the arterial opening between the plaque. In Figure 4.7, we see the difference in the flow patterns between injection at 0 deg (lumens are closer to the plaque) vs 180 deg where the lumens are closer to the opening. Interestingly, the lowest flushing times are observed when the injection lumens are at the top or directed towards the arterial opening as opposed to the plaque which is counter intuitive to what may originally be assumed. Flushing times increase as the catheter is rotated with lumens on the side. The major implication of these results reduces concerns from clinician about the feasibility of saline flushing when the catheter distal tip does not point towards the plaque.

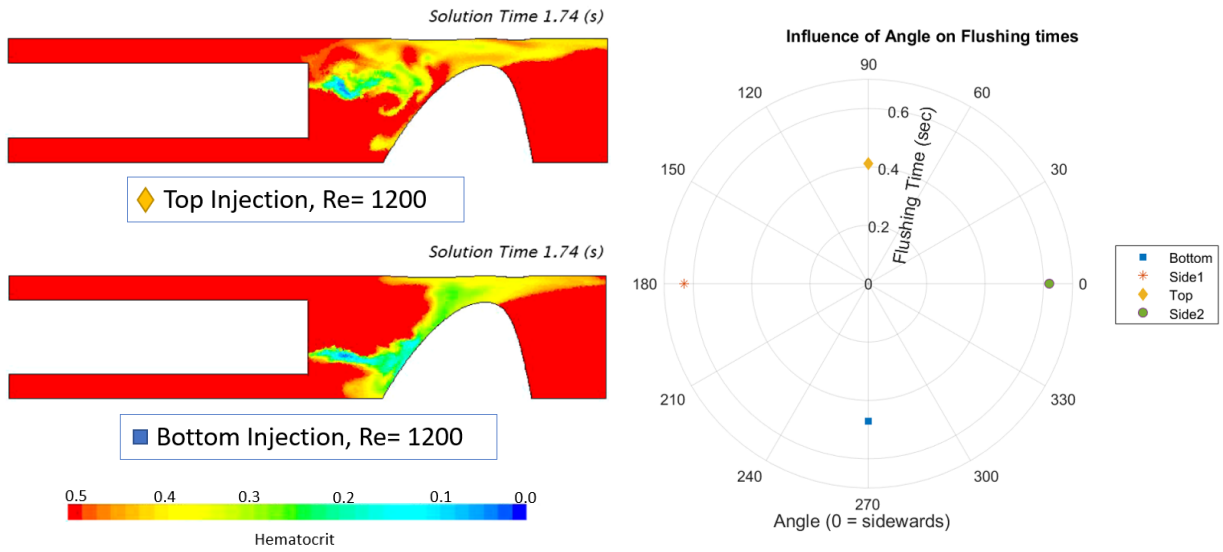

(a) *(b)*

Figure 4.7: The position of the lumens with respect to the occlusion has a small impact on flushing times (a). Interestingly, the lowest flushing times are when the lumens are directed towards the arterial opening which is located at the top. Injection of saline when the lumens are aimed sideways, results in an increase in flushing times.

4.8 Total occlusion near bifurcating arteries

Major coronary arteries frequently branch out into smaller arteries with provides the heart with opportunity to bypass blood from blocked arteries. However, the blocked arteries may be critical and require treatment. From a fluids perspective such blocked bifurcating arteries present a mixed problem where the blockage is a closed system due to the CTO, but the bypass artery allows antegrade blood flow through the arterial network acting as an open system, thus presenting a new challenge for the saline flushing catheter, and for achieving optical clearance.

Catheter placement

Since the occlusion is completely blocked, the synchronized suction-injection system was employed for achieving clearance. The catheter was placed upstream of the bifurcation as show an

in Figure 4.8 and saline was unable to flush the blood. Blood pumped from the heart forces the saline injected to flush into the bypass artery, with little blood flowing into the occluded artery. Hence the catheter was pushed further downstream beyond the bifurcation into the occluded artery at 2 mm and 4 mm distance from the bifurcation. At both 2 mm and 4 mm distances, the saline injected would flush the blood, but would get entrapped by pockets of antegrade blood and be pushed into the bypass artery or the un-occluded circumflex artery. This occurred due to the high injection rates of saline into the artery.

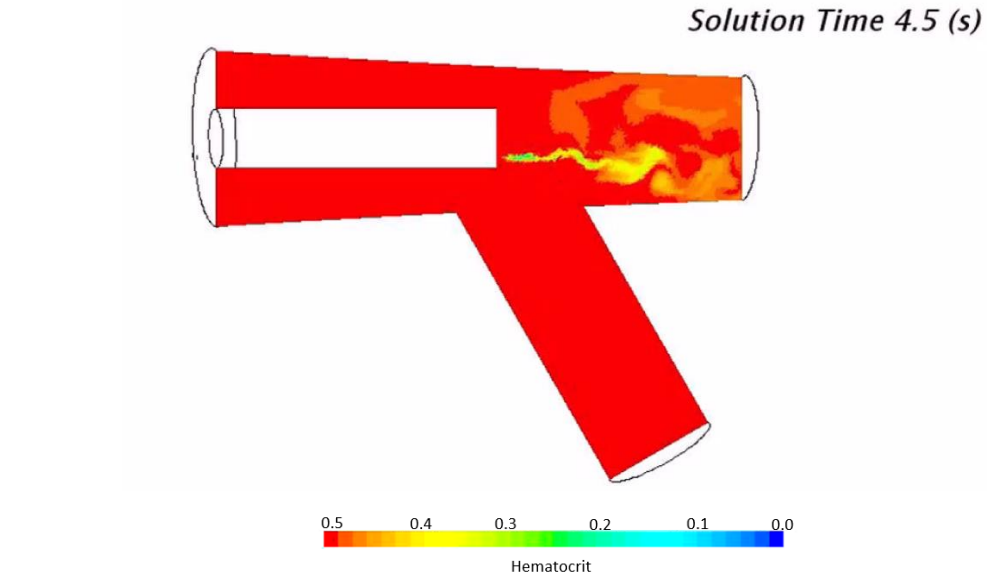

(a)

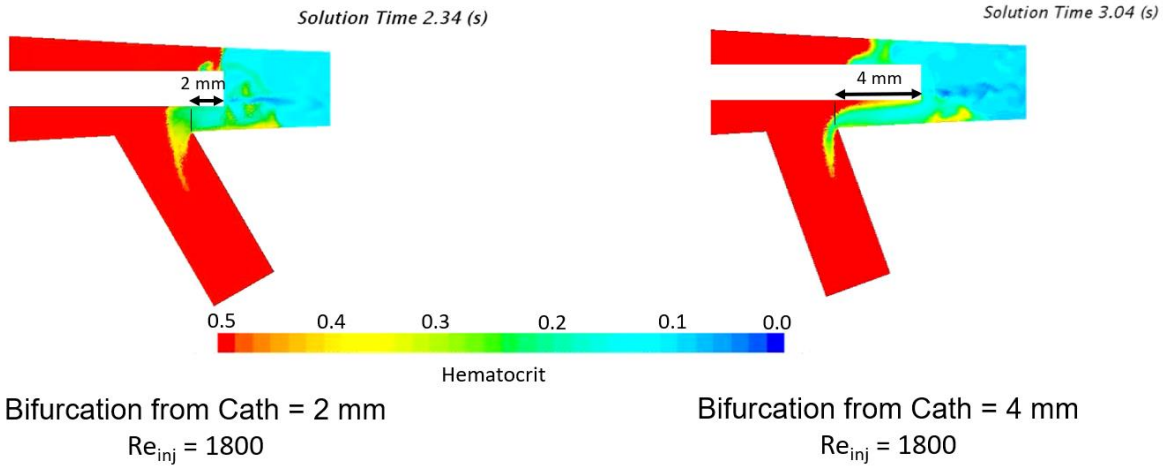

(b) *(c)*

Figure 4.8: Flushing of blood for occlusion near bifurcations. When the synchronized suction-injection is employed, the catheter cannot be placed upstream of the occlusion as antegrade blood prevents any clearance from taking place (a). Saline injected dilutes the blood when the catheter is pushed further downstream into the artery at (b) 2 mm and (c) 4 mm beyond the bifurcation. However, saline still gets trapped by pockets of blood and is pushed into the bypass artery at such high injection flow rates.

To avoid the problem of losing saline into the bypass artery, the flow rates were reduced to Re_{inj} = 150 and Re_{inj} = 300. While injection of saline at Re_{inj} = 150 restricted the saline between the occlusion and the face of the catheter, it only diluted the blood to about 10% hematocrit. With an injection Reynolds number of 300, however, increased dilution of blood was observed, as seen in Figure 4.9. To identify if the occlusion can be visualized, an optical analysis was performed (see methodology, section 2.6) on the complete occlusion for Re_{inj} = 300 and compared to the simulation results (planar view). We found partial clearance of the occlusion, which can be utilized by the clinician to diagnose the plaque characteristics by composing images of the occlusion collected over a series of short clearance "bursts". Thus, the synchronized suction-injection system can be used to successfully visualize occlusions near bifurcating arteries.

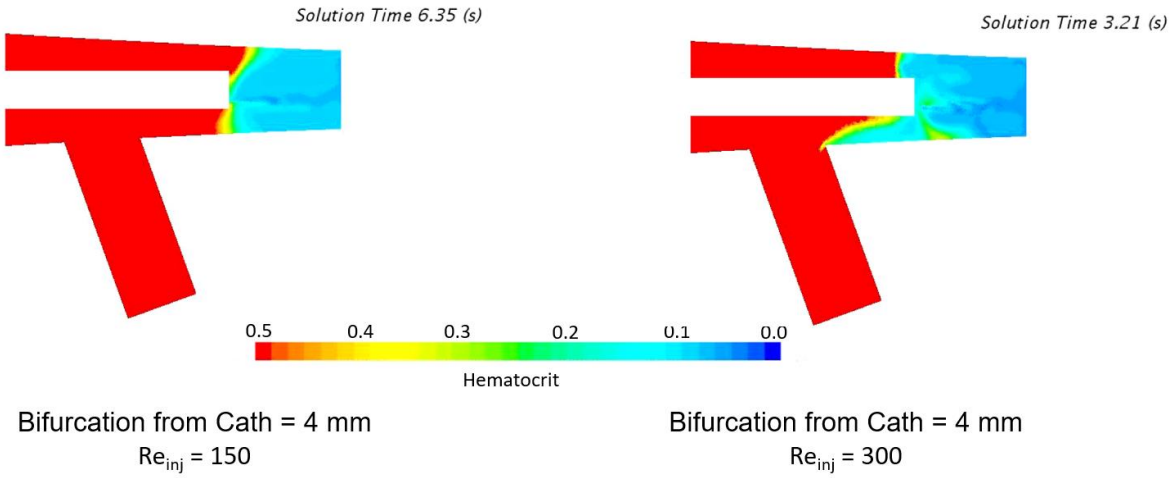

(a)

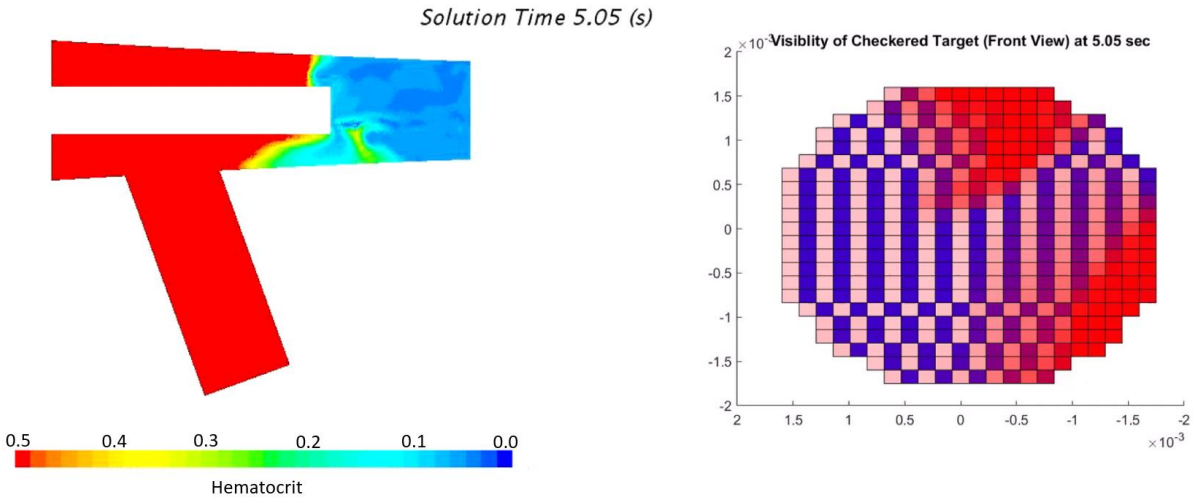

(b)

Figure 4.9: Lowering the injection flow rates to Reinj =150 and Reinj = 300 enabled the containment of a majority of saline between the occlusion and catheter, thus helping dilute and clear more blood. But since only partial clearance can be achieved, optical analysis was performed to observe if the occlusion could be visualized.

4.9 Discussion

Imaging of arterial wall and plaque requires flushing of blood to obtain a transparent optical medium uninterrupted by various constituents of blood. Understanding the flushing mechanics will enable efficient optical clearing of blood in a safe manner.[10, 14] While high-resolution visible light imaging is dependent on saline flushing to provide a clear optical imaging medium, OCT can image even with the use of a contrast agent to flush the blood, providing a uniform medium to image the artery although at lower resolution.[19, 35, 36, 64] However, contrast agents are harmful to the body and radiation from non-invasive techniques should be minimized, which encourages using saline flushing along with minimally invasive imaging as an advantageous technique for plaque diagnosis.[10, 33, 34] Saline flushing additionally helps during laser atherectomy of the plaque during treatment as it provides a clear field for the treatment beam to

propagate and reach the plaque unobstructed, and can even act as a favorable cooling agent, compared to blood that may suffer damage, to stabilize temperature during ablation. [23, 25, 41, 65] Additionally, the forward viewing advantages of the scanning fiber endoscope encourage the study of saline flushing to enable imaging of the arterial wall.

Saline flushing is being actively studied to inspire product design and development of modern catheters. Currently, with advancements in optical system, the understanding of the fluid mechanics of catheters is a bottleneck for the technology to advance, as smaller optical elements are readily available, but high-pressure injection of saline can be harmful for patient safety due to catheter burst, or to diseased arteries. Innovation in optical technology with concurrent advancements in fluid systems will enable large strides in medical techniques.[12, 15, 16, 66] A lateral saline injection catheter was investigated computationally; flushing physics were influenced largely by the diameter of the artery and the saline injection flowrates. [40] Peak jet velocities were observed inside the catheter body just ahead of injection. These injection jet velocities can be reduced by introducing lateral holes along the injection lumen allowing saline to exit in the form of a plume instead of a jet at the tip of the catheter.[56] The plumes have lower velocity and are much safer in preventing any damage to the artery or dislodging bits of plaque that can lead to an embolism. A recent study, focused on the failure of catheters, proved numerically that catheter size, position, angle of injection and velocity of injection are critical in governing damage to the artery.[47]

A novel synchronized suction-injection catheter system proved to achieve optical clearance within clinically relevant times with zero over-pressure in the artery for diagnosis of chronic total occlusions via an angioscope, such as the scanning fiber endoscope.[67] The absence of any overpressure in the artery is critical to ensure a safe and complication-free procedure that can avoid

rupture of the artery or any dislodging of the plaque. In the case of a partially occluded artery, the advantage of a suction lumen is lost as antegrade blood flow interferes the injected saline and prevents flushing of the blood-saline mixture. Preliminary studies that used the SFE for coronary porcine and rabbit studies, employed a balloon occlusion to stop this antegrade flow of blood.[12, 15, 16, 66] This study circumvented this problem using dual injection via both lumens to flush the blood and expand the use of a dual lumen catheter for both partial and total occlusions.

In vitro experiments showed the effectiveness of a dual injection lumen system to clear a 97% partially occluded arterial phantom. Clearance is achieved due to as the local intraarterial pressure due to the saline, creates a soft fluid blockage preventing antegrade flow of blood, thus preventing the need of a balloon in the procedure. Lower injection flow rates (Re = 600 and 300) provided partial clearance as blood flow varied between systole and diastole, as seen in the experimental results (section 4.1, image 4.1) During this phase of clearance, video-rate high resolution images can be captured by the SFE or angioscope providing clinicians with sufficient detail of the plaque and the artery. All the above flow rates provide clearance in less than a second which is much shorter that clinical requirements of less than twenty seconds. Numerical simulations explained the soft fluid blockage and showed the pressure varies between 5 to 70 Pa due to the injection of saline and the presence of the occlusion. Additionally, the experiments also established the existence of an injection threshold for the working of dual lumen injection system in the absence of a balloon occlusion. Numerical simulations corroborated this injection threshold and showed the influence of occlusion size on the injection threshold. While occlusions are detrimental to the health of the patient, saline flushing is facilitated by their presence and enable the development of soft “tamponade” leading to clearance of the artery and visualization of the occlusion. The flow rates employed by this study are much lower than previous preliminary SFE studies, which tested

the efficacy of the SFE in non-occluded arteries thus requiring higher flow rates as explained above.[12, 15, 16, 66]

Saline flushing and forward viewing high-resolution imaging of the artery is proposed to be used adjunct with standard fluoroscopy or coronary angiography. However, with limitations in fluoroscopic resolution, the clinician may not accurately know the distance between the angioscope and the plaque. In vitro experiments in this study showed that dual injection of saline at an injection Reynolds number of 1200 can produce complete clearance all the way up to > 11 mm away from the plaque. This fundamentally provides room for the clinician to visualize the artery at a wider field of view to get more information of the plaque and gradually approach the plaque if needed for a more detailed perspective. Flushing at larger stand-off distances may reduce the exposure to radiation during fluoroscopy, as direct visualization of the plaque starts earlier (clinicians stops fluoroscopy and starts direct imaging even though the catheter is far from the plaque). Additionally, this results in reduced quantity of contrast agent used during the procedure. Flushing times increase linearly with increasing distance between the plaque and the catheter as the volume of blood required to flush increase linear and the fluid regime remains the same, with the increased flushing times within clinical requirements.

Coronary artery intervention procedures take place at various occlusion sizes.[68, 69] To understand the implication of plaque morphology, three different occlusion sizes were simulated. At an initial artery with a 97% occlusion, injection Reynolds number of 300 results in complete clearance. However, as the size of the occlusion reduces to 90% the same injection flow rate cannot flush blood away effectively to produce clearance. This means that injection flow rates must be above a minimum threshold to achieve clearance, and this threshold is dictated by the size of the occlusion, with larger occlusions having lower thresholds. Reduction in the occlusion size also

leads to increased flushing times as larger intra-artery saline pressures are required to flush increase antegrade blood flow. Flushing times also increase linearly with stand-off distances which is observed both numerically and experimentally. The increase in numerical flushing times is attributed to more accurate modelling of the lumen size which replicates the 0.3 mm diameter lumen for one meter length.

Finally, the variation of the orientation of the lumens with respect to the plaque shows that flushing times increase when the lumens are facing the sides of the occlusion and are neither opposite the arterial opening or at the bottom of the occlusion. The shortest flushing times are achieved when the lumens face the arterial opening instead of the plaque which is counterintuitive. Since orientation is crucial for reducing damage inside the artery, this may be the safest configuration to achieve clearance.[47] While flushing times vary with orientation, they are all well within clinically relevant times. However, as seen in the experiments, at large stand-off distances between the catheter and plaque, orientation of the catheter and the lumens plays a crucial role as incorrect alignment of the lumens can lead to interference of one injection jet with the other resulting in only partial clearance of the artery and partial visualization of the plaque. However, at shorter stand-off distances, the influence of the alignment is negligible as the lower volume of blood that requires flushing offsets any misalignment.

Chapter 5

CONCLUSIONS & FUTURE WORK

Saline flushing within endovascular catheters was performed for clear optical imaging of CTOs within a modeled coronary artery. Several parameters that affect the saline flushing of blood have been analyzed and discussed. To avoid development of large overpressures within the artery or in the catheter, a novel approach to saline control was implemented in this thesis. Instead of regulating pressure at the inlet and suction lumens, regulating and synchronizing the flow rates of injected saline and suction of the saline/blood mixture is proposed. This approach improves the previously existing technique for optical clearing, reducing the injection flow rates necessary and the associated intra-catheter pressures for saline injection. At the same time, it minimizes the overpressure inside the artery in the proximity of the CTO, drastically lowering the risk of rupture or dislodgment of the CTO within the artery. This control system was verified with in-vitro experiments and CFD simulations. The size of the saline lumens in the catheter needed for proper

flushing and clearance ahead of the CTO are minimized, allowing for a smaller total catheter diameter, while still allowing for the required optical (or other treatment) elements inside the catheter. Introducing a suction lumen within the catheter drastically changes the mechanics involved in the flushing technique. The flushing times become shorter with suction. It reduces both the intra-arterial pressure and the injection pressure required to infuse saline into the system. The saline flushing technique can be used for different arterial plaque geometries and CTO configurations that may arise within patients with atherosclerosis.

Saline flushing via dual lumen injection was performed via in vitro experiments for clear optical imaging of partially occluded vessels without a balloon inflation within an arterial phantom. Occlusion sizes were varied to represent a range of plaque morphology commonly observed in patients with coronary artery disease. Injection flowrates were varied to determine flushing times between injection and complete clearance of blood that led to a transparent imaging medium between the catheter and the plaque. These flushing times were well within clinically relevant times for different injection rates and distances from the plaque, thus confirming the feasibility of the proposed injection system for partially occluded arteries. Numerical simulations provided detailed information of the local hemodynamics within the artery. Additionally, he simulations modelled the thin lumens for 1 m (as expected in clinical conditions) and simulated the actual pressure drop in the system, which was not possible experimentally due to limitations in the experimental setup (experiments used hypodermic needles followed by larger lumens to facilitate the use of laboratory syringe pump with lower injection pressures). A close agreement was observed between the simulations and the experiments, with slightly higher flushing times in the simulations due to the longer lumen length. Additionally, simulations showed injection of saline in partially occluded vessels leads to a soft tamponade, involving an overpressure of less than 1

mmHg, which enables flushing of saline without the use of balloon occlusion to block the arterial flow. The orientation of the injection system plays a limited role in flushing time, but complete clearance can be achieved at all orientation of lumens with respect to the occlusion. The proposed dual injection system can be used as a safe and effected procedure for guided therapy of partially occluded arteries to improve treatment of coronary artery disease.

Limitations of the study

The study makes certain assumptions that limit the extent of the conclusions reached in this thesis. The experiments and CFD simulations were all performed on straight arterial models, as opposed to the curved and tortuous anatomy of the coronary arteries. Future work includes using patient derived arterial geometries for both simulations and experiments, which will represent more realistic scenarios.

The arterial walls in the simulations were modelled as non-deformable boundaries, while the experiments have a small distensibility which is an intrinsic property of the silicone model and does not accurately represent motion of the carotid artery walls in response to injection of saline. However, the small overpressures observed in the simulations suggest that these assumptions may not be a large deviation from the true case, where compliance of the atherosclerotic artery walls may play a limited role. The deformation of the coronary arteries due to the intrinsic displacement of the ventricular wall on which they lay, changing the curvature of their substrate within each cardiac cycle may be a larger effect on the flow inside the CTO, bifurcations or partially occluded arteries.

The simulations and experiments were conducted with blood mimicking fluid which matches the density and viscosity of the flow but do not incorporate the optical properties of blood. While the

optical properties are irrelevant when complete clearance is obtained and in the determination of flushing times, they will play a small role in the visibility of the occlusion when complete clearance cannot be achieved and while the flushing process is taking place. Saline was chosen as the only flushing fluid. Clinicians have used optically clear radiopaque contrast and low-density dextran solutions with angioscopes.[36, 46, 64, 70] The experiments used hypodermic needles inside the arterial phantom, but the lumen diameters (of the injection tubes) are increased thereafter to reduce pressure required to push saline into the models via a laboratory syringe pump. In clinical conditions, a readily available high pressure syringe pump can easily inject saline via constant diameter lumens which will be used in the actual system and have been theoretically verified to be within the pressure limits of available lumen materials. Finally, motion of the beating heart changes the morphology of the artery and this dynamic motion/movement have been ignored in the current study and are prospective goals of the continuing future work.

Future Work

In this thesis, occlusions near bifurcations were investigated via numerical simulations. The next steps would be to verify clearance in such arteries via in vitro experiments. Following this, experimental investigation is required of smaller catheter sizes that are in development, with smaller lumens at lower flowrates that can have operate within reasonable pressures of operation for endovascular catheters. The smaller catheter tip model may contain a guidewire extending from the distal tip and through the partially occluded artery to more realistically model the clinical procedure. The previous vascular models all used straight arteries, hence curved and tortuous arteries must be incorporated into future studies.

Atherosclerotic plaque is predominantly developed in coronary arteries which require visualization for treatment. However, the catheter system and the technology can be used as a diagnostic tool in

much larger arteries such as the aorta. Although these large arteries have much higher flow of blood and present a unique problem for optical clearance, their larger size enables the catheter dimensions to increase, resulting in a similar change in flow characteristics of injection and suction of saline and blood.

The analysis of the suction-injection catheter so far has been using idealized arterial and plaque models. The morphological dimensions are acquired from different literature and associated with fluid flow properties reported in previously published studies. However, actual morphologies are slightly different than straight sections with no wall imperfections as designed by CAD software. Through our collaboration with the Center for Cardiovascular Innovation (CCVI), patient specific models can be acquired. The acquiring technique currently used at the center is Optical Coherence Tomography (OCT), which straightens out the artery before acquiring the images. The lost curvature can be restored during post-processing. By modelling realistic anatomy, the influence of intricate nuances that exists in the arterial wall can be captured. This will provide a deeper understanding to saline-blood interaction in real patients.

The optical analysis shown in this report and published earlier works to a high degree on chronic total occlusions (CTOs). However, as with the expansion of the study to include curvature, patient geometry and partial occlusions, the optical analysis needs to be expanded and improved accordingly to accommodate for more complicated geometries.

The numerical study imposes rigid wall conditions for the arterial wall. While the simulated flow in the arteries accounts for the interaction of the change in pressure and wall distensibility to calculate the flow through the artery, the simulations don’t account for expansion or movement of the arterial wall due to injection of saline. Future work should include fluid structure interactions

that account for the arterial wall tissue and its motion, expanding the understanding of the fluid physics.

A major step in taking this technology forward would be to evaluate the proposed catheter system in animals through collaborations at the University of Toronto and the University of Michigan, thus laying the platform for series of studies required for FDA approval of the catheter system.

Thesis Part 2:

Transport and mixing in photo-catalytic oxidation of urea for a wearable dialysis system (POUR)

Chapter 6

INTRODUCTION

6.1 End Stage Renal Disease (ESRD)

Chronic kidney disease refers to the illness of the kidneys in either structure or function resulting in insufficient filtration of waste from the body. Initial stages of kidney disease are asymptomatic and can go undetected but is reversible. Accelerated advancement of the disease can take place over a few months, but generally takes years with some patients showing no signs of progression.[71] Kidney function is characterized by the glomerular filtration rate (GFR) which is the total fluid filtered by all the nephrons in the kidney per unit time.[72] When the GFR falls below 15 mL/min per 1.73 m^3, kidney function is unable to sustain life and leads to kidney failure. [73, 74] Kidney failure or end stage renal disease (ESRD) is recognized as the most serious result of chronic kidney disease characterized by reduced kidney function and currently leads to an

estimated mortality of 2.3 million patients due to lack of access to treatment. Nearly 4.9-9.7 million patients required kidney replacement treatments (KRT) with more than 2.6 million patients require transplant of a kidney, which is the final treatment option, from a donor, while.[75, 76] For patients with ESRD onset, a 5-year survival rate is 41% including transplants and 39% excluding transplants.[77] This includes the death of about 91,000 patients annually in the United States.[78] Recent trends suggest these numbers are projected to increase to 5.4 million patients annually requiring KRT in the next decade.[75, 76] Models have projected a rise in risk factors of kidney disease such as obesity, diabetes, hypertension etc. by 11-68%, resulting in an increase in ESRD prevalence by 29-68% in the US alone. [79] However, there are reportedly less than 10% of the number of dialysis systems needed.[80-82] The cost to care for patients is staggering with over $34 billion spent for patients with ESRD and a total of $100 billion for all patients with renal disease.[82] With increased incidence of ESRD and increasing healthcare costs, there is a fundamental need to investigate robust technologies for dialysis patients.

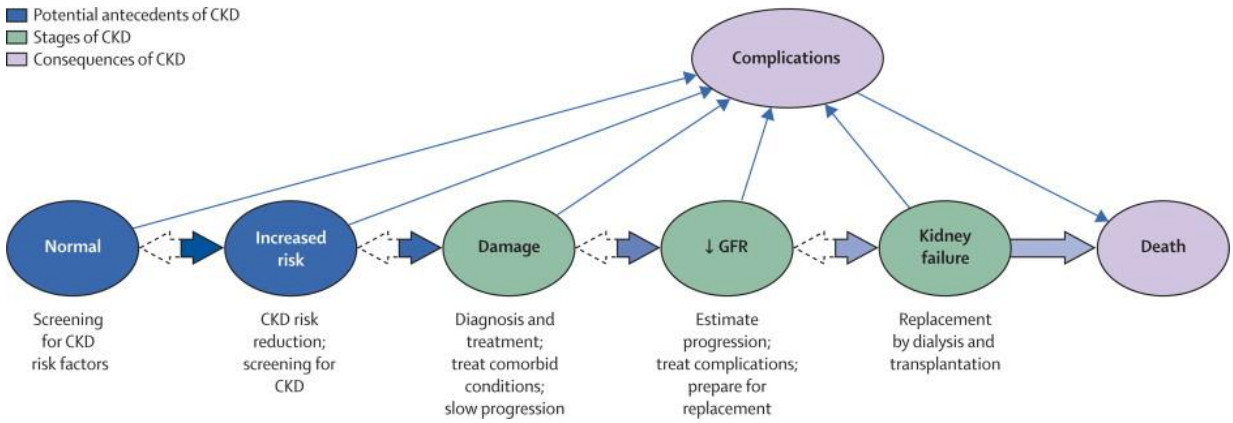

Figure 6.1: Progression of chronic kidney disease (CKD)[71]

6.2 Hemodialysis

Hemodialysis is the removal of waste products, fluids, and extra chemicals from the body via the blood using an artificial kidney or hemodialyzer.[83, 84] A minor surgery to the arm or leg to gain access to the blood stream is common, and a graft or a fistula is used to access the vascular system in the patient.[85] Blood passes through the hemodialyzer, which consists of a series of membranes that filter the waste products into the dialysate. The membranes are selectively permeable and allow the blood to pass through, cleaning it, and subsequently return to the body. [83, 84] Globally over 4 million people receive dialysis on a chronic basis.[86] Multiple studies have shown that extended treatment times lead to improved survival among ESRD patients.[84, 87-91] In-center treatment times are generally high (> 4 hours) and require patients to visit treatments clinics about 3-4 times a week for removal of metabolic wastes by running 120 L of dialysis fluid each session.[88, 92] Currently over 2 million patients receive dialysis to sustain life, and this number is described as less than 10% of the actual need[86]

While conventional dialysis is the current solution, intermittent dialysis results in abrupt changes to biofluid balance within the body, contributing to intradialytic hypotensive events and myocardial stunning.[87, 93-97] Furthermore, treatment at clinical centers decreases the day-to-day quality of life in ESRD patients, as it interferes with their physical, and social activities and their mental health.[82, 98, 99] An alternate to traditional dialysis treatment is the use of wearable dialysis devices.

6.3 Wearable dialysis devices

Wearable dialysis devices are external devices that are mobile and provide continuous dialysis throughout the day. Wearable dialysis can increase treatment times and thus directly improve survival rates among patients.[100-103] Additionally, it reduces the cost of dialysis, and improves

the quality of life through eliminating visitation of treatment clinics and sedentary dialysis for 3-4 hours.[91, 104, 105] Apart from these benefits, wearable dialysis would reduce waste due to reuse of the dialysate, which is currently disposed.[106]

The challenge with these devices is the necessity to reuse/regenerate the dialysate for the removal of toxins, and the reduction of the large volumes of dialysate used in classical dialysis (120L per patient). Methods to achieve wearable dialysis systems have been studied for years but sorbent-based systems have low binding capacities.[107-109] To circumvent this, multikilogram-scale sorbent systems were required.[109-111]

An effective method for decomposing urea to CO2 and N2 through the photoelectrochemical oxidation via TiO_2 has been investigated for the processing of agricultural urine for electrical power generation.[112] While that study proved high performance, the efficiency was only 0.28% for all UV lamp emissions, which would not make it feasible for a mobile dialysis device. However, recent advances in the nanostructure of TiO_2 films have reached up to 40% efficient UV LEDs, and together with improvements in catalytic production of O_2 this has opened avenues for development of TiO_2 based dialysis systems.[113-116]

The decomposition of urea takes place over an exothermic photo-electrochemical reaction which is represented by the following reactions on the electrodes:

$$Anode: \quad CO(NH_2)_2 + 6OH^- \rightarrow CO_2 + N_2 + 5H_2O + 6e^-$$

$$Cathode: O_2 + 2H_2O + 4e^- \rightarrow 4OH^-$$

$$Net: \quad CO(NH_2)_2 + \left(\frac{3}{2}\right)O_2 \rightarrow CO_2 + N_2 + 2H_2O$$

where $CO(NH_2)_2$ represents the urea in the equations. The cathode reactions take place on the carbon cloth (Figure 6.2) with the anodic reactions taking place on the TiO_2 plate. Gases produced due to the reduction at the cathode are released from the air breathable carbon cloth and do not interact/interfere with the oxidation process.

6.4 Motivation for current research

A new technique consisting of photo-electrochemical decomposition of urea developed by the Center of Dialysis Innovation at the University of Washington has the potential to improve the quality of life for ESRD dialysis patients.[117-119] The key objective is to produce a wearable dialysis system (POUR dialysis unit), utilizing a closed dialysate loop, that can extend dialysis periods and allow normal day to day functioning of patients. While the technology is currently being investigated from the electro-chemical perspective and is making significant improvements, an optimized flow design is needed to enhance the transport rates of urea, from the bulk dialysate to the catalyst TiO_2 surface, to make the system more compact, portable and energy efficient.

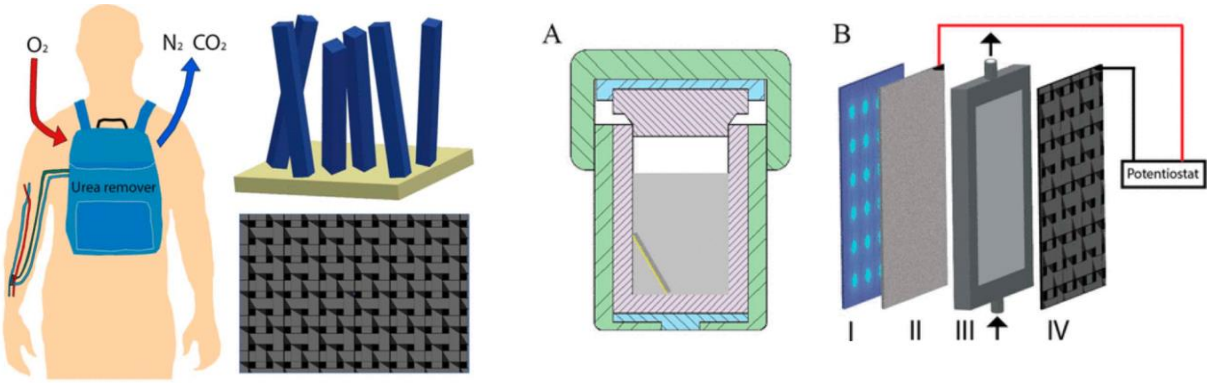

(i) *(ii)*

Figure 6.2: Schematic showing the process of blood retrieval for a proposed wearable dialysis machine (i) along with schematics of the nano TiO_2 fibers. A sectional view of the dialysis system in (ii) shows (A) FTO Substrate, With Conductive Surface Facing down, Inside the Hydrothermal Vessel during TiO2 Nanowire Synthesis and (B) Schematics of Device Setup: (I) 365 nm LED Array; (II)

TiO2/FTO Substrate; (III) 3 mm Thick Spacer through Which the Dialysate Simulant (10 mM Urea in 0.15 M NaCl) Flows; (IV) Air-Breathable Platinum-Coated Carbon Cloth.[117]

This thesis studies various aspects of the dialysate fluid system and photo-catalyst oxidation channel design via CFD. A streamlined manifold design can remove stagnation regions, avoid pressure losses, and create a more efficient flow loop. Channel shape and size have a considerable influence on the decomposition of urea as the transport of the urea requires effective mixing to overcome the diffusion limit. A detailed CFD study can identify and isolate the predominant factors and improve the design to obtain the best overall mixing and transport of urea, making the TiO_2 photo-electrochemical system viable as a portable dialysate regeneration solution in a wearable dialysis machine.

6.5 Study outline

The aim of this work is to understand the fluid dynamics of urea transport and removal from a wearable dialysis channel prototype. In chapter 7, this thesis describes the detailed development of the urea oxidation geometry, setup of the numerical model, and the different performance metrics used to evaluate each individual channel design. In chapter 8, the numerical model is described. This involves a rigorous grid independence study to demonstrate that the numerical simulations are able to accurately describe the small scales necessary to resolve the gradients of concentration that determine the mixing and, ultimately, the flux of urea to the catalyst wall. This is followed by determining the right diffusion coefficient of urea from literature and experimental values and evaluating different urea oxidation reaction models to represent the physics of the photo-catalytic reaction. The model is then adjusted with experimental data for different inlet concentrations of the dialysate. In chapter 8, three variations of channel designs are explored: thin

channel, wavy channel, and chevron channel. For each design, a parametric analysis is conducted to determine the best geometric and flow conditions that provide maximum removal of urea. These designs are then compared to each other to provide recommendations for the development of experimental prototypes. Additionally, the current panel (channel arrangement) is evaluated for fluid inefficiencies, providing design suggestions to improve the overall performance of the wearable dialysis system. The evolutionary design of the POUR channel is discussed in detailin Chapter 9. Finally, the limitations of this study and future work are explained in chapter 10.

Chapter 7

METHODOLOGY

The aim of this study is to understand fluid mechanics of the diffusion and convection of urea as dialysate passes through the oxidizing channels. A parameter of interest is the concentration of urea at the outlet or daily removal rate of urea. The target daily removal rate of urea is 15 g/day, with the engineering goal of meeting this requirement. Increasing the daily removal rate is favorable as it increases the range of patients who can use the device, reduce the cost of the device, or reduce the time spent in dialysis for the patient. Overall, the study focuses on using CFD to optimize and enhance the fluid dynamics of urea removal to develop a novel wearable dialysis system. While the overall CFD setup is explained below, the modelling developed to understand the performance of the POUR channels is discussed in the next chapter, including available experimental data. The model developed from the initial analysis is used to design and optimize the POUR channels.

7.1 POUR CAD geometry

The POUR channels for each specific design and flow manifolds were developed using the CAD modeler Solidworks (Dassault Systemes, Velizy-Villacoublay, France). Different iterations of length, width, and height were studied to analyze the independent influence of each geometric parameter. The inlet and outlet flow manifolds were modeled as either inline or perpendicular to the channel, while the overall channel array alignment was modified to find an optimized setup for urea removal from the dialysate. Once the basic CFD model was developed, design optimization was performed, where the results from the CFD were used to change the Solidworks model. This was done for the four main designs: Baseline channel, Thin channels, Wave channels, and Chevron channels. For each design, a parametric study was conducted using feedback from the simulations to alter the design. The baseline channel was sized at 22.1 cm x 2.86 cm x 0.3 cm.

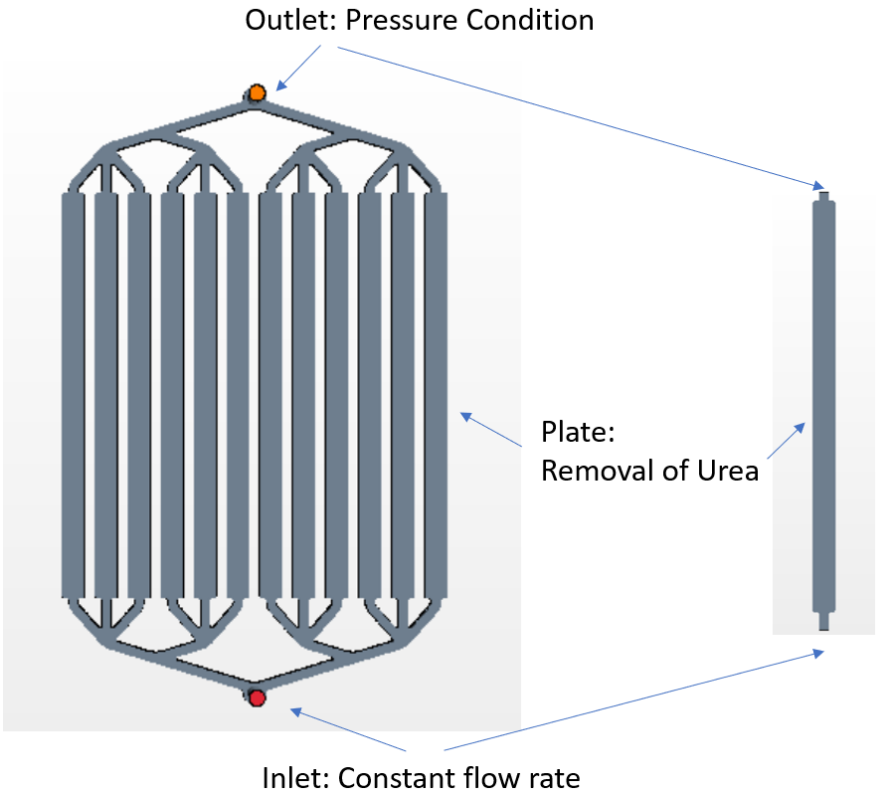

Figure 7.1: The POUR panel (a) consists of twelve channels. The dialysate enters the panel at the bottom, rises through the channels reacting with the TiO2 resulting in removal of urea from the

dialysate and reduction in the urea concentration of the dialysate, and finally exiting from the top. The channels (b) are optimized in this study to find an effective shape and size to maximize urea decomposition.

7.2 Grid Convergence and Time Step

Initially, two different mesh sizes of 11M and 8M cells were used, corresponding to base element sizes of 0.5 mm and 0.25 mm. The larger coarser mesh was used to investigate a bird's eye view of the POUR system involving the inlet/outlet flow manifolds as well as the arrangement of the individual channels. This provides a robust understanding of the flow parameters required to design the overall system. The finer mesh is used to resolve the mass boundary layer above the TiO_2 plate which decomposes urea from the dialysate. The flow patterns at these small scales help drive the design of the individual channels to improve the effectiveness of urea removal from the dialysis system. However, accurate modelling of the diffusion of urea required an highly resolved mesh, and a mesh independence study was conducted resulting in the baseline mesh utilized for the parametric design study. The simulations were run under steady state condition.

7.3 Boundary conditions

In the POUR channels, the dialysate enters the domain through an inlet velocity condition and exits the fluid domain through a constant pressure outlet boundary. All other boundaries are modeled as no slip walls. The inlet has constant uniform concentration of 10 mM, which corresponds to a urea mass fraction of 0.0006 in water. The urea is removed by the TiO_2 plate at the bottom of the channels. The TiO_2 decomposes urea and removes it from the dialysate at a net rate of 15 g/day. This corresponds to a urea flux of 9.33×10^{-7} kg/m^2-s, which is specified as a constant outward flux boundary conditions. In simulations that incorporate the influence of the

concentration of urea on the reaction rate, the local element concentration is determined and used to calculate the local flux on the surface of the TiO_2 plate.

7.4 Parameters of interest in the CFD simulations

The engineering goal of this study is to maximize the removal of urea from the dialysate, minimizing cost. Cost can be categorized into two components: fluid cost and material cost. Hence, the main parameters we will discuss are:

Concentration of urea

The dialysate starts with an initial concentration of 10 mM. As the dialysate flows through the POUR channels, urea is removed prescribed by a flux at the bottom of the channel. This reduces the concentration of urea in the flow. Due to the extremely low concentration of urea in the dialysate, urea is modelled as a passive scalar and the concentration of the passive scalar can be calculated for any defined region. For our simulations, we look at different planes to understand the fluid and diffusion mechanics and calculate the average concentration of urea at the outlet.

Pressure Drop

To drive the flow through narrow channels and multiple parallel panels (each consisting of individual channels), an external pump is required. Hence, as design modifications are made, a close eye is kept on the resulting pressure drop to maintain our energy/fluid costs within reasonable range. High pressure drop through the channel translates into expensive and/or larger/bulkier pumps, which reduce the efficiency of the wearable dialysis device.

Area of TiO_2

The main production cost of building a wearable dialysis device is expensive TiO_2, which oxidizes the urea. Apart from this, fabrication of certain design may require specialized manufacturing processes increasing the overall production cost of the channel. These costs are important to keep in mind during the design and development of the POUR channels. Hence, design considerations would tend to reduce the area of TiO_2, with unique design comparisons normalized by area of TiO_2 to provide a true picture of their individual performance.

Chapter 8

NUMERICAL MODEL DEVELOPMENT

With the goal of developing a POUR channel capable of removing urea at a rate of 15 g/day, the challenge lies in increasing the mixing of urea at such low Reynolds number flows. These laminar flows do not produce any instabilities in the flow, which can help mixing and removal of urea. Before the design of the channel can take place, the numerical model is developed to match what is observed experimentally. Two teams from the Hinds Lab focused on evaluating the feasibility of TiO_2 in removing urea using a 3 mm channel with a base design of 22 cm x 2.86 cm cross section area. Experimental data from the two individual teams was used to develop the numerical model. In this chapter, we explain the stages of the development of the numerical model and, in the following chapter, the model development is discussed with its implication on the design of the channels.

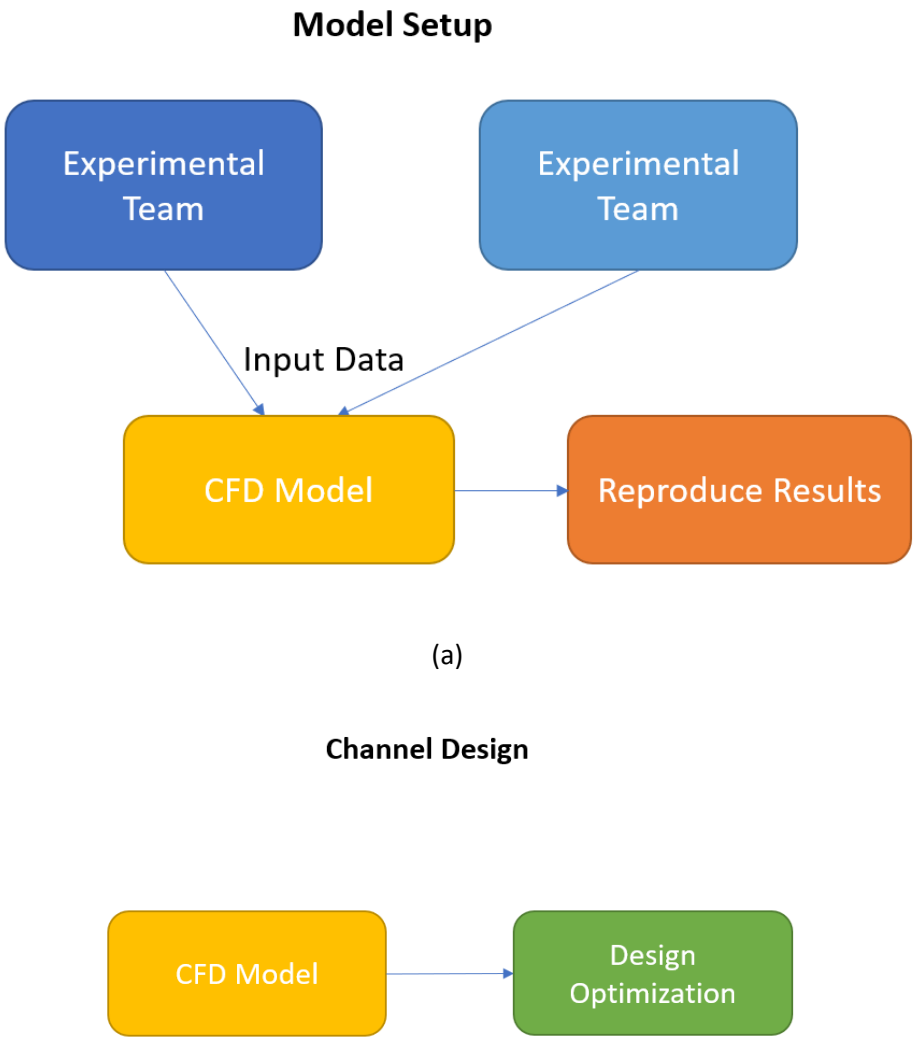

Figure 8.1: Numerical model development flow chart. (a)Data obtained from individual experimental teams help build the CFD model through an iterative process. The finally CFD model was used to reproduce results observed by the experimental team. Once the model was developed (b) a parametric study was conducted to optimize the channel design.

8.1 Mesh development

The initial element size was 0.25 mm. This spatial discretization included inlet/outlet piping and the inlet/outlet manifolds. With a large volume of 222 mm x 23 mm x 3 mm to mesh, an unstructured mesh consisting primarily of tetrahedral elements, lined with prismatic elements on the top and bottom walls, was used. The total grid node count was 8 million. While initial results provided by the mesh showed promise, a more refined mesh was developed to resolve the diffusion of urea , which depends on resolving the small scale gradients in concentration. To account for the high-density mesh, the auxiliary components of the dialysis channels such as the piping and the manifold were removed. With the discretization of only the channel sections with TiO_2, the overall mesh sized increased to 13 million mesh cells. Since the primary reason for this refinement was resolving the diffusion of urea, only prismatic elements were used in the grid, which would capture the concentration of urea throughout the mass boundary layer. Under the same flow conditions, the initial growth of the mass boundary layer was identical for both meshes. However, after a channel length of 100 mm, significant differences were observed between the grids, with the coarser mesh reporting inaccurate concentrations of urea, as seen in Figure 8.2. This effect exacerbated as the channel length increased. At the outlet, the refined mesh reported a 12% increase in daily urea removal rate.

A grid independence study was conducted using the refine mesh cells, where the number of prismatic elements were incrementally increased from 50 to 200 cells. As seen in Figure 8.3 the subsequent mesh showed negligible improvements in results with increasing computational costs. To check if this solution was specific to the current problem, the smallest mesh (50 prismatic cells) and the largest mesh (200 prismatic cells) were re-evaluated for a pseudo low diffusion coefficient

problem where the Peclet number increased from 3000 to 30,000 (the importance of Peclet number in this model is discussed in the subsequent section).

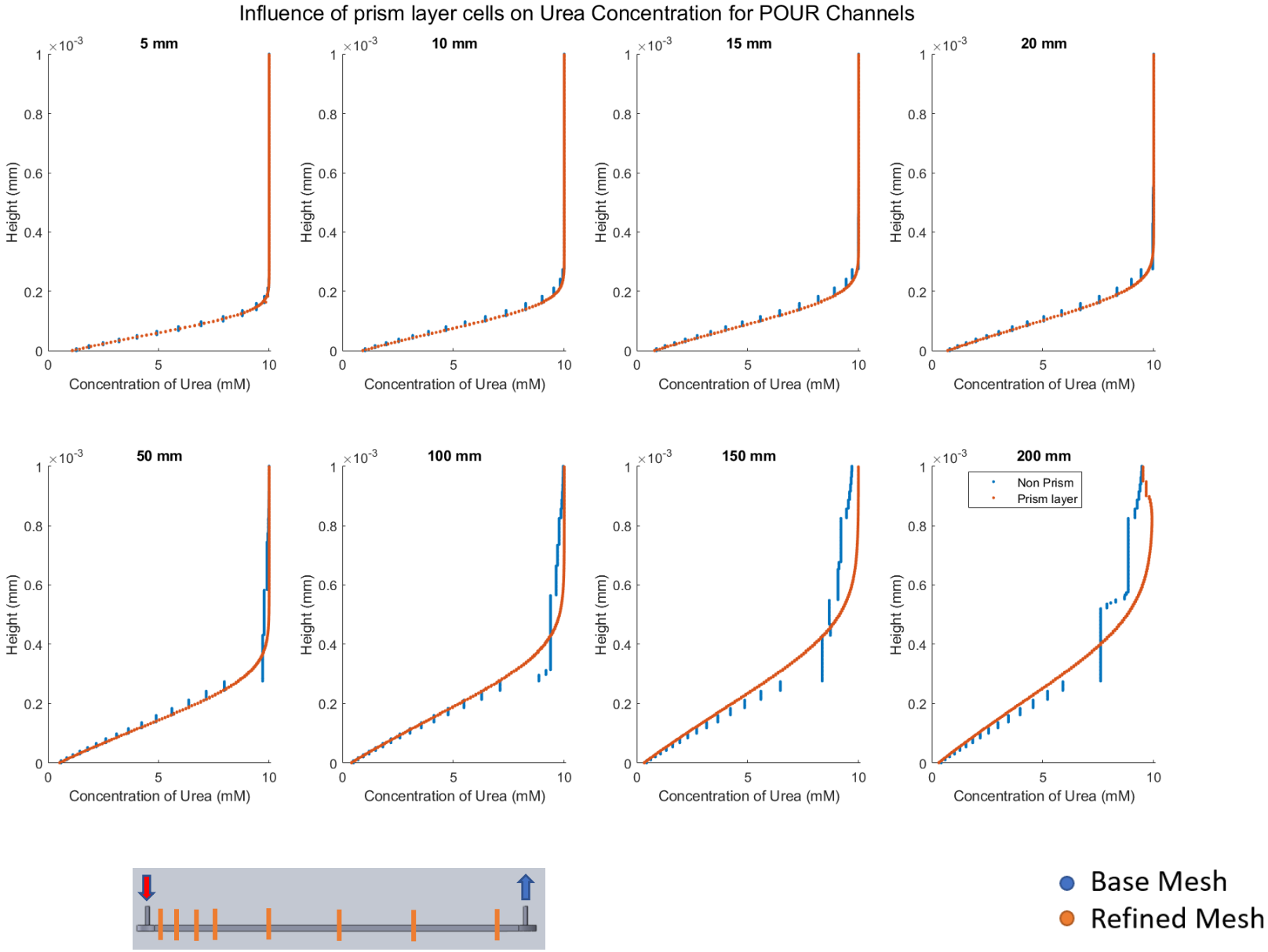

Figure 8.2: The refined mesh with 13 million prismatic cells reported significantly different concentration values for urea after a channel length > 100 mm. Consequently, the refined mesh reported an 12% increase in daily removal rate of urea.

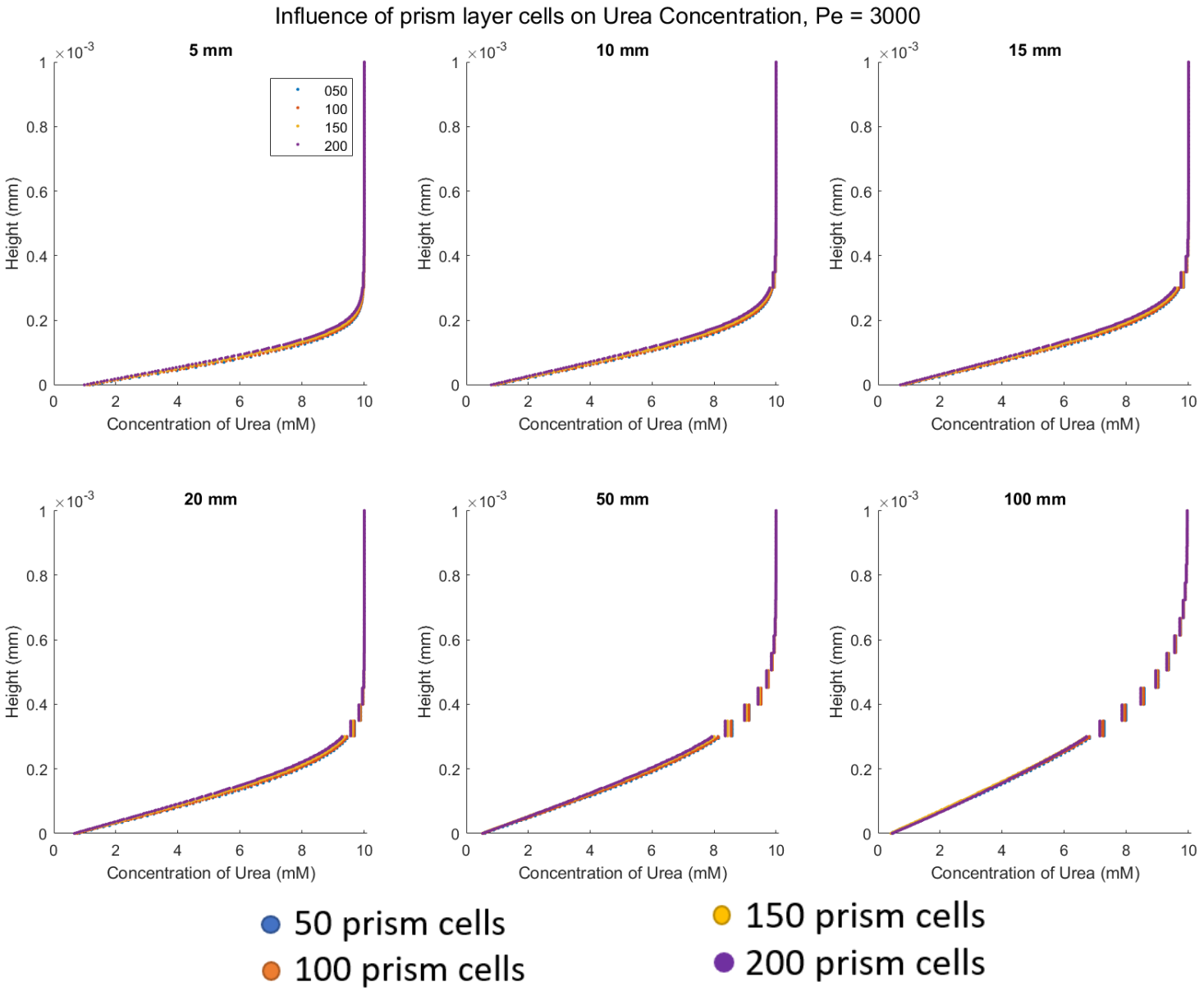

Figure 8.3: A grid independent study shows negligible change in concentration of urea across the height of the channel for different channels for Pe = 3000.

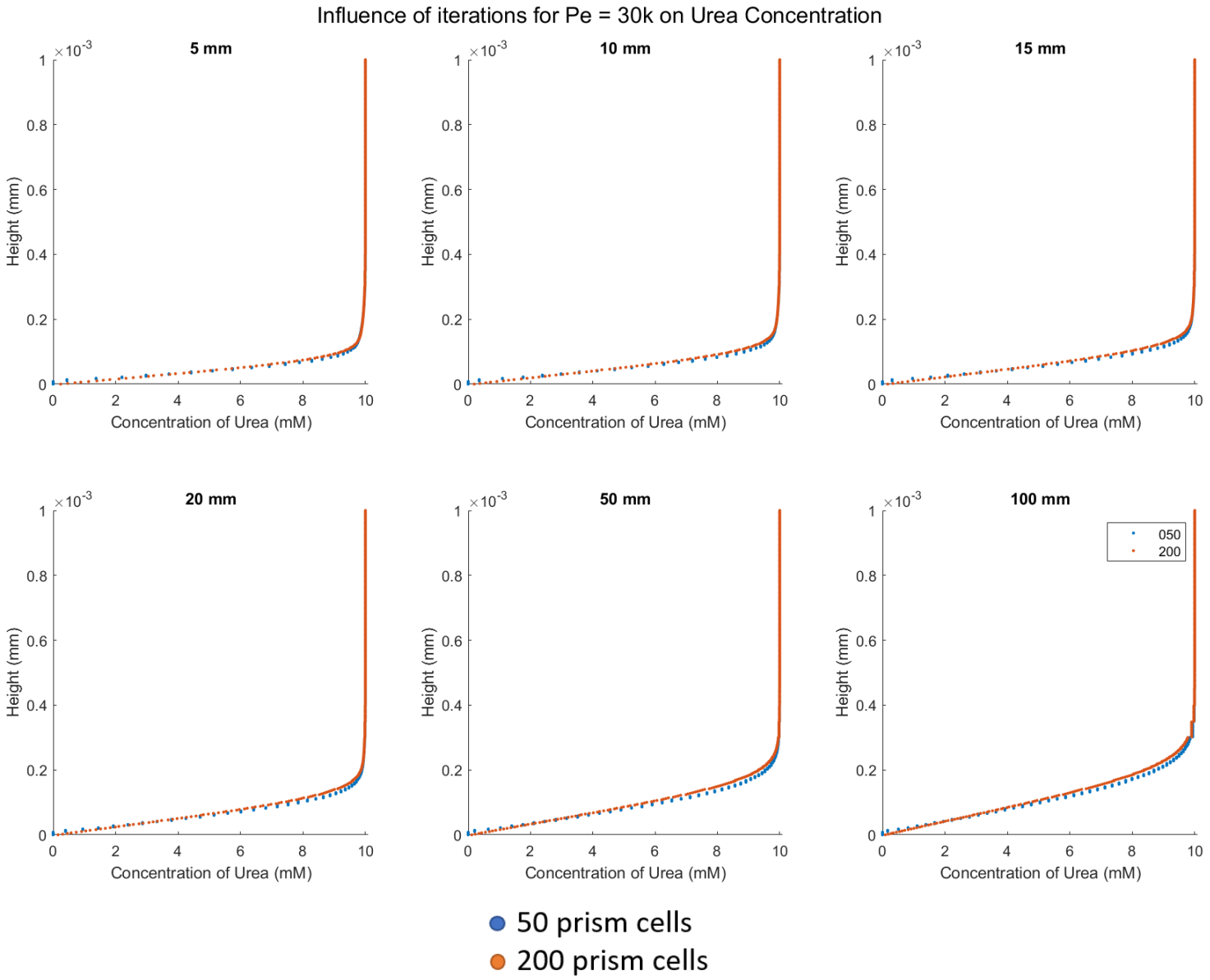

Figure 8.4: A grid independent study between the coarse mesh (50 prism cell) and the fine mesh (200 prism cell) shows negligible change in concentration of urea across the height of the channel for different channels for Pe = 30,000. This suggests that the coarse mesh sufficiently resolves the diffusion of urea.

The concentration of urea through the channel for both grids for this extremely low diffusion problem showed no significant different. This suggested the coarser mesh of 50 prismatic cells resolved the diffusion of urea sufficiently. Therefore, this mesh was selected for subsequent studies.

8.2 Diffusion coefficient of urea

With low Re flows in the axial direction (along the length of the channel) and no fluid flow in the transverse direction, the mode of urea transport is limited to diffusion. Hence, there is fundamental need to model the diffusion coefficient of urea accurately. The diffusion of urea determines the nature of the flow as captured by the Schmidt number. The Schmidt number is a purely intrinsic property of the material that describes the ratio of viscous momentum transport to diffusive transport of a particular substance (Note: The diffusion coefficient is a property dependent on the diffusing agent and the diffusion medium). The Schmidt number is defined as:

$$Sc = \frac{\nu}{D} = \frac{\mu}{\rho D}$$

$$Sc = \frac{viscous\ diffusion\ rate}{molecular\ (mass)\ diffusion\ rate}$$

where *Sc* is the Schmidt Number, ν is the kinematic viscosity, *D* is the mass diffusivity, μ is the dynamic viscosity of the fluid, and ρ is the density of the fluid.

While the Schmidt number explains the diffusion of a species within the fluid, the nature of the flow is not well characterized by the Schmidt number. The product of the Schmidt number and the Reynolds number results in the Peclet number. The Peclet number incorporates the convection of the fluid, from the Reynolds number, and the diffusion transport from the Schmidt number. This

provides a clearer view of whether the flow is convection-dominated (high Peclet number) or diffusion-dominated (low Peclet number). The Peclet number is defined as:

$$Pe = \frac{Lu}{D} = Re_L * Sc$$

$$Sc = \frac{advective\ transport\ rate}{molecular\ (mass)\ diffusion\ rate}$$

where *Sc* is the Schmidt Number, *u* is the local flow velocity, *D* is the mass diffusivity, *L* is the characteristic length, and Re_L is the Reynolds number of the flow.

For our study, diffusion coefficients were provided by two individual experimental teams, while additional values were found in the literature. For the concentration of urea, previously published literature suggested a variable diffusion coefficient. We modelled three different cases where the diffusion coefficient was 1.0×10^{-10} m^2/sec, 1.4×10^{-9} m^2/sec, and variable diffusion coefficient dependent on the local concentration that followed the experimental data and the linear fit. For the variable diffusion coefficient, the simulation recalculates the diffusion coefficient through all 13 million cells for each iteration, thus increasing the computational cost significantly. All three models showed substantially different results, as seen in Figure 8.5. The urea removal rates were 0.07 g/day, 0.29 g/day, and 0.26 g/day, respectively. Since the variable diffusion coefficient model captures the diffusion of urea more accurately as the concertation of the urea decreases, this model was selected for future investigation of channel design.

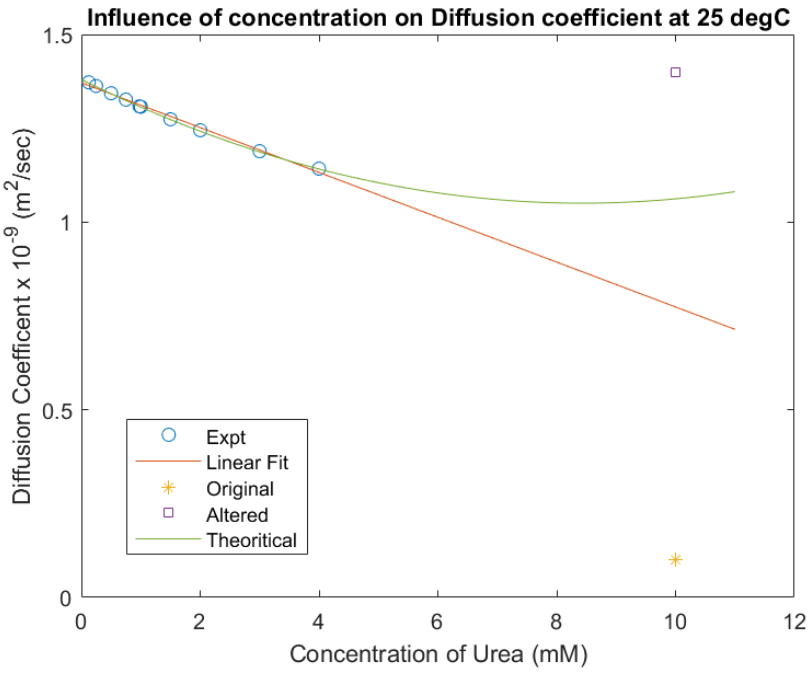
Influence of concentration on Diffusion coefficient at 25 degC
Diffusion Coefficent x 10^-9 (m^2/sec)
Concentration of Urea (mM)
Expt
Linear Fit
Original
Altered
Theoritical
0
0.5
1
1.5
0
2
4
6
8
10
12

(a)

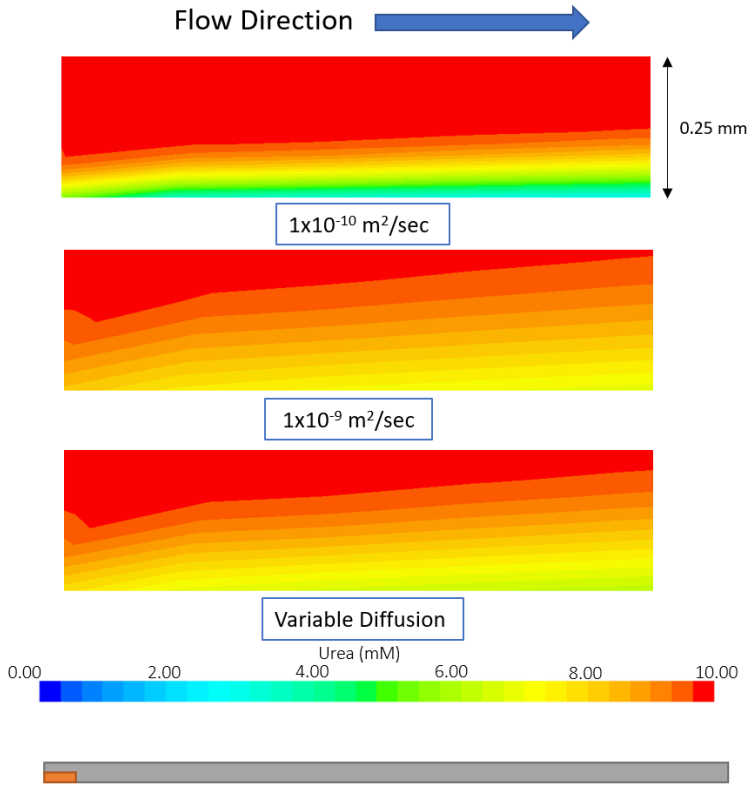
Flow Direction
0.25 mm
1x10^-10 m²/sec
1x10^-9 m²/sec
Variable Diffusion
Urea (mM)
0.00
2.00
4.00
6.00
8.00
10.00

(b)

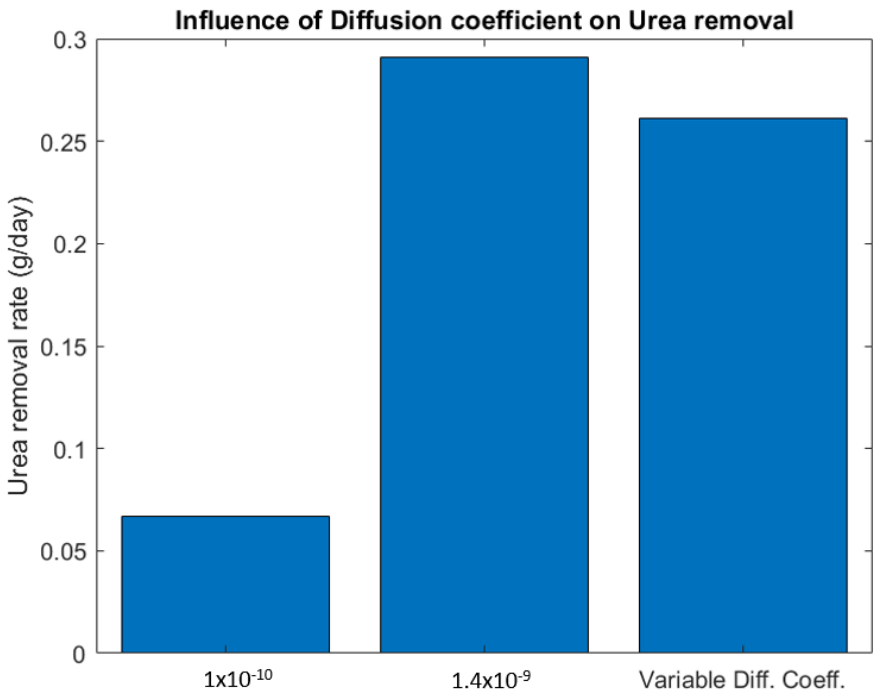

(c)

Figure 8.5: Influence of diffusion of urea on the model results. The diffusion coefficient of urea was modelled from values obtained by two experimental teams (labeled as Team 1 & Team 2) and from literature (a). Literature suggested variability of the diffusion coefficient, primarily influenced by the concentration. The three values for the diffusion reported different results as seen in the longitudinal section view of the first couple mm of the channel (b), where the urea concentration is dramatically different and the subsequent daily urea removal rates are different (c). The variable diffusion coefficient model is selected for future investigation, despite the increase in computational cost.

8.3 Determination of urea removal rate

The first goal of the POUR device was to remove urea at a constant rate of 15 g/day. The two experimental teams reported multiple successful trials at meeting this target with a flow rate of 1.8 ml/min over 32 channels. Thus, the first main benchmark for our model was reproducing this

result. An initial constant removal rate model was selected for the POUR channel inspired by the overall targeted 15 g/day removal rate. This reverse engineered model resulted in high removal of urea even at the end of channel where the concentration of urea had dropped to zero. In such a case, the removal rate is influenced simply by the lower diffusion rates of urea as this is influenced by the low concentration at the end of channel. However, the theoretical removal rate cannot remain constant. The photo-electrochemical oxidation 'reaction' of urea at the TiO_2 follows a first order reaction relationship with the concentration, which can be used in the numerical model to improve the fidelity. Substantial difference was reported between the two models, as shown in Figure 8.6 where the constant reaction model severely overestimated the performance of the channel.

As the dialysate flows through the channel, high concentration urea is first exposed to the TiO_2 plate and there is rapid oxidation of urea, which results in lower concentration of urea at the surface of the TiO_2 plate. This concentration difference promotes the diffusion of urea from high concentration dialysate above to the lower concentration dialysate below, based on the magnitude of the concentration difference and the diffusion rate of urea of in the dialysate. However, as the removal rate exceeds the slow diffusion rate, the concentration of urea on the TiO_2 plate continues to decrease, which results in reduced removal of urea as the reaction of urea follows a first order reaction rate. Hence, the first order reaction rate is a better model for the simulation of dialysate photo-catalytic oxidation.

The first order model is then compared with results from the first experimental team's trials. Since the model used an idealized first order reaction rate, the rate halves at half the urea concentration and goes to zero when the urea concentration reduces to zero. For an accurate representation of the reaction, the coefficient of proportionality or linearity required determination. Data from the

experimental team is used to calculate the coefficient of linearity via multiple iterative simulations, which suggested a proportionality constant that can match the experimental results.

The accuracy of the subsequent model was evaluated against data from the second experimental team, which conducted concentration tests for different initial concentration of urea at a flow of 1 ml/min. The numerical model accurately predicted the performance of the POUR channel at 10 mM, which is the target initial concentration of the device. For concentrations < 10 mM, the model underpredicted the removal rate, which is acceptable as any future design changes would result in higher (and more favorable) removal rate in practical applications. At concentration > 10 mM, the simulations overpredicted the removal rate, which requires correction. This is because at these concentrations, the physics of urea oxidation are different. We hypothesized that the concentration of urea saturates the reaction, and the reaction is limited by availability of TiO_2 molecules. However, in the current design of the dialysis system, high initial concentrations are unnecessary and therefore the model remains unchanged and the high concentration results are ignored.

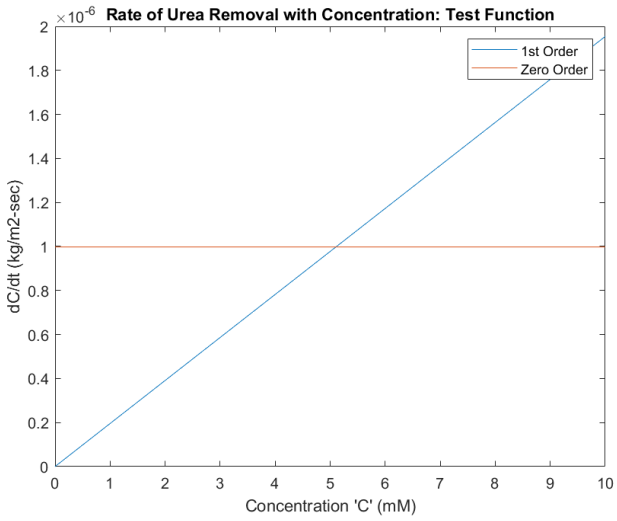
Rate of Urea Removal with Concentration: Test Function
×10^-6
1st Order
Zero Order
dC/dt (kg/m2-sec)
Concentration 'C' (mM)

(a)

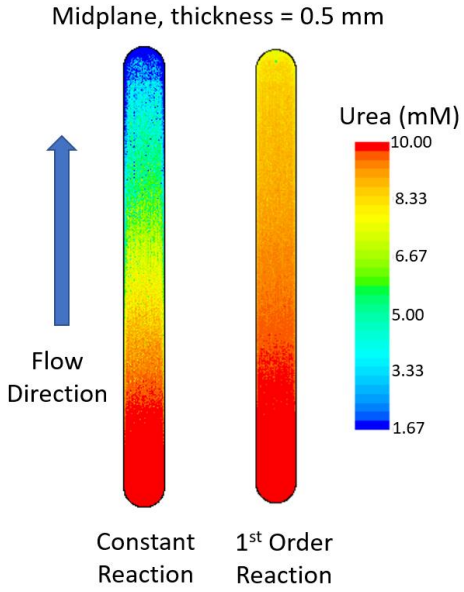
Midplane, thickness = 0.5 mm
Urea (mM)
10.00
8.33
6.67
5.00
3.33
1.67
Flow Direction
Constant Reaction
1st Order Reaction

(b)

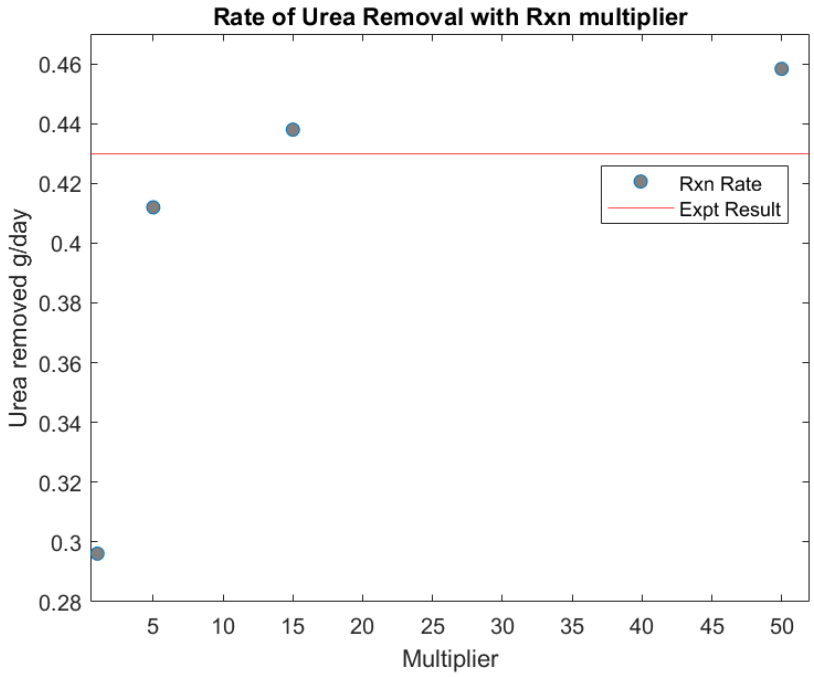
Rate of Urea Removal with Rxn multiplier
Rxn Rate
Expt Result
Urea removed g/day
Multiplier

(c)

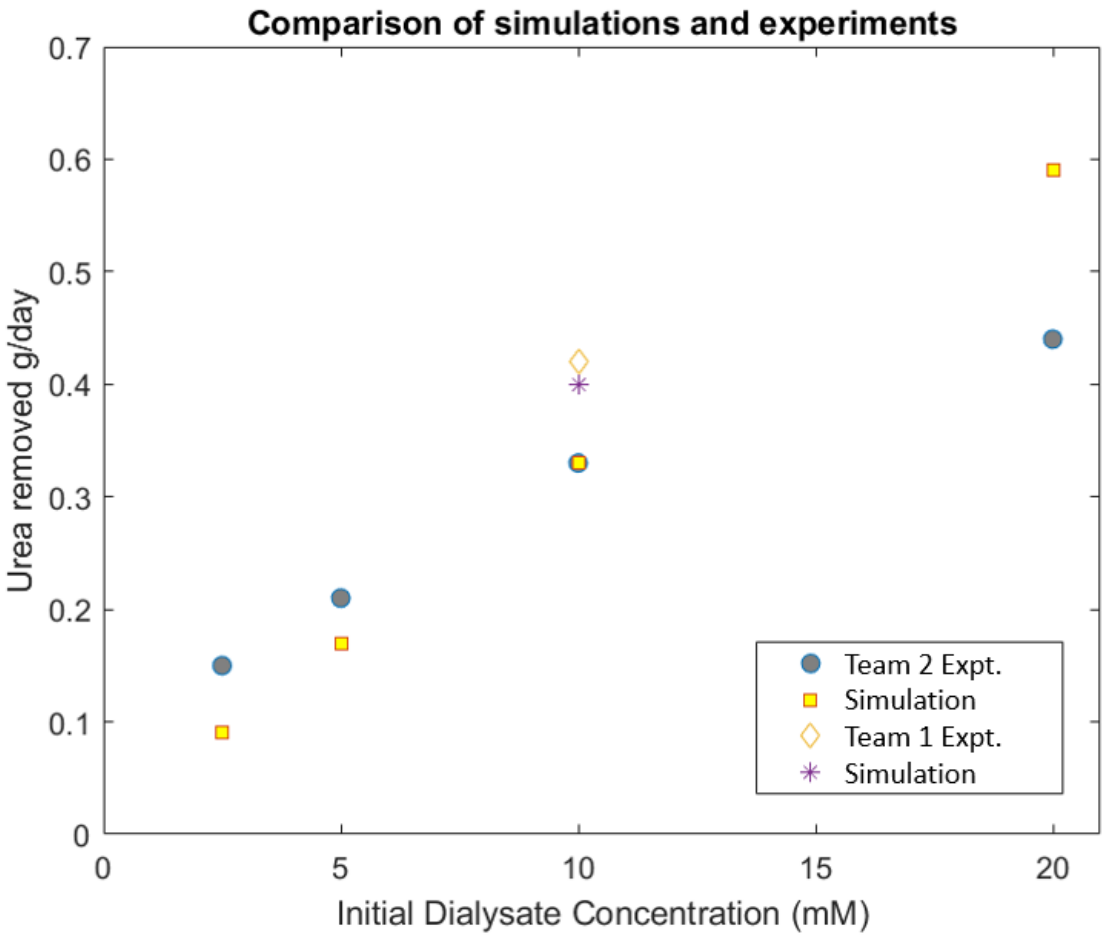

(c)

Figure 8.6: Influence of urea removal rate. (a) A constant urea removal rate was initially applied which overestimated the performance of the POUR channel and was subsequently replaced with an idealized first order urea removal rate. (b) Midplane views of the POUR channel show significant differences in the urea removal from the two different models. (c) The first order reaction model was tweaked to determine the coefficient of linearity which reproduced the experimental results. (d) The new model accurately reproduced urea removal rate for 1 ml/min experiments run by a different team. Additionally, the model underestimated the urea removal rate for lower initial dialysate concentration and overestimated the rate for high initial dialysate concentration. Since the lower concentration of

urea is of importance, the coefficient of linearity was further improved to close this difference, while the higher concentrations (>10 mM) inaccuracy was ignored due to the scope of the dialysis system.

Chapter 9

PARAMETERIC DESIGN OPTIMIZATION

With a sufficiently accurate numerical model, the different designs of the POUR channels and panel were investigated to evaluate their individual performance. For the panel design, the goal was to identify regions of inefficiency and optimize the fluid flow to enhance overall transport and removal of urea. This macrolevel optimization aimed at improvement channel arrangement and inlet/outlet manifolds to streamline the fluid flow across all regions. The results below discuss the first part of the study where regions of inefficiency were identified. Future work involves proposing design ideas that avoid fluid inefficiency and improve overall performance of the device.

The bulk of the discussion below pertains to optimizing the channel design with the goal of maximizing urea removal at low Reynolds number flows or laminar flow. This involves a comprehensive parametric analysis of different geometries of channels, while three main geometries are focused on in this thesis: thin channel, wave channel and chevron channels. In this

chapter the results from the parametric analysis are presented followed by an explanation of the various design considerations along with the development of the model in the discussion.

9.1 Panel optimization

The optimization process started with a basic twelve channel panel with urea rich concentration of 10 mM entering the channels from the bottom and exiting via the outlet at the top. The dialysate passes over TiO_2 plates on the bottom of each of the twelve channels, which decompose urea, reducing the concentration, allowing the dialysate to return to a mass exchanger (outside the system) for replenishment and thus forming a closed loop.

The target urea removal rate of the entire pour unit is 15 g/day. To achieve this, experimental studies (performed by collaborators) showed that eight such panels (12 channels in each panel) are required. The total area of twelve channels in each panel is 224 cm2, which gives us an average urea flux from the TiO_2 plate to be 9.77 x 10-7 kg/m2-s. The tested flow rates were 100, 150, 250 mL/min & 56 mL/min.

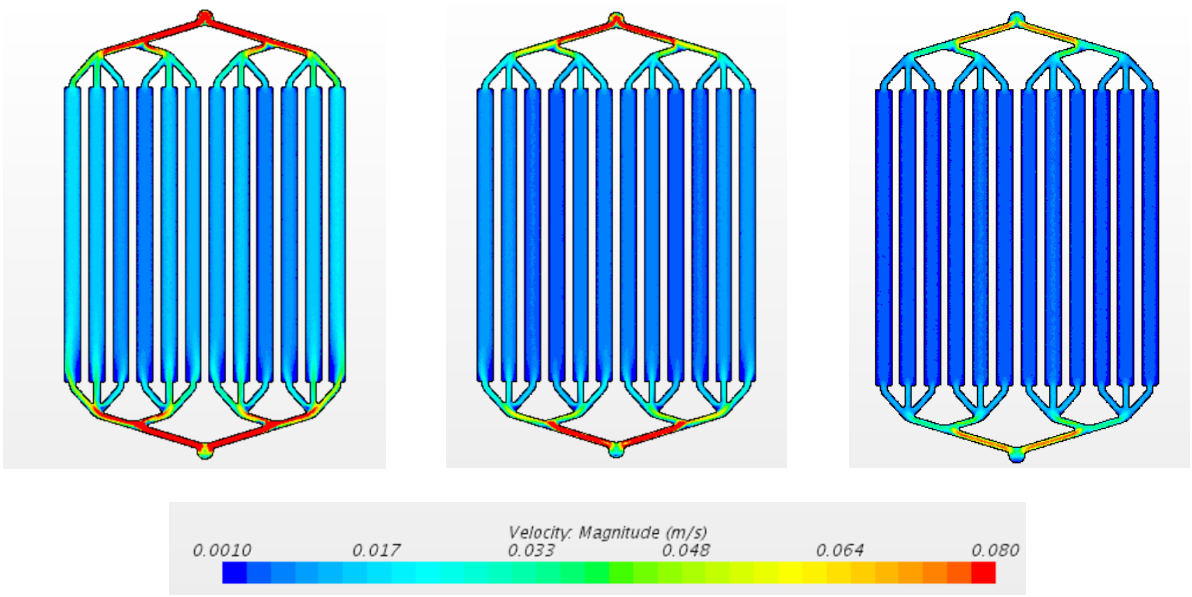

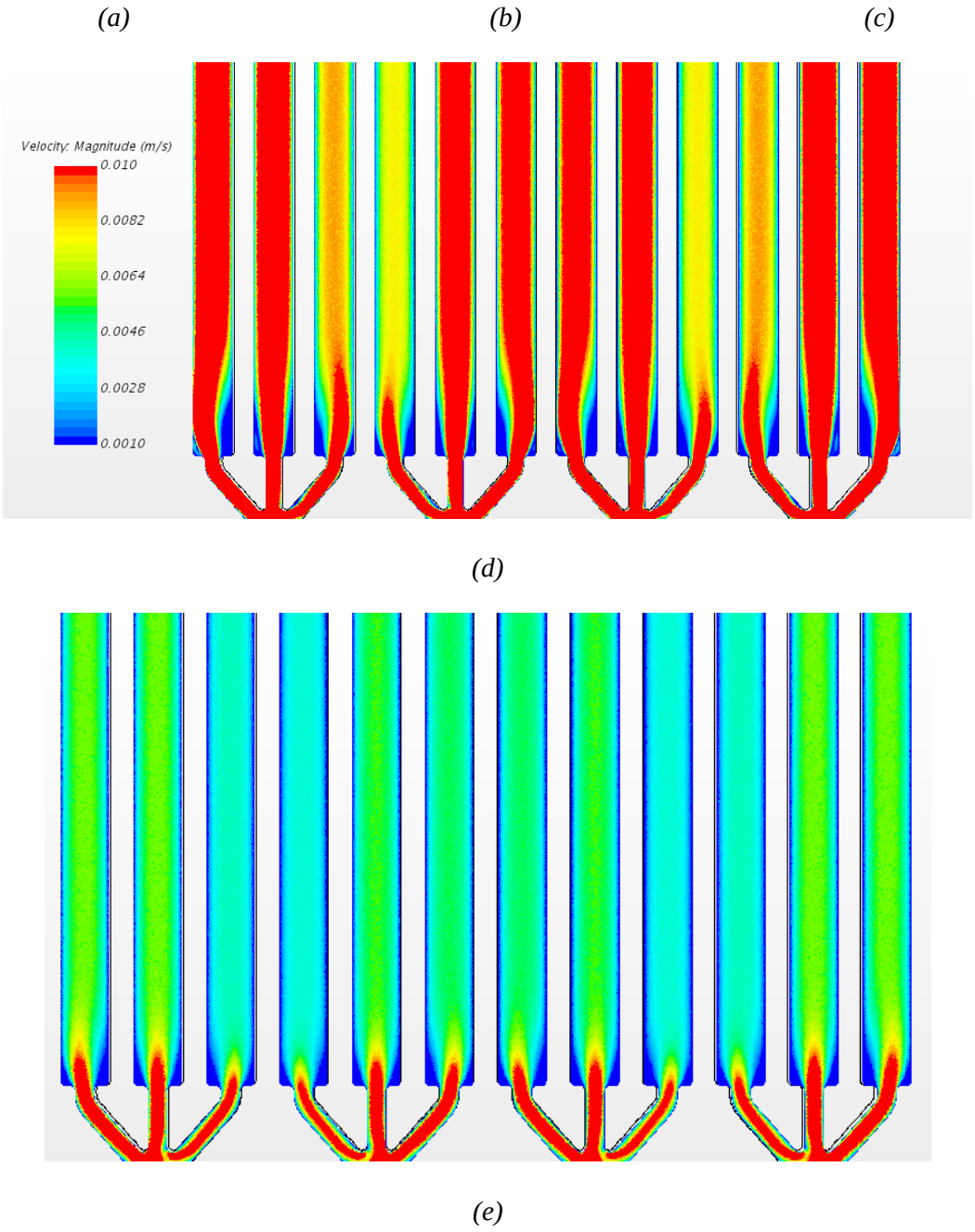

Figure 9.1. The splitting in the inlet manifold causes the dialysate to prefer some channels over others leading to different flow rates in different channels. As the flow rate reduces from (a) 250 mL/min, (b) 150 mL/min, and (c) 100 mL/min, the inter-channel variations reduce. The inlets are smaller than the channel sizes leading to expansion of the flow as seen in the case of (d) 250 mL/min, where the fluid jumps as it expands, resulting in inefficient urea transfer. These regions reduce again as the flow rate

decreases (e) 100 mL/min. The inlet/outlet manifold and channels need to be optimized to avoid such inefficiencies.

The velocity maps show that there is different peak and average velocities, inside the different channels. This is attributed to the inlet channels or manifold, which split the flow creating lower and higher flow resistances in different channels. This causes the flow to flow higher in some channels over the other. The channel variance in flow velocity, leads to non-uniform decomposition of urea between channels, resulting in ineffective utilization of the TiO_2 plate. As the flow rate is increased, the smaller inlet channels which open into the TiO_2 channels cause the flow to jump and separate. This further increases the area of TiO_2 plate that receives no fresh dialysate, resulting in reducing the efficiency of the system. Figure 9.1 also shows small stagnation regions around flow divergence caused at the inlet/outlet flow splits. By changing the inlet/outlet manifold and streamlining the design of flow channels, flow separation, stagnation regions, and non-uniform inter-channel velocities can be avoided.

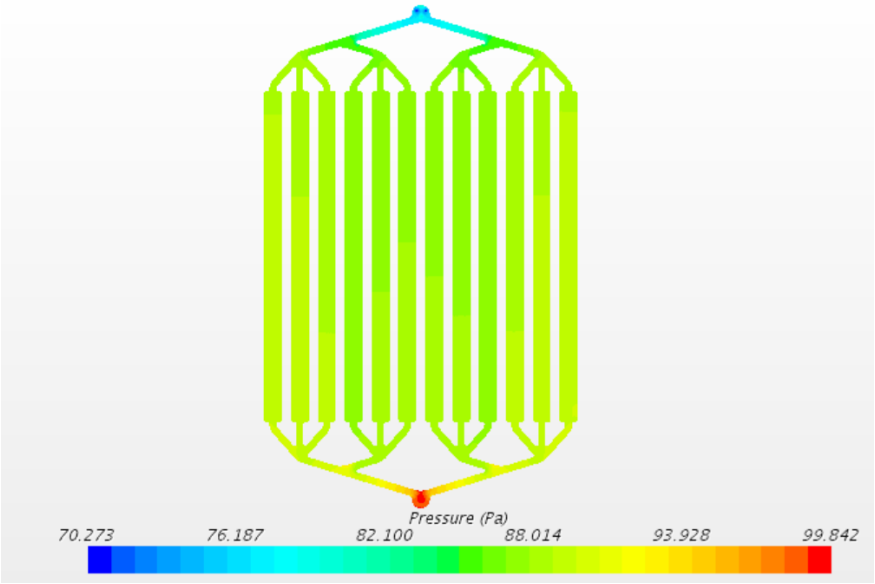

Figure 9.2: The pressure drop for 150 mL/min is about 30 Pa. This increases with increase flow rate.

The pressure drop across the entire panel is about 15 to 70 Pa (100-250 mL/min), which can be easily accommodated by a simple pump in the system. The pressure chart shows tiny low-pressure areas at the outlet of the panels, which causes oscillations in flow parameters and can be solved by extending the outlet. There is a non-linear relationship between the concentration of urea at the outlet with flow rate. The aim of the study is to maximize the removal rate of urea, which corresponds to the lower concentration of urea at the outlet. This encourages future studies to be at lower flow rates (higher residence times of urea in the reaction chamber).

9.2 Channel optimization - thin channels

Influence of flow rates and height of channel

The original experimental channel was at height/thickness of 3 mm. Since the diffusion scales are extremely small, the channel thickness was first decreased to 1 mm and 0.5 mm. The dialysate flow rate was varied at 5.00 mL/min, 3.10 mL/min and 0.54 mL/min. Additionally, the TiO_2 was placed at a 0.1 mm step. The urea removal flux (associated with the reaction rate of urea on the catalyst) included the first order reaction model as explained in the previous chapter.

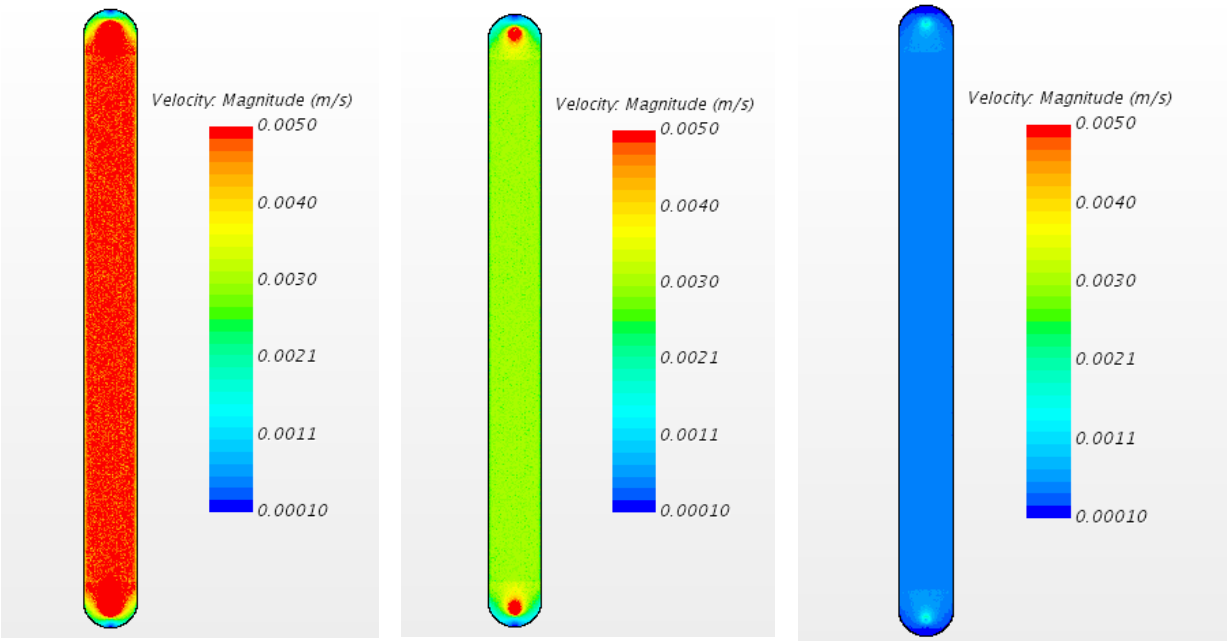

(a) *(b)* *(c)*

Figure 9.3: As the flow rates are reduced to (a) 5.00 mL/min, (b) 3.10 mL/min and (c) 0.54 mL/min a uniform flow profile exists in the channel. The channels have minimal stagnation regions which are away from the TiO2 plates, showing an effective shape and design for the channels.

The velocity maps show that there is a smooth uniform flow through the channels without any stagnation regions as it passes over the TiO_2 plate. The pressure drop across these channels is 47 Pa, 29 Pa, and 5 Pa for 5.0 mL/min, 3.10 mL/min, and 0.54 mL/min respectively for a thickness of 1 mm. At the midplane of the channels the urea concentration map shows effective removal of urea for a flow rate 0.54 mL/min, while the free stream concentration of 10 mM persists for the larger flow rates.

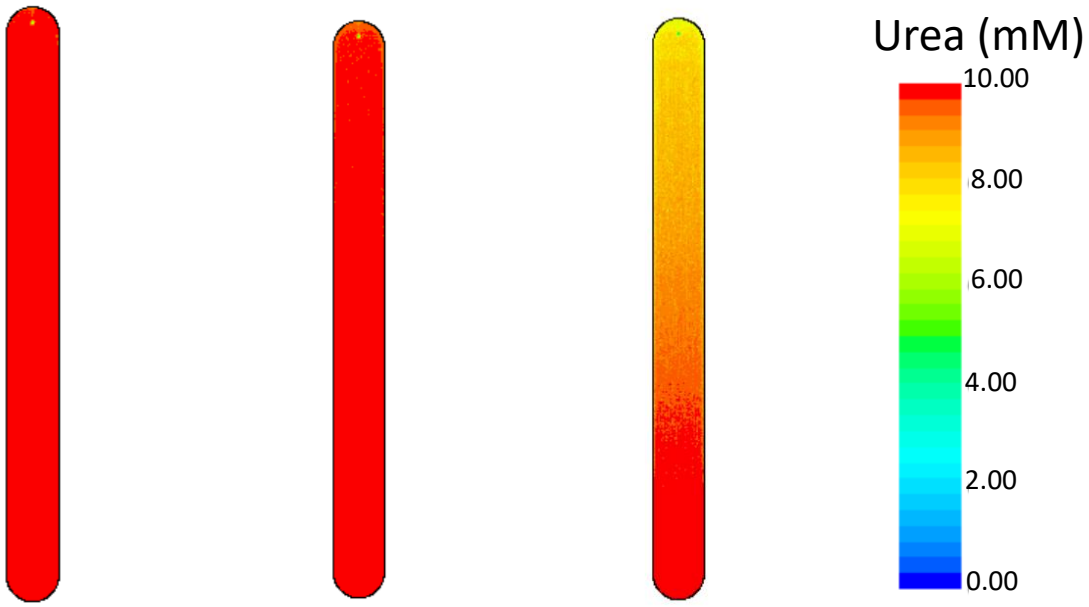

(a) *(b)* *(c)*

Figure 9.4: The mass fraction of urea at the mid plane (thickness/2) shows the free stream urea concentration (mass fraction of urea = 0.0006) persists at high flow rates (a) 5.0 mL/min and (b) 3.10 mL/min. In comparison, a nice decreasing concentration gradient of urea is seen at a flow rate of (c) 0.54 mL/min.

As expected, reducing the thickness of the plates from 1 mm to 0.5 mm brings the freestream urea rich dialysate closer to the oxidation plate Figure 9.5. Due to this, larger percentage of the urea begins to decompose, resulting in lower average outlet concentrations. As flow passes over the plate and decomposes, the lower concentration of urea results in a decreasing reaction rate. This means the reaction rate is fastest at the start and slows down towards the end of the channel. Diffusion of urea is the limiting factor at this point in the optimization process and, hence, the next steps involve the introduction of flow elements which can develop vortices that lead to mixing of

the urea from the bulk to the mass boundary layer near the catalyst plate, thereby utilizing the latter sections of the TiO_2 plate more efficiently.

(a)

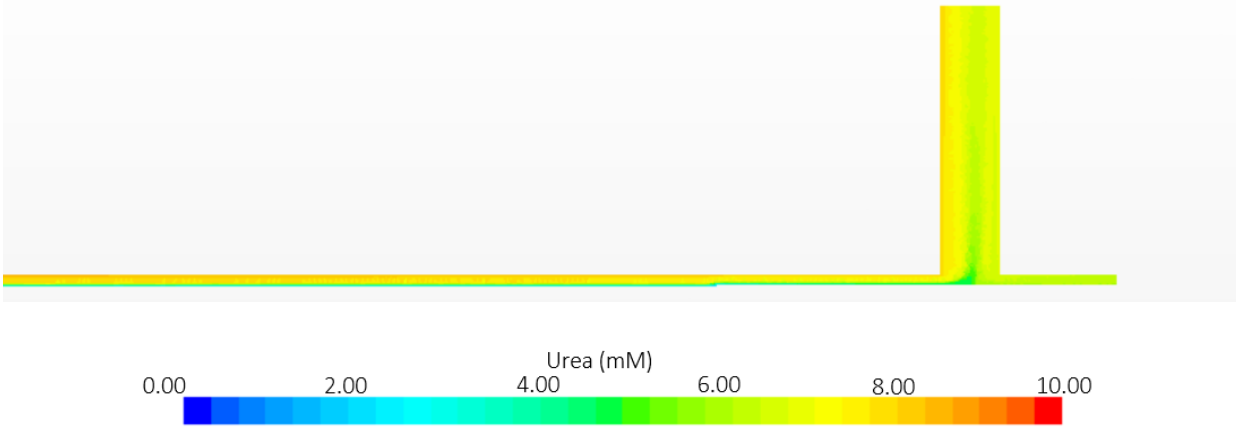

(b)

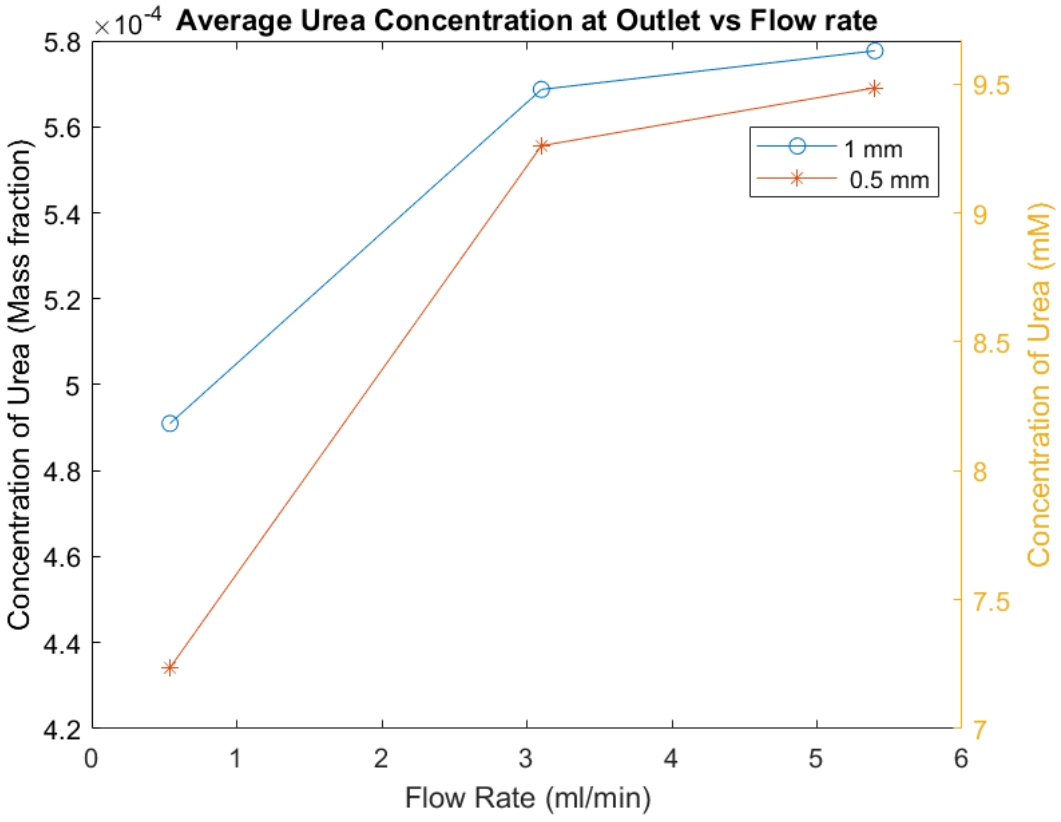

(c)

Figure 9.5. When the thickness of the panels is reduced from (a) 1 mm to (b) 0.5 mm, the free stream urea concentration (0.0006 mass fraction of urea) is brought closer to the TiO2 plate. This causes more reaction at the plate and a reduction in urea concentration through the flow. The effect is compounded when the flow rate reduces (less concentration with low flow and low thickness) and shows a similar trend as the 1 mm channel.

Influence of width and length

With the same aspect ratio, increasing the width of the channels showed negligible difference in urea outlet concentration as the change in velocities within the channel balances increase high concentration reaction of urea at the start of channel in addition with the reduced channel length. As the length of the channel is increased the performance increases due to increased available

TiO_2, however this increases the bulkiness of the POUR system which is counterproductive with our design goals.

9.3 Wave channel design

To improve mixing passively at these purely laminar flows and to enhance urea removal rate a new wave design was proposed. The base design included etching of waves on the bottom plate of the channel which is then coated with TiO_2. This improves the packing of TiO_2 due to the presence of the waves or folds like a corrugated surface for heat/mass transfer. The channel height was designed at 1 mm, a wave of amplitude 1 mm, and the baseline centered at height of 1 mm from the top plate (essentially matching where a plain TiO_2 plate would be). Only the bottom plate of the channel was corrugated as manufacturing corrugation on the carbon plate (top of the channel) is challenging.

Influence of the height of the channel

The simulations investigate the combined effect of the increased area of reactive material with mixing of dialysis produced by the repetitive acceleration and deceleration of the dialysate as it flows over the crests and troughs of the corrugated plate. The effect of the corrugated sheet for channel heights of 0.5 mm and 1 mm are compared with a plain channel of 0.5 mm height.

As the height of the channel is reduced, the bulk urea rich dialysate is brought closer to the reactive surface as explained earlier. However, in the case of the corrugated sheet, where the amplitude is also varied to match the reduction in channel thickness (if amplitude is kept constant, then channel height of 0.5 mm will match half the amplitude of 0.5 mm resulting in blocking of the channel), the area of TiO_2 decreases. Hence, there are two counteracting effects where the urea is closer to the reactive plate, but a reduced area of plate is available through the channel length. Interestingly,

for a 5.0 ml/min dialysate flow rate, the overall concentration of the 0.5 mm corrugated channel is much lower than the concentrations for the plain channel and corrugated channel of 1 mm. The effects of this increased mixing and closer bulk flow propagate through the channel and produces a compounded effect, resulting in reduced concentrations of urea at the outlet for the 0.5 mm corrugated channel as seen in Figure 9.6. This increase in performance is associated with a marginal increase in pressure cost and thus is an effective strategy to improve urea removal from the POUR system.

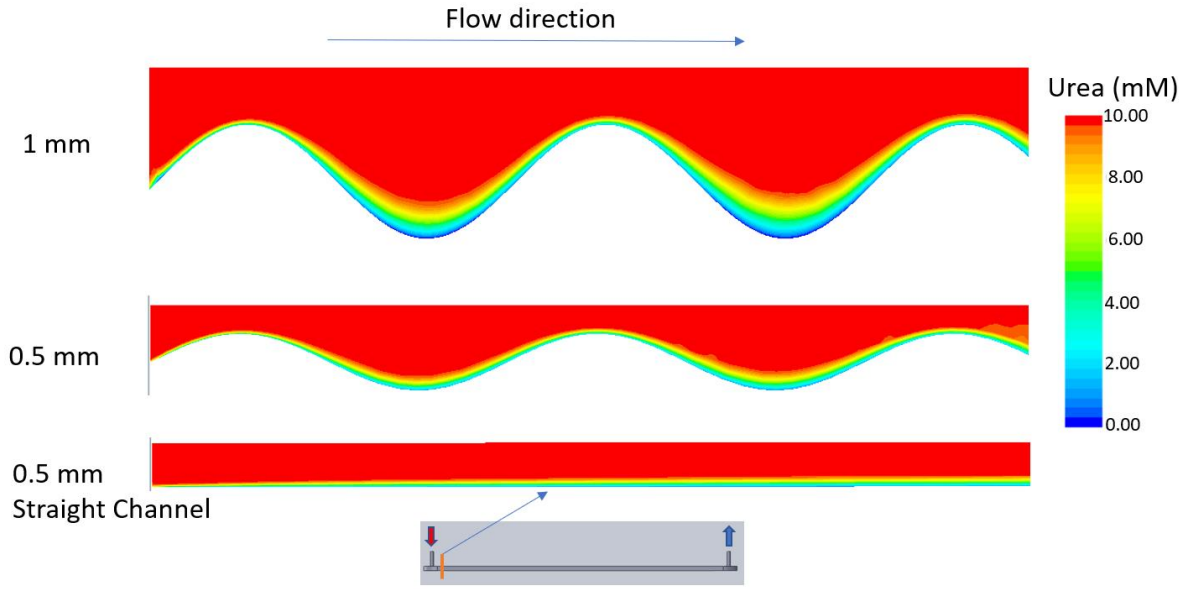

(a)

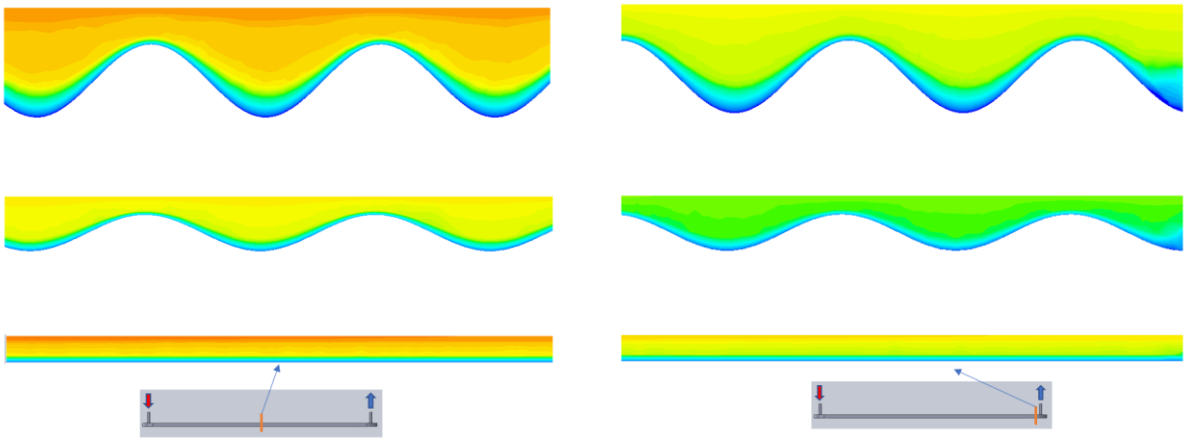

(b) *(c)*

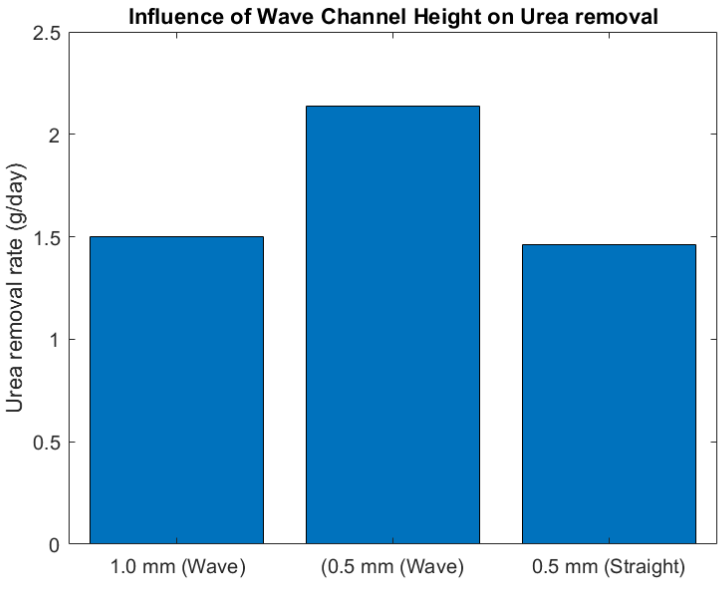

(d)

Figure 9.6: Influence of channel height and comparison against plain channel. (a) the longitudinal view at the channel entrance shows lower concentration of urea for the corrugated 0.5 mm channel. This is due to bringing the bulk concentration of urea closer to the channel along with enhanced mixing of urea due to acceleration and deceleration of the dialysate. These effects propagate through the channel and are observed at (b) mid channel length and (c) at the end of the channel. At the outlet,

the overall concentration of urea can be used to calculate the daily estimated urea removal rate (d) which shows peak performance for the 0.5 mm wave channel.

Influence of flowrates

Three different dialysate flow rates were assessed with an increased range for this design from 0.5 ml/min, 5.0 ml/min & 10.0 ml/min for a 1 mm channel with a 1 mm amplitude corrugated sheet. As the flow rate reduces, the diffusion of urea increases in these slow flows, leading to larger mass boundary layer which reduces the overall bulk concentration of urea. This a favorably effect, which propagates through the channel length leading to increased removal of urea at the lower flow rates Figure 9.7(b). However, the engineering goal of the design is to increase the 'daily urea removal rate.' Slower flows means that fewer passes take place in the day and what is observed is the combined effect of increased per pass removal of urea with the number of passes exacerbates the overall performance of channel Figure 9.7(c). The daily urea removal rate increases from 0.45 g/day to 2.50 g/day as the flow rate increases from 0.5 ml/min to 10.0 ml/min. This means low per pass urea removal combined with more frequent passes results in increased performance of the channel. The associated increase in pressure for 10.0 ml/min flow is 200 Pa, which is important to consider. Additionally, since the POUR channels are only one element in the dialysis system, future work is targeted at optimizing the flow rate with other design considerations from mass exchangers that work between the blood and the dialysate.

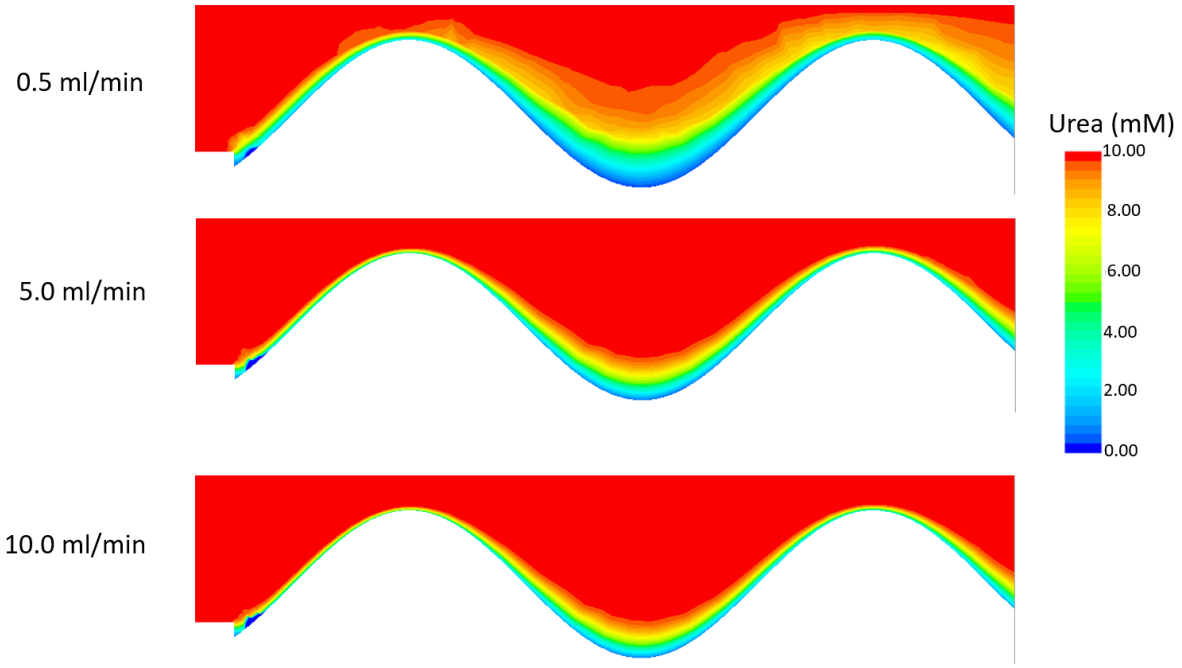
0.5 ml/min
5.0 ml/min
10.0 ml/min
Urea (mM)
10.00
8.00
6.00
4.00
2.00
0.00

(a)

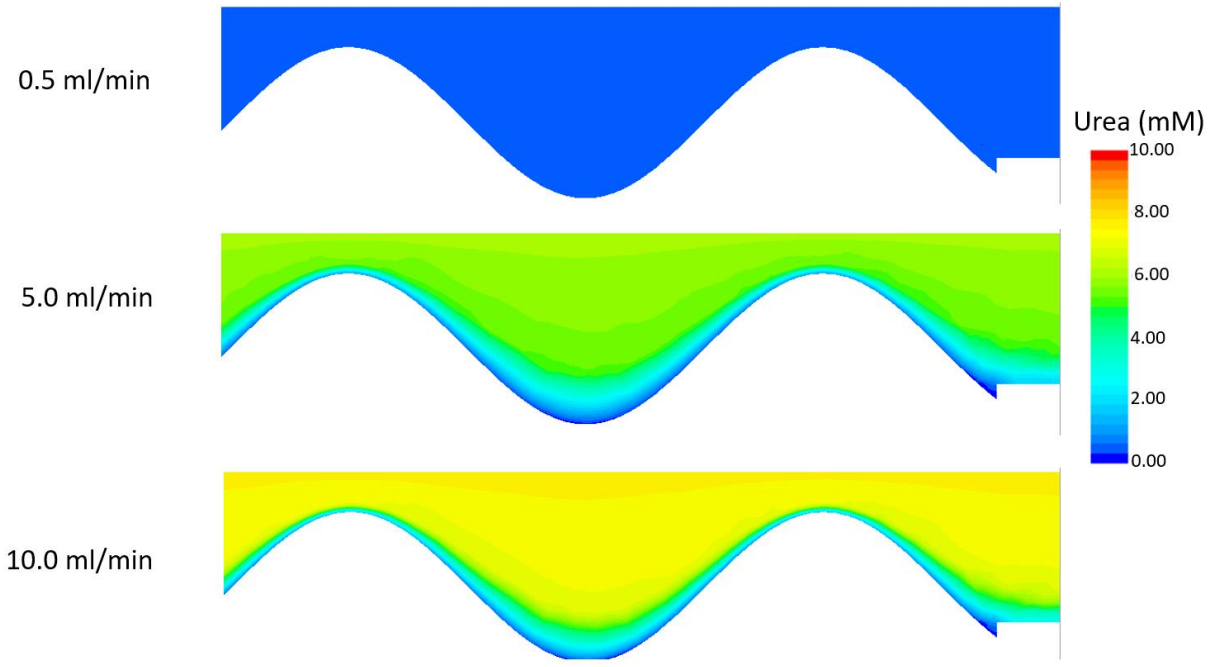
0.5 ml/min
5.0 ml/min
10.0 ml/min
Urea (mM)
10.00
8.00
6.00
4.00
2.00
0.00

(b)

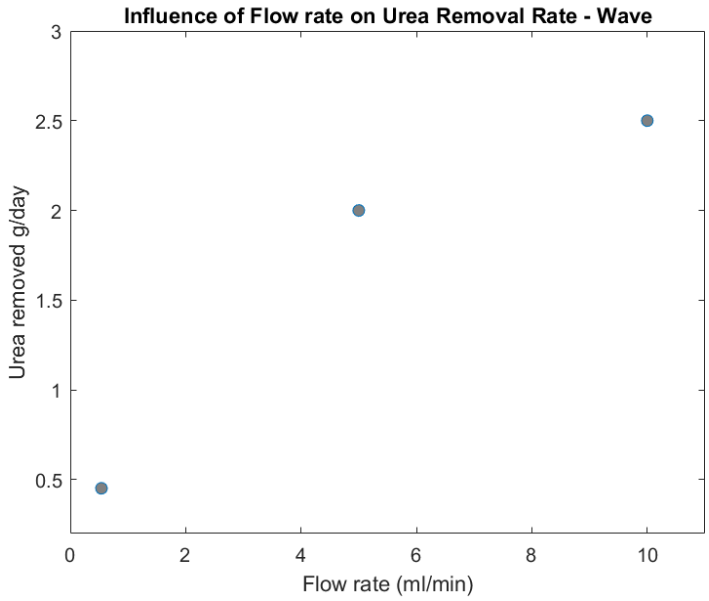

(c)

Figure 9.7: Influence of flow rate. (a) Longitudinal view of the channel entrance shows slower flows promote increased urea removal and larger mass boundary layers which results in lower concentration through the channel length and overall lower concentration at the end of the channel (b). However, since reduced flow rates translate to fewer passes through the day, the daily removal rate falls sharply (c), and larger flow rates are preferred.

Influence of amplitude

The amplitude of the corrugated plate was varied to see the influence on mixing and urea removal from the channel. The increase in amplitude results with an additional increase in available surface area for TiO_2 plate which enables increased urea removal by default. As explained earlier, the reduction in clearance between the bottom plate and top plate results in acceleration of the dialysate which then decelerates as it approaches the trough section. This motion promotes mixing of the fluid which increases the bulk concentration close to the reactive surface as seen in Figure 9.8(a) with the increased mass boundary layer. The combined effect shows a performance increase as

seen in Figure 9.8. However, this improved performance is associated with a steep pressure increase seen as the amplitude increases to 0.90 mm and 0.95 mm. A drop in performance is noticed at 0.95 mm amplitude as well, suggesting either 0.85 mm or 0.90 mm amplitude be used in the final channel design.

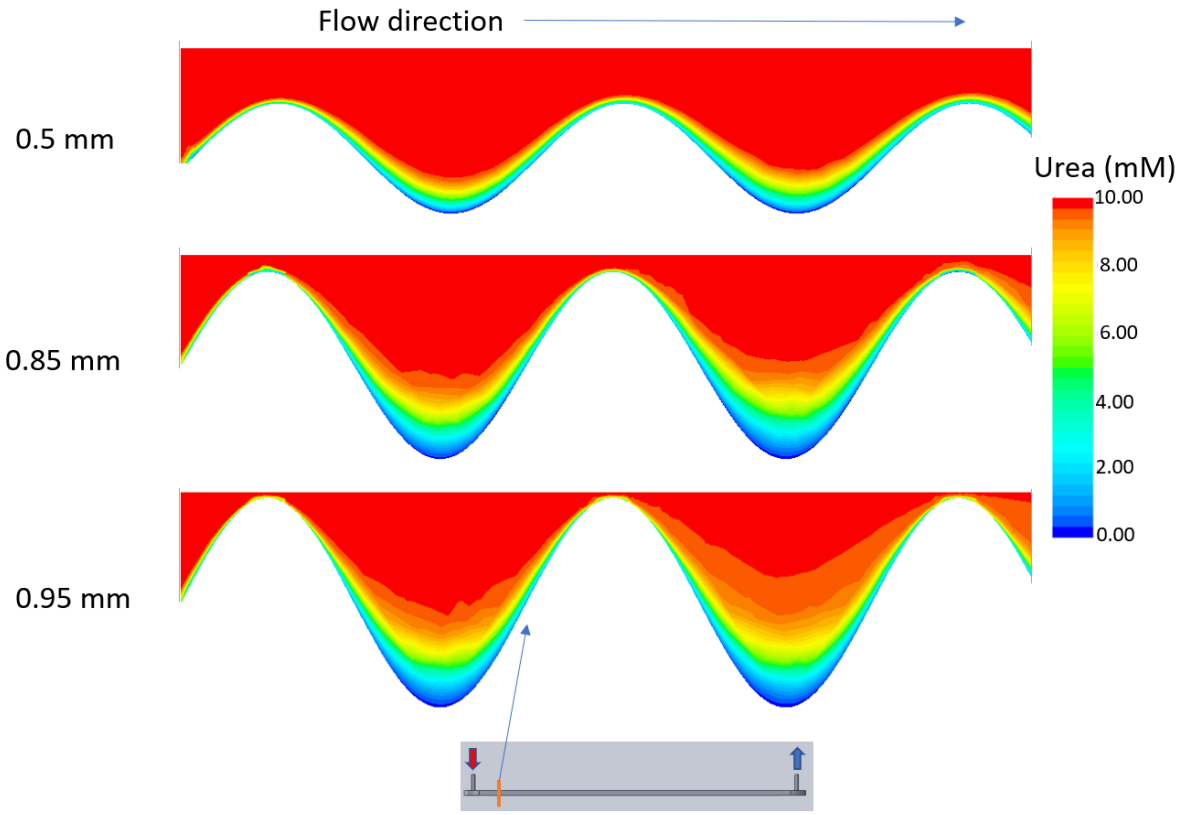

(a)

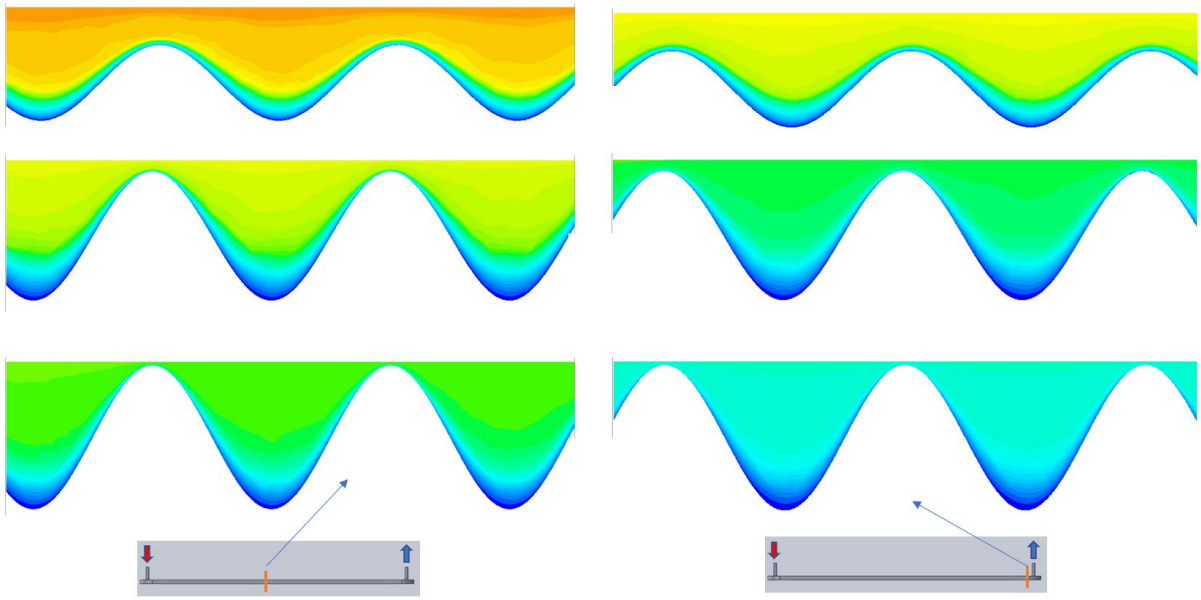

(b) *(c)*

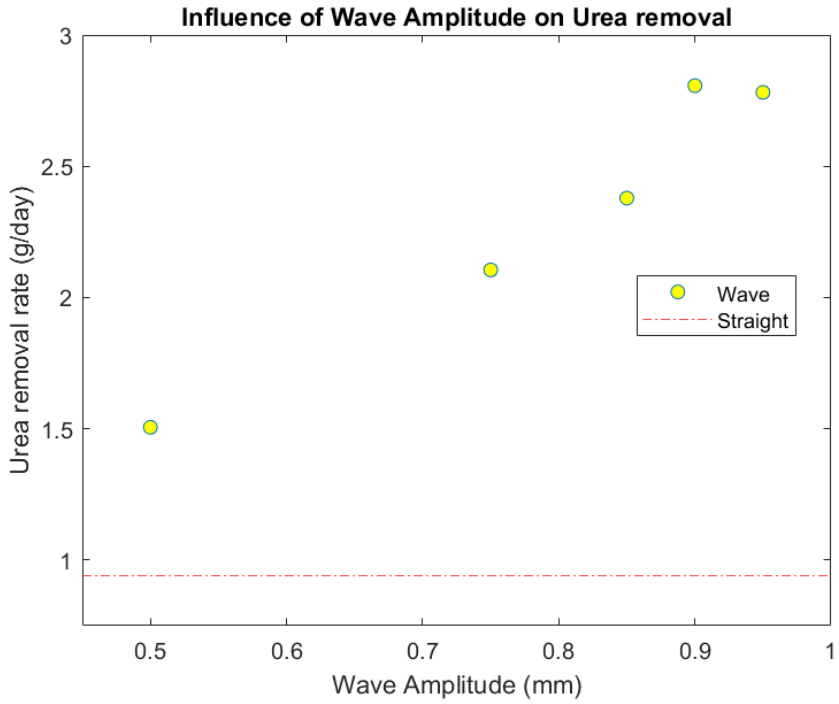
Influence of Wave Amplitude on Urea removal
Urea removal rate (g/day)
Wave Amplitude (mm)
Wave
Straight
3
2.5
2
1.5
1
0.5
0.6
0.7
0.8
0.9
1

(d)

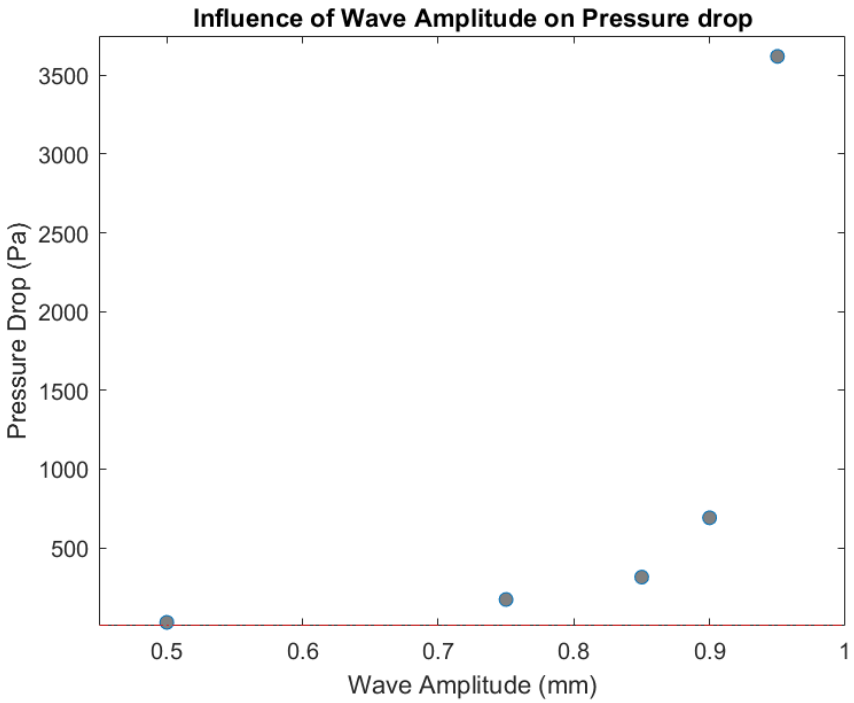

(e)

Figure 9.8: Influence of amplitude of corrugated sheet. Increasing the amplitude increase the reactive surface area and improves mixing resulting in increased removal of urea as seen at (a) start of the channel, (b) half the channel length and (c) end of the channel. A non-linear increase in daily urea removal rate is observed (d) where the improved performance is associated with increasing pressure costs (e).

9.4 Chevron channel design

The increased performance of the wave channel design provided deep insight into the governing physics within the POUR channels. The wave channel presents a huge manufacturing channel as such fine crests and troughs are difficult to manufacture on a glass substrate. To circumvent this problem yet provide a wave like effect a new chevron design was proposed.

Base geometry and fluid physics

Chevron shaped 3D protrusions were etched into the bottom surface of the POUR channels, alternating from each side, which were “plated” with TiO_2 as seen in Figure 9.9. To avoid pockets of circulation of dialysate, a small gap is present between each individual chevron. The base design of chevron contained nineteen alternating chevrons each 12 mm in length and 5 mm wide angled at 30 deg with the horizontal with a height of 0.5 mm. With a total channel height of 1 mm, this means the clearance between the chevron and the top surface reduces to 0.5 mm.

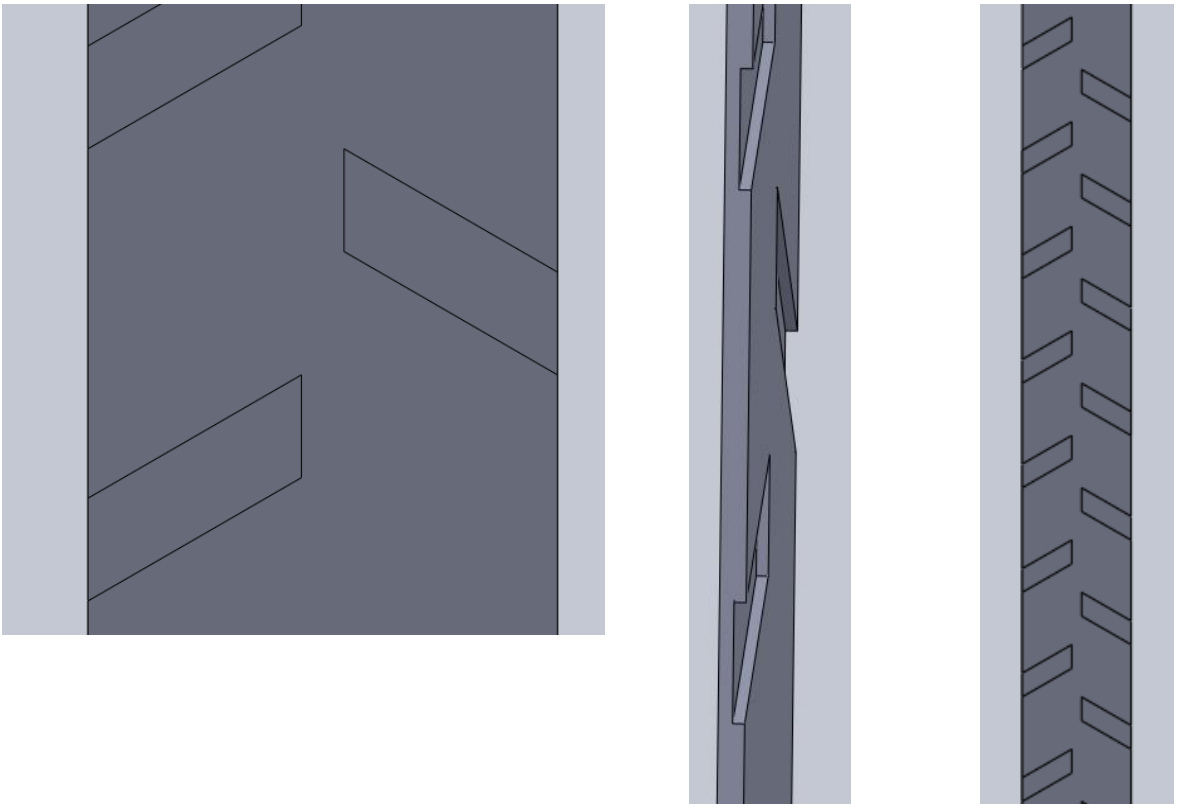

Figure 9.9: Alternating chevrons are etched into the bottom plate of the TiO2 with a gap between the chevrons.

The fundamental difference in the flow in the chevron channel is explained as the fluid is forced to rise over the chevron as seen in Figure 9.10. The fluid begins to twist and turn to squeeze through the small clearance between the chevron and the top plate which forces the middle layers of dialysate to meet the chevron coated TiO_2, which previously would never take place. In previous design, the urea in these layers would diffuse slowly to the lower layers and then be removed by the reactive surface. Additionally, this twisting and turning results in improved mixing of the urea within the dialysate, thus bringing more urea rich fluid close to the reactive TiO_2 surface leading to higher reaction rates and enhance urea removal.

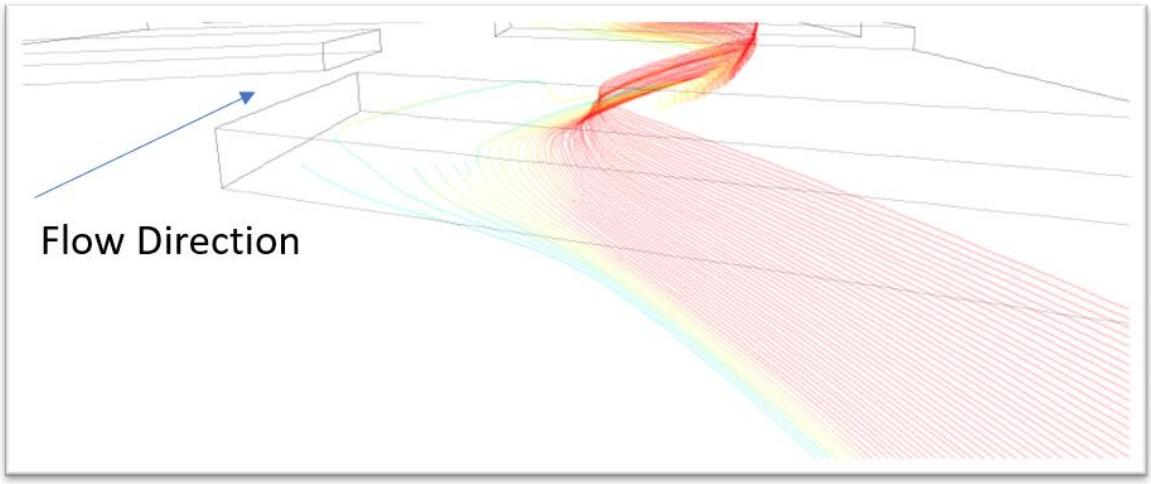

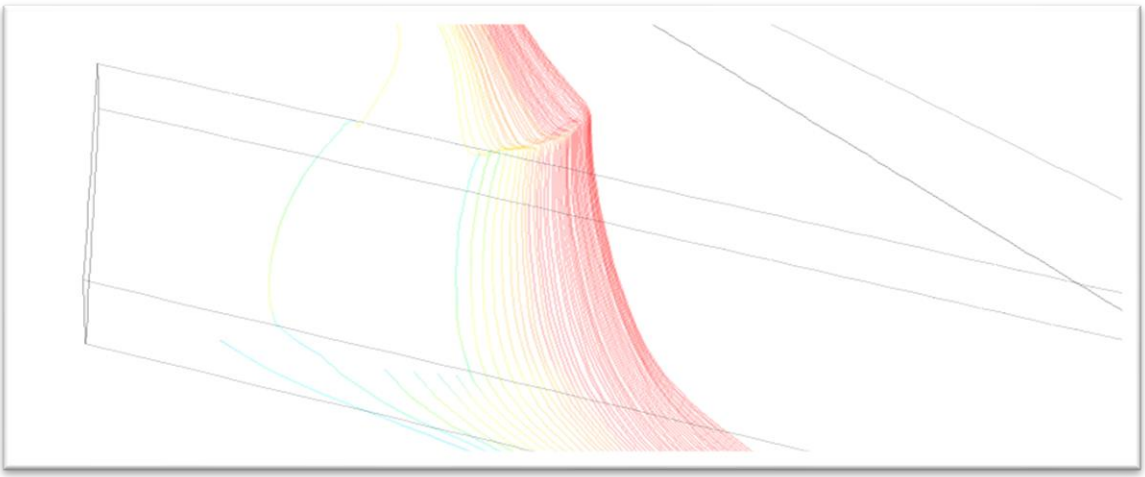

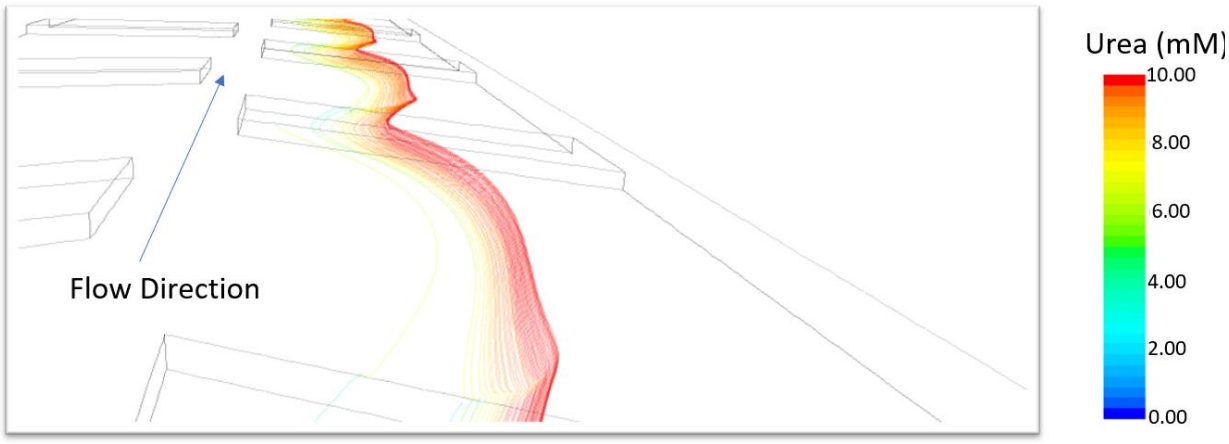

Figure 9.10: Flow over the chevron improves performance. As the dialysate flows over the chevron it is forced to twist and turn, resulting in mixing of urea in the dialysate. Additionally, layers which previously would never contact the reactive surface are now forced to come close to the TiO2 resulting in urea rich dialysate to react and oxidize, improving the performance of the POUR channels.

The fluid as seen in the velocity images in Figure 9.11 accelerates around the chevron edges which promotes mixing as seen previously in the wave design. Finally, the pressure cost of the chevron design is nominal with an increase in pressure drop to 13 Pa.

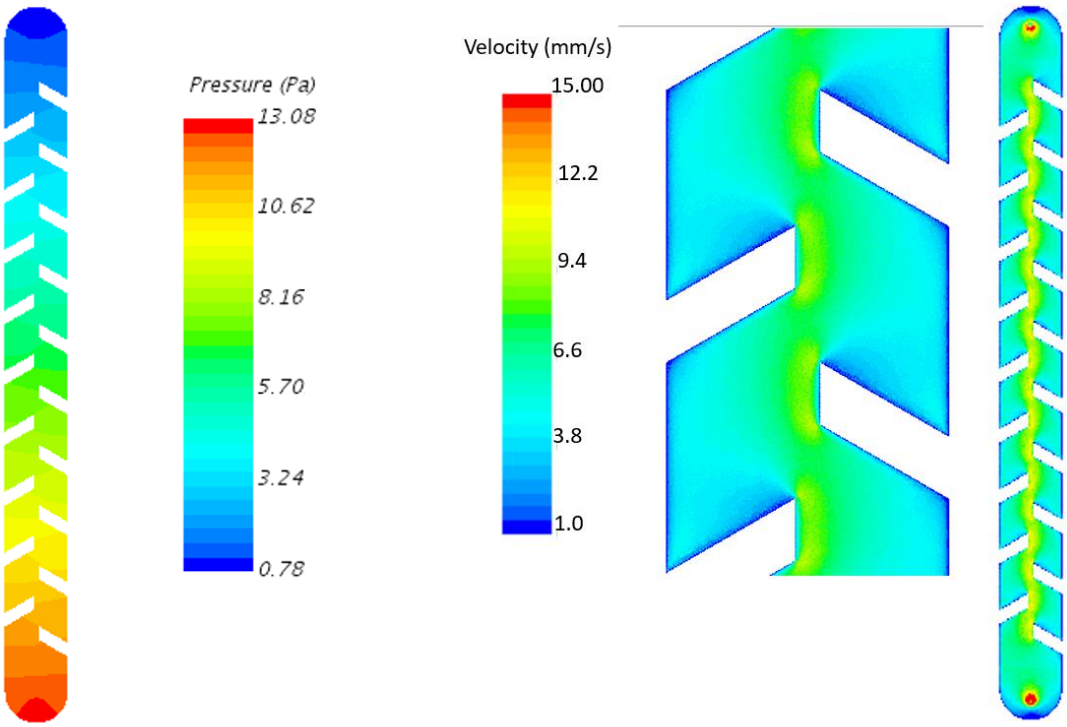

(a) *(b)*

Figure 9.11: Pressure drop and velocity profile in the chevron channel at a dialysate flow rate of 5 ml/min. (a) The pressure drop in the chevron design results increases to 13 Pa and velocity diagram shows the acceleration of the dialysate around the chevron in (b).

Influence of chevron height and flow rate

Earlier in the wave geometry, reducing the height of the channel or reducing clearance between the top and bottom plates improved performance. To obtain a similar improvement in performance, the height of the chevrons was increased from 0.50 mm to 0.75 mm & 0.90 mm. As seen in Figure 9.12 the flow required to squeeze through a smaller clearance which increased the pressure drop across the chevrons, which forced the bulk flow to take the path of least resistance and flow through the gap between the chevrons. Therefore, the flow bypassed the chevrons, and thus avoiding TiO_2

on the chevrons which results in reducing the effect of the chevrons, leading to a sharp fall in performance. This effect may be circumvented by reducing the gap and increasing the length of the chevrons (see next section). Once again, as the flow rate of the dialysate was increased an increase in performance was observed even though the concentration of urea per pass was higher for higher flowrates.

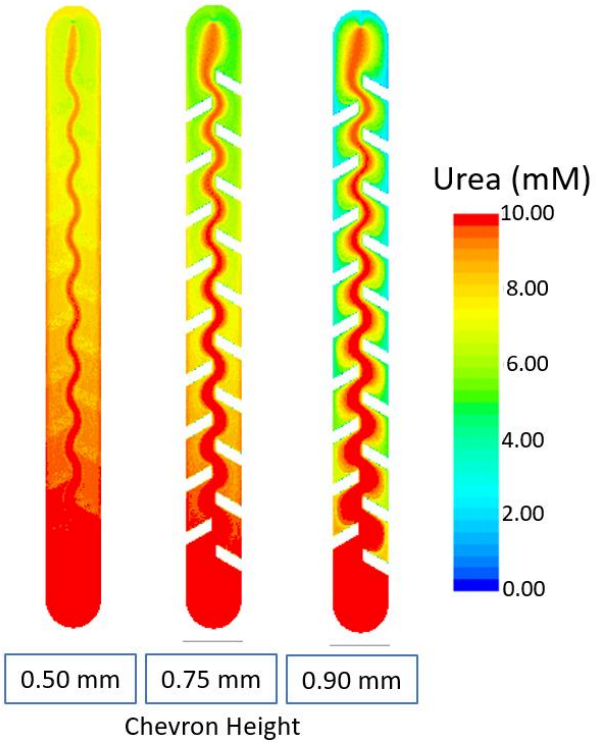

(a)

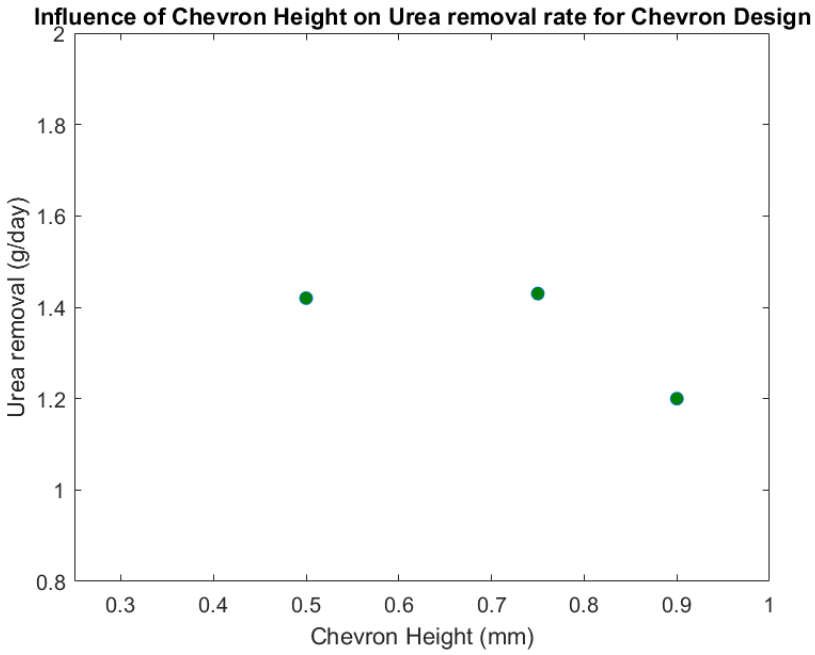

(b)

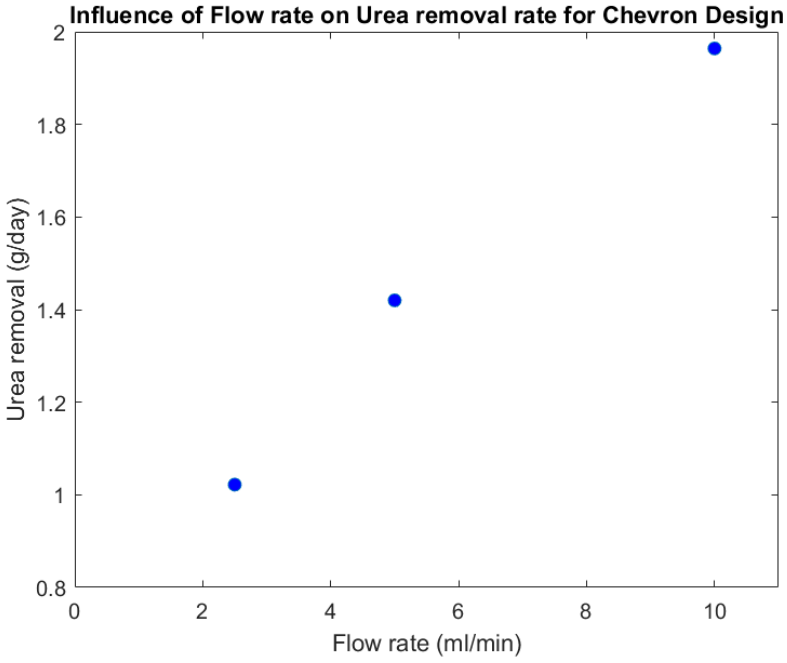

(c)

Figure 9.12: Influence of height of chevrons. As the chevron height increases, the urea rich dialysate prefers the path of least resistance flows through gap between the chevrons (a). This reduces the effect

of the chevron and hence results in fall in performance (b). As the flow rate increases, a linear increase in performance is observed.

Influence of length of the chevron and angle

As a reduction in performance was observed when the dialysate preferred the central gap between the chevrons, the design evolved to reduce the gap of between the chevrons. This was done by increasing the length of the chevrons. As the chevron length increased, and the central gap reduced, the dialysate flow preferred to flow over the chevron rather than around it. This promoted increase removal of urea and improved performance. Due to the same reason, changing the angle of the chevrons resulted in changing the gap between the chevrons which influenced the performance of the channels. The current design of 30 deg angled chevron reported higher urea removal rates than 45 deg and 15 deg angled chevrons.

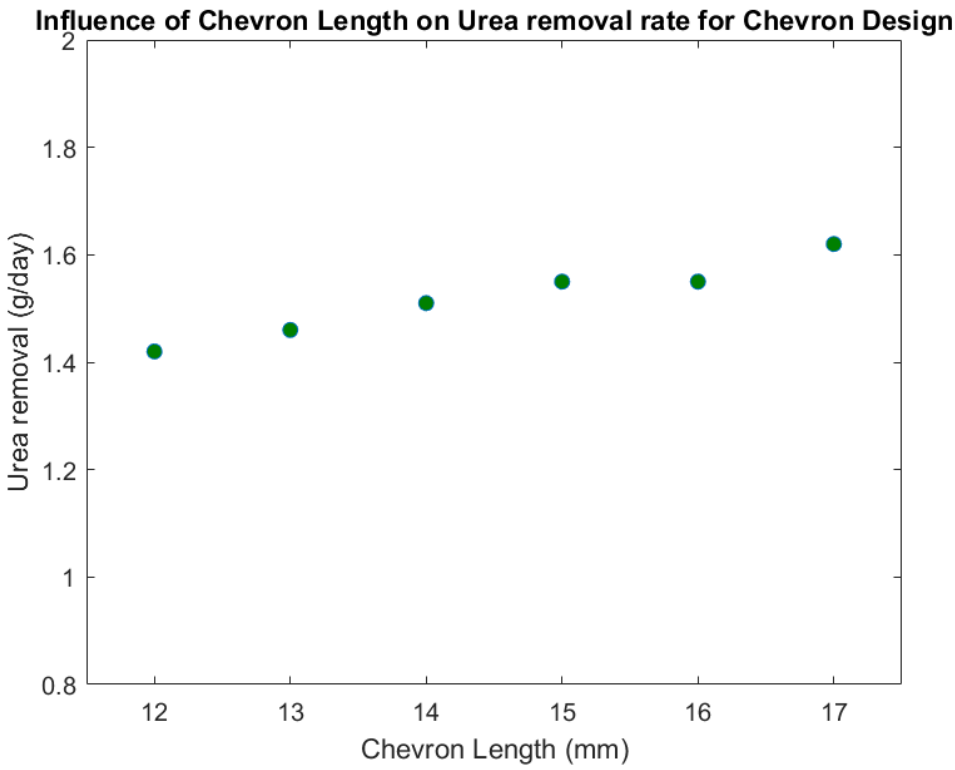

(a)

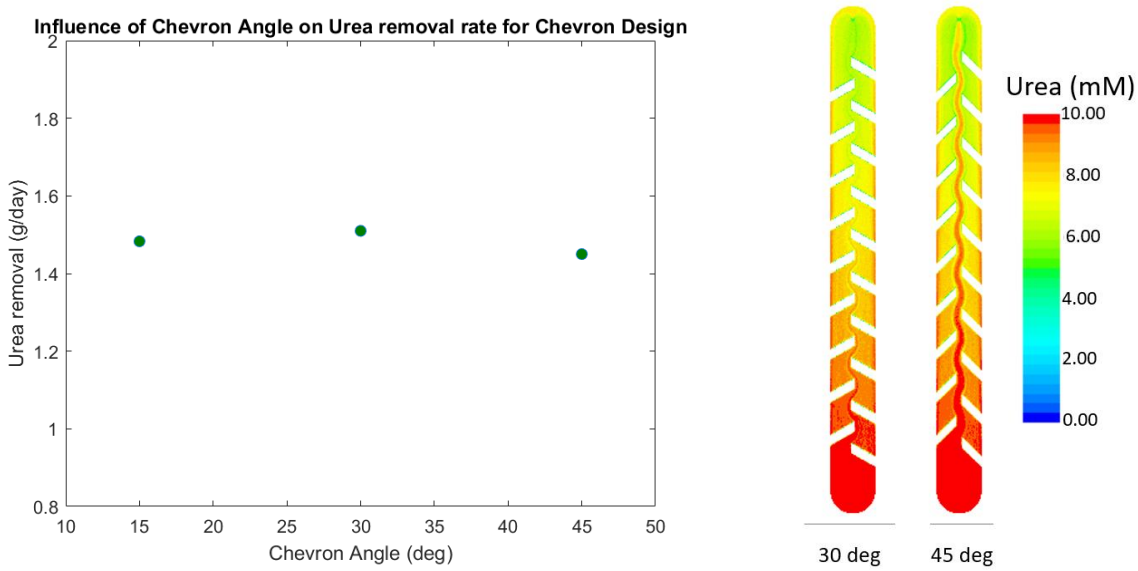

(b) *(c)*

Figure 9.13: Influence of chevron length and angle. As chevron length is increased, the dialysate is forced to go over the chevron, increasing the removal of urea as well as enhancing the mixing of the dialysate. This results in a linear increase in performance with increasing chevron length (a). The chevron angle plays a small influence on performance of the channel, with a decrease in performance (b) as the channel increases to 45 deg. This is again due to increase in the gap between the chevrons allowing dialysate to flow promoting fluid flow through the gap instead of over the chevrons.

Influence of width and spacing of the chevrons

As the width of the chevrons is altered, it affects the inter-chevron distance or the spacing which again affects the number of chevrons per channel. To evaluate the individual influence of each parameter, the number of chevrons was reduced to ten. The width of the chevrons was varied for the ten chevrons and fixed inter-chevron distance of 20 mm. Daily urea removal rate was found to increase with increasing the width of the chevrons as the urea rich dialysate flows over the chevron

for longer periods/lengths, thus bringing the higher concentration urea flow closer to the reactive surface. The inter-chevron spacing was reduced from 20 mm to 17 mm and 15 mm, with constant chevron thickness of 5 mm, and an increase in performance was observed. This suggests that future POUR channel designs should incorporate smaller interspace chevrons, where the chevrons are squeezed closer to one another. Further investigation is required to determine the drop-off in performance in comparison with the associated pressure costs as the chevrons are brought close to each other and with increasing thickness. An optimized chevron size and spacing needs to be determined to maximize the daily urea removal rate.

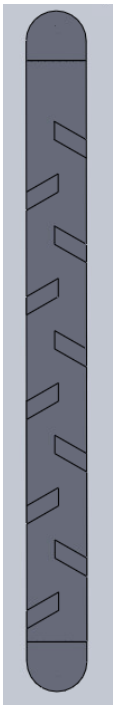

(a)

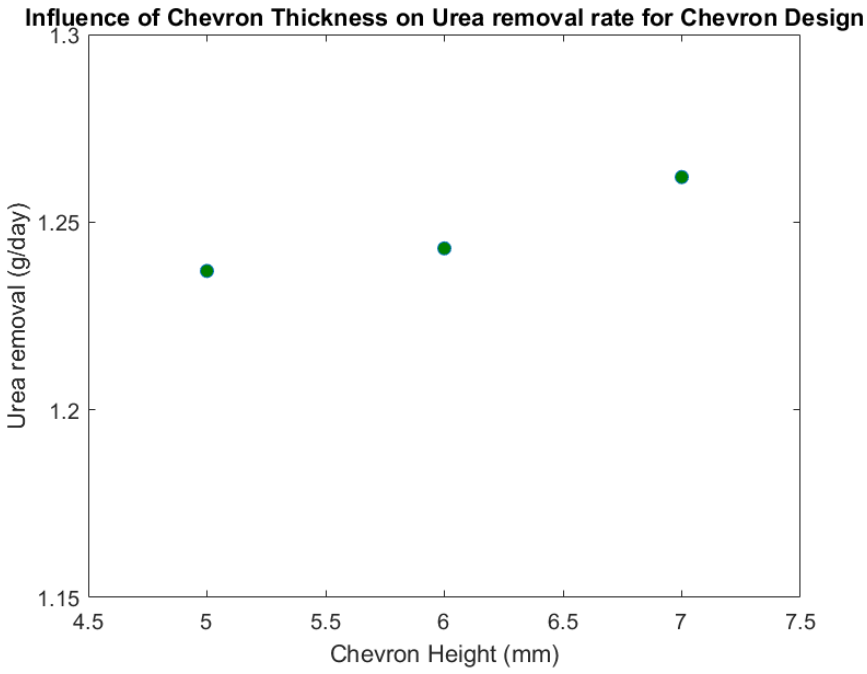

(b)

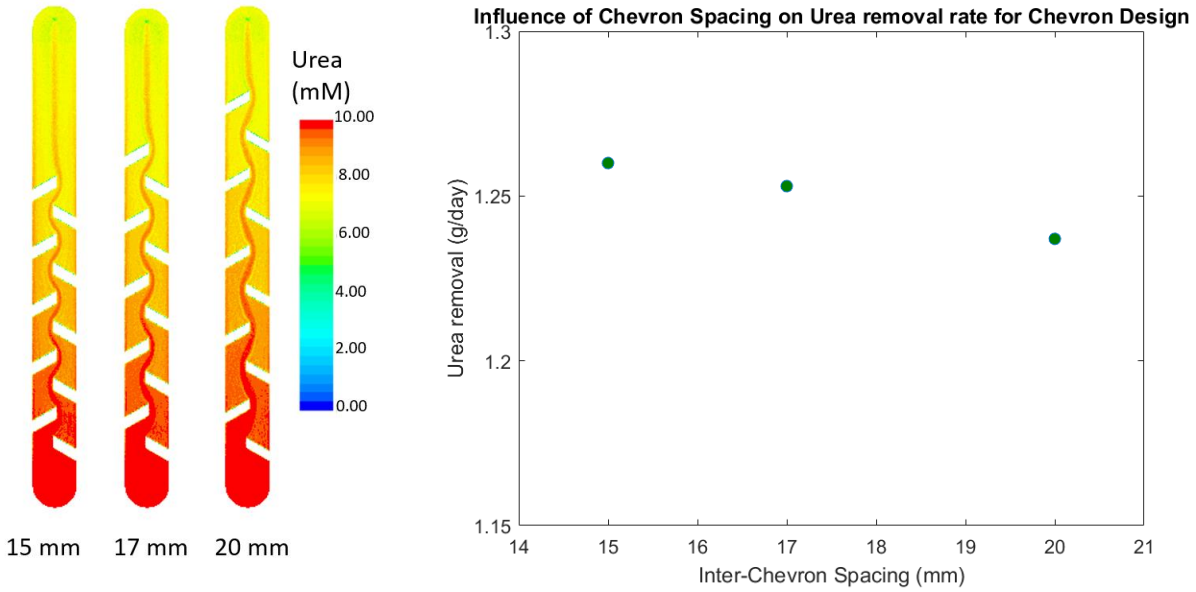

(c) *(d)*

Figure 9.14: To compare the thickness and spacing of chevrons which influence each other in the design the number of chevrons was reduced to 10 (a). As thickness of the chevron increased the performance of the chevrons increased for a fixed inter-chevron spacing of 20 mm (b) as higher concentration flow was closer to the reactive surface for longer lengths (width) of the chevrons. To evaluate the influence of the inter-chevron spacing independently, the chevron thickness was fixed at 5 mm (c). As the chevrons were brought closer to each other, the performance of the channel increased (d). This enables introducing more chevrons as can be seen in (c) allowing more performance to be extracted from these POUR channels.

9.5 Channel design comparison

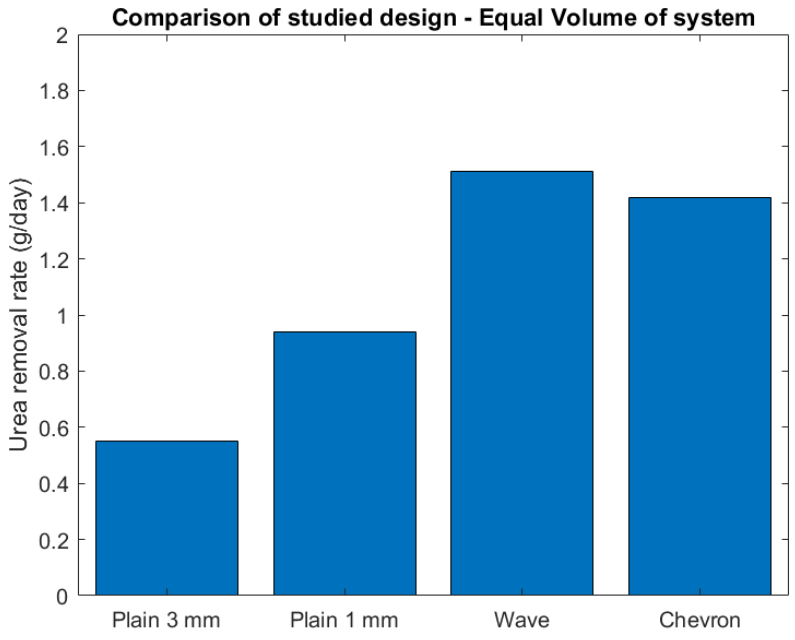

(a)

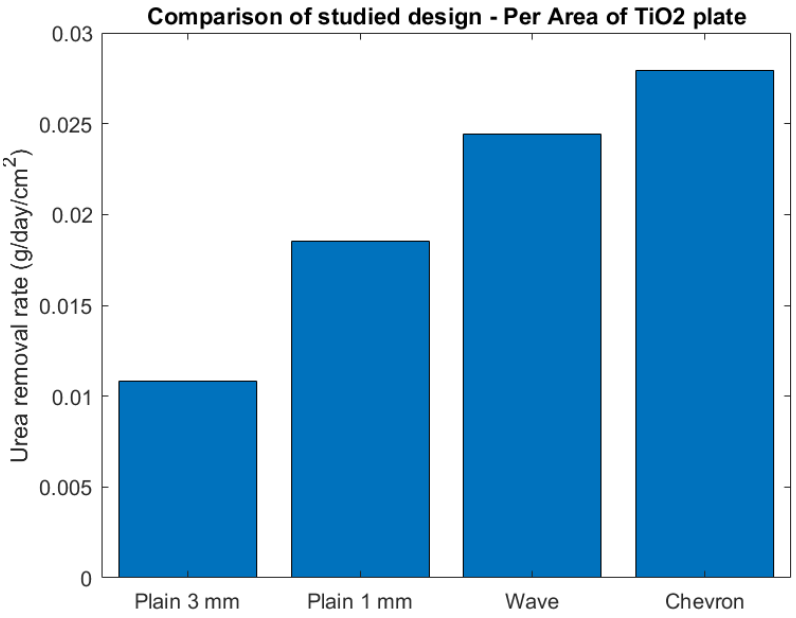

(b)

Figure 9.15: Performance comparison of the four unique designs. (a) The true output of the four different shows increased urea removal rate for the thin channels over the current design. The wave

channel design and the chevron channel design both report high improvements over the current design as well as the thin channel design. (b) When the area of the TiO_2 plate is normalized, the chevron outperforms all other channel designs at achieves higher urea removal rate with the same area of TiO_2 as the thin channel and current 3 mm channel design, while the wave channel design incorporates more reactive surface area due to the corrugated geometry.

Reducing the channel thickness/height to 1 mm results in a dramatic increase in performance by 72.7%. The resulting 0.95 g/day per channel daily removal rate is due to the bulk high concentration dialysate reacting with the TiO_2 due to its proximity resulting high reaction rates even at higher flow velocities through POUR channel. The corrugated or wave channel design increased further increased the daily urea removal rate by 57.9% to 1.5 g/day per channel. This effect is attributed to three different sources. First, the flow undergoes repeated acceleration and deceleration as it passes through the crests and troughs of the corrugate channel. This results in mixing of the dialysate and improving the overall concentration of the dialysate near the reactive surface. Further, at the troughs with the reduced clearance the bulk urea rich dialysate is brought in close contact with TiO_2 plate, thus increasing the reaction rate. Finally, the folds in the bottom plate allow more TiO_2 to be packed in the same volume. This results in more reactive surface and hence higher performance of the POUR channels. Apart from the high pressure drop that develops as the channel size reduces due to the wave, the cost of manufacturing such complex surface is large. To circumvent these problems, the chevron design was proposed which reported slightly lower performance levels with a daily urea removal rate of 1.4 g/day per day, 6.7% lower than the wave, but 50% increase over the thin channels. A major advantage of this design is the ease in fabrication of the bottom plate as opposed to the wave design and is associated with a lower pressure cost for the fluid system as see in Figure 9.16. Figure 9.15 (b) shows when material cost

is included or performance is analyzed per unit area of the reactive surface, the chevron design outperforms all the previous designs, as the size of TiO_2 plate remains consistent with the thin and current channel designs and only requires an additional manufacturing to etch the chevrons. This makes chevron channel design extremely favorable to be incorporated in the next prototype for experimental testing.

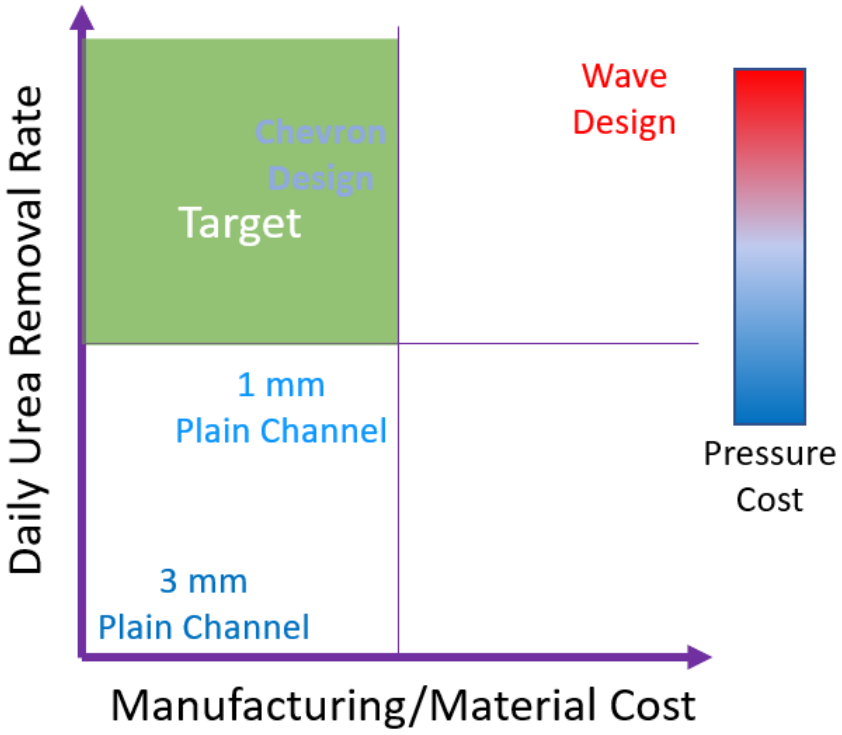

Figure 9.16: Comparison of the performance all four designs with daily urea removal rate with respect to the manufacturing/material cost and pressure cost.

9.6 Discussion

With rising risk factors of chronic kidney disease such as obesity, cardiovascular disease and hypertension and predicted increase in kidney disease patients, there is immediate need for new and improved treatment options. Currently, conventional dialysis is the primary treatment option

for end stage renal disease (ESRD) patients who accept a poor quality of life in exchange for their survival, even though mortality rates are dishearteningly low. Studies have reported improved survival rates with continuous dialysis as well as reduced adverse effects associated currently with conventional dialysis. Presently, there is an unmet need for a portable dialysis system previously unavailable due to sorbent inefficiencies.

However, due to recent advances in material technology, a new TiO_2 based decomposition of urea looks promising. At the Center for Dialysis Innovation, POUR channels take advantage of this method to filter blood and are being evaluated experimentally. With a target of removing 15 g/day, the channels can perform this over thirty-two channels with an individual rate of less than 0.5 g/day. The channels are about 222 mm x 23 mm x 3 mm in size with perpendicular inlet-outlet manifolds. While the system currently functions in laboratory conditions, it is far from feasible for patient use due to the bulkiness of the system and the unoptimized setup for dialysate flow. As the TiO_2 oxidation of urea is saturated in the current design, the question remains whether more urea can be removed from these channels by improving fluid flow and circumventing the diffusion limit of the device which results in the saturation of the performance.

Computational fluid dynamics is a powerful tool to model different fluid systems and flows enabling low turnaround pathways for enhancing our understanding of fluid physics for various engineering problems. This involves numerically solving complex Navier stokes equations that govern fluid flow, which can be extended to resolve mass and heat transfer. However, this theoretical model requires accurate understanding of the flow conditions to produce accurate results. Numerical modelling is as good as the robustness of the input data available along with definite knowledge of the interaction of different physical parameters and their governing

equations. If the model is unreliable, simulations will follow the garbage-in garbage-out adage, leading to meaningless results.

Thus, with the goal of understanding the fluid physics in the POUR dialysis channels, the first step consisted of developing a robust numerical model with sufficient accuracy to explain local physics of the urea decomposition phenomenon. Dialysate flows through the thin POUR channels at low flow rates and can be described as a pure laminar flow characterized by a low Reynolds number. Such flows are smooth, and the flow profile is described as a Poiseuille flow through a rectangular duct. The flow is fully developed and remains unchanged through the channel, which contributes to the lack of instabilities that would otherwise contribute to mixing of the fluid resulting improved transport of urea. Fluid flow in these channels is constrained in the axial direction resulting in no transverse flow, translating to zero convection of urea in the transverse direction. Thus, urea transport is characterized purely by diffusion due to concentration difference developing as a removal of urea from the dialysate. The low diffusion coefficient of urea in water, and low flow velocities of the dialysate through channel are described by high Peclet number flows. Peclet number is an important non-dimensional quantity for the study of transport phenomena and signifies the ratio of advection/convection of a substance by the fluid flow to the diffusion of the substance in the fluid.

At high Peclet number flows, the inherent challenge is to resolve the small diffusion scales to accurately capture the diffusion physics. Errors produced at small lengths can propagate through the domain resulting in large deviations from actual or exact solutions. To resolve this problem, two different grids were utilized each with 8 million and 13 million cells, where the coarser grid discretized the inlet/outlet piping and manifold along with the channel, while the fine mesh was limited to discretizing the channel. Comparison of the two grids, showed close matching at the

start of the channel, while the results deviated significantly towards the end of the channel. This is just as previously mentioned about the propagation of errors and hence there was need to perform and accurate grid independent study. Four different mesh were selected with 50, 100, 150, & 200 prismatic layers in the grid. Prismatic layers are thin stretched cells that take advantage of their small (thin) size in the transverse direction to finely discretize the volume thus enabling accurate representation of the diffusion scales. Increasing the grid size increases the computation cost of the simulations significantly, but results from all four grids were similar with negligible difference even at the end of the channel. To confirm the validity and the accuracy of the 50-prism layer mesh, a comparison was performed against the 200-prism layer mesh for a theoretical higher Peclet number flow (Pe = 30,000) which represented a reduction of the diffusion coefficient by 10, thus increasing the complexity of the resolution of the grid. The results of both the simulations matched once again, thus providing confidence in the coarse 50-prism layer mesh.

With a suitable grid, an important property of the numerical model was the diffusion coefficient of urea. Intrinsic properties of simulations such as diffusion coefficients are selected to be constant, thus maintaining constant fluid flow regimes, such as constant Peclet number flow. Two independent experimental provides different diffusion coefficient values which lead to different results. Previously published literature provided experimental data on the diffusion coefficient at different temperatures and concentration of urea. As the simulations are run at constant temperature the influence of concentration was considered. The experimental data was fit to a linear curve and then exported into the simulations. While this increased computational time, the gain in accuracy justified the significantly longer simulation times which takes place since at each iteration of the simulation, the solver recalculates the local diffusion coefficient at each element, which is an additional 13 million calculations per iterations. The reported results differed from

both the previously used diffusion coefficient values determined from the experimental teams. Hence, the more accurate variable diffusion coefficient model was employed in the simulations, as the constant value models provided incorrect results.

Urea in the numerical simulations is modelled as a passive scalar as a simplified model of the chemical reaction and oxidation of urea at the TiO_2 surface. With the target of removing urea at a constant rate of 15 g/day from the entire dialysis system, the equivalent flux was calculated for a single channel from a series of thirty-two channels, with an individual channel area of 222 mm x 23 mm. This constant flux was imposed at the bottom of the channel which provided a simplified solution. As the chemical reaction of urea has a first order dependence on the concentration of urea, an idealized first order reaction was imposed as the flux, where the area under the first order curve matched the area of the constant reaction curve and the rate of reaction increased linearly with the concentration of urea. This model provided an improved solution where the reaction rate was high at the start of the channel due to the higher concentration of the urea in the dialysate and the reaction rate progressively slows down as the dialysate passes through the channel. To fit the coefficient of linearity the numerical models were iteratively run to and compared with experimental data available from successful trials for 3 mm POUR channels.

With an established coefficient of linearity and first order concentration dependent flux, the numerical models were re-evaluated for different dialysate inlet concentrations and compared with a second experimental data set made available by another independent team, which showed a slight underprediction of urea removal rate by the simulation at lower concentrations (< 10 mM) and an overprediction at higher inlet concentrations (> 10 mM) and was accurate at 10 mM concentration. The underprediction of the performance of POUR channels can be accommodated as this suggests trends reported by the simulations will show improved performance in

experimental runs. Additionally, this underprediction can be corrected by additional adjustment of the coefficient of linearity to better fit the data. As explained earlier, numerical models improve with increased availability of experimental data sets for comparison and validation of the models. The overprediction of urea removal at high concentrations is noteworthy but can be ignored since the goal of the dialysis system is to reduce concentration of urea and input dialysate is either at 10 mM or lower.

With a sufficiently accurate model describing the flow of dialysate through the channel and the diffusion of urea, the numerical model was utilized to predict the performance of different channel designs. The current channel height of 3 mm although small, is still large in comparison to the small diffusion scales (of the order of 10^{-9} or 10^{-10}), hence the first design considered reducing the thickness/height of the channel. With reduced height of 1 mm or 0.5 mm, a sharp increase in performance was observed (~72%). As uniform 10 mM concentration dialysate flows through the channel the TiO_2, the dialysate in contact with the reactive surface loses urea creating a concentration gradient. This promotes the diffusion of urea from the top layers of the dialysate to the bottom layers and is dependent on the diffusion coefficient of urea. By reducing the channel height/thickness, this distance is reduced and hence urea diffuses to the reactive surface earlier, resulting in more decomposition. However, the smaller channels result in increased velocity of the flow, which may deter faster removal of urea, as slow flows promote more diffusion. Apart from this, the pressure drop through the channel increases as the height reduces which requires more pumping power. However, the increase in pressure drop by reducing the thin channel design is about 10 Pa, which is nominal. Additionally, thin channels also reduce the overall structural volume of the device, which reduces the cost and increase the portability of the device. The

advantages of thin channel design overshadow the small cons, and thus is a better design for the POUR channels.

The fluid physics in these plain channels involves the removal of urea from the dialysate as it flows through the channels, which leads to the growth of a mass boundary layer where the concentration of the free stream is 10 mM, and the concentration in the boundary layer is < 10 mM. The growth of this boundary layer is comparable to the thermal boundary layer growth over a flat plate which is dependent on the Prandtl number (describes thermal diffusion through the flow) and is analogous to the Schmidt number (describes the mass diffusion through the flow). The current design of the channels is diffusion limited, meaning the performance is slowed down by the slow diffusion of urea. Increasing the concentration of urea at the bottom of the plate will increase the rate of reaction thereby improving performance. As such, a key component of a future major design of the channel would be to improve mixing of dialysate or bring higher concentration dialysate closer to the reactive surface.

To do this, a corrugated wave plate was introduced at the bottom, which would force the flow to accelerate and decelerate repeatedly, thus introduce changes to the flow field, leading to mixing of the fluid. A dramatic increase in performance was observed with 0.5 mm thick wave design in comparison with the equivalent channel design where urea removal rate increased by 40%. The corrugated plate, in addition, squeezes the dialysate through the crests of the plate which brings the urea fluid in proximity to the reactive surface improving the reaction rates. Finally, the wave geometry increases the available surface area of the TiO_2 plate within the same volume of the channel due to the folds of present in the bottom plate. These three phenomena lead to an overall increase in performance of the channel. Increasing amplitude of the channel enhances all these phenomena and improves removal rate of urea, although a steep pressure cost is associated with

larger amplitudes. Interestingly, a drop in performance is observed as the amplitude changes from 0.90 mm to 0.95 mm. Higher flow rates of dialysate through result in lower diffusion rates of urea and reduced removal rate but are associated with increased number of passes through the channel per day, which offsets the low removal rate and results in better overall performance of the channel.

The wave design with its high performance comes at high pressure requirements but more importantly high manufacturing requirements. Manufacturing a corrugate substrate is extremely challenging and may require specialized techniques to develop them. This increases the overall complexity of the POUR system and results in higher overall costs of the device. which will lead to large. The chevron design circumvents this problem of increased manufacturing complexity as the chevrons can be etched into the substrate easily at low cost. The chevrons change the fluid physics of the channel by allowing a section of fluid to pass through the axial gap between the chevrons and forcing the rest of the fluid to flow over the chevrons themselves. As fluid squeezes itself between the top plate and the chevron, it twists and turn to accommodate for this low clearance, resulting in high concentrated dialysate to contact the TiO_2 surface leading to higher reaction rates. This improves the performance in comparison with the plain channels.

As the height of the chevrons is increased the clearance with the top plate reduces, increasing the pressure drop over each chevron. This forces the dialysate to prefer the central axial gap between the alternating chevrons as this is the path of least resistance. Thus, the dialysate ignores the chevrons, and the flow resembles flow through a plain channel (previous designs) and results in a loss in performance. To overcome this problem, increasing the length of the chevron close the central axial gap, and hence a linear increase in performance is observed with increase in chevron length. A similar effect was observed when the angle of the chevrons was varied, where a larger angel would result in an increase in the central axial gap, thus encourage more fluid to flow through

the gap instead of over the chevrons and reduce overall performance. A chevron angle of 30 deg with the horizontal maximized the urea removal rate. The spacing of the chevrons is interlinked with the width of the chevrons and both can affect the count of the chevrons in the channel. To investigate their individual influences, the chevron count was fixed to ten, and with variation in the chevron width, with constant spacing, larger chevrons reported higher levels of urea removal. This is attributed to increased proximity of the urea rich dialysate with the reactive surface of the TiO_2 for longer lengths (increased width of the chevron). Finally, as the inter-chevron spacing was reduced, the urea removal rates increased which is promising, especially since this enables more chevrons to be introduced in the channel thus increasing the performance of the chevron design. Future investigations need to study the balance between the width, count and inter-chevron spacing to determine the optimum design for maximum urea removal rate.

All the three designs proposed for the POUR channel show increased performance over the current 3 mm channel. The wave design maximizes urea removal for the same flow rate, but is associated with high manufacturing costs, while the chevron channel design performs equally well at lower manufacturing costs. However, in a comparison where the area of the TiO_2 is normalized to compare the designs equally, the chevron design shows the best performance. This is due to the increased urea removal rate and no change in the area of the reactive surface, thus shows the most promise for future experimental trials.

Chapter 10

CONCLUTIONS & FUTURE WORK

With a growing need to improve the status quo of dialysis systems, this study provides a novel design for a wearable dialysis device optimized via CFD simulations. A numerical model was built which resolves the low diffusion scale of urea, incorporating a concentration dependent diffusion coefficient of urea. The model was improved from a constant urea flux from the reactive surface to an idealized first order removal rate which was then fitted to reproduce experimental results. The performance of the current experimental channels was increased by 72.7% by reducing the height of the channels. To improve the mixing and enhance urea removal, a corrugate plate design was introduced. The design was analyzed for different wave amplitudes, flow rates, channel heights to extract maximum performance with the least pressure cost. The final design resulted in a 100% performance increase from the thin channel design. To accommodate for the material and manufacturing complexity and cost of the wave design, an alternative chevron design was proposed. A parametric analysis was run to determine the optimum length, height, and angle of the chevrons. A flow rate analysis was performed to evaluate the performance of the chevron

design under different flow conditions. The chevron design reported improved daily urea removal rate by 47% over thin channels. This study used numerical modelling to enhance the fluid mechanics of the dialysis system and provide design improvements to develop an optimized wearable dialysis device.

Limitations

The study involved the use of numerical modelling to predict the performance of dialysis channels and optimize the design of the channels to enhance their performance. However, the accuracy of the numerical model is dependent on the experimental data, and with only two unique sets of experimental results, the model is limited to reproducing these results. With an expanded range of flow rates, concentration and channel height/thickness, the numerical model will benefit with increased robustness. The simulations model removal of urea as a flux from a surface as opposed to a chemical reaction. The current model sufficiently represents the physics expected within the channels but does overlook the more intricate interactions that may take place by the various chemical species. Additionally, in the wave geometry, illumination of the TiO_2 may wary due to the different angles of incident light as the plate is no longer parallel to the illuminating top plate, which may result in reduced reaction at the TiO_2 surface, which the simulations do not consider. The photo-electrochemical oxidation reaction is an exothermic reaction that produces a temperature gradient which may induce thermal convection of the dialysate and improve mixing, which is currently ignored by the numerical model. Finally, the simulations are an incredibly reliable tool to observe trends in the various channel designs as well as their individual parametric analysis, however, the actual values may differ slightly. Each of the designs in this study needs to be corroborated by experimental runs, if only for the base design to compare the performance parameters reported by the simulations.

Future work

With an improved channel design, the next challenge is to develop a streamlined flow loop to distribute the dialysate into the various panels that house these channels. As reported by this study, the current panel design is extremely inefficient and requires redesign to avoid fluid and pressure losses as the dialysate flows through the channels. While the numerical model predicted the performance of different channels for different flow rates, the flow rates are not uniquely controlled by the channel design. The POUR channels work in tandem with a forward osmosis membrane mass exchanger that functions optimally under certain inlet outlet urea concentrations and flow rates. These concentrations and flow rates need to be determined and used for the performance analysis of the POUR channels, enabling the entire dialysis system to be optimized. Finally, the numerical study needs to be corroborated by experimental data to improve the models as well as compare the performance of the different channel designs, which is expected to be conducted by the experimental teams in the near future.

BIBLIOGRAPHY

[1] P. Joseph *et al.*, "Reducing the global burden of cardiovascular disease, part 1: the epidemiology and risk factors," *Circulation research,* vol. 121, no. 6, pp. 677-694, 2017.

[2] G. A. Roth *et al.*, "Global, regional, and national burden of cardiovascular diseases for 10 causes, 1990 to 2015," *Journal of the American college of cardiology,* vol. 70, no. 1, pp. 1-25, 2017.

[3] D. Mozaffarian *et al.*, "Heart disease and stroke statistics—2015 update: a report from the American Heart Association," *circulation,* vol. 131, no. 4, pp. e29-e322, 2015.

[4] M. Ala-Korpela, "The culprit is the carrier, not the loads: cholesterol, triglycerides and apolipoprotein B in atherosclerosis and coronary heart disease," vol. 48, ed: Oxford University Press, 2019, pp. 1389-1392.

[5] M. Watson *et al.*, "Relation between cigarette smoking and heart failure (from the Multiethnic Study of Atherosclerosis)," *The American journal of cardiology,* vol. 123, no. 12, pp. 1972-1977, 2019.

[6] S. P. Whelton *et al.*, "Associations between lipids and subclinical coronary atherosclerosis," *AIDS (London, England),* vol. 33, no. 6, p. 1053, 2019.

[7] G. Sianos *et al.*, "European experience with the retrograde approach for the recanalisation of coronary artery chronic total occlusions. A report on behalf of the euroCTO club," *EuroIntervention,* vol. 4, no. 1, pp. 84-92, 2008.

[8] T. S. Group*, "The Thrombolysis in Myocardial Infarction (TIMI) trial: phase I findings," *New England Journal of Medicine,* vol. 312, no. 14, pp. 932-936, 1985.

[9] P. Fefer *et al.*, "Current perspectives on coronary chronic total occlusions: the Canadian Multicenter Chronic Total Occlusions Registry," *Journal of the American College of Cardiology,* vol. 59, no. 11, pp. 991-997, 2012.

[10] C. Given *et al.*, "Frequency-domain optical coherence tomography assessment of human carotid atherosclerosis using saline flush for blood clearance without balloon occlusion," *American Journal of Neuroradiology,* vol. 34, no. 7, pp. 1414-1418, 2013.

[11] C. M. Lee, C. J. Engelbrecht, T. D. Soper, F. Helmchen, and E. J. Seibel, "Scanning fiber endoscopy with highly flexible, 1 mm catheterscopes for wide-field, full-color imaging," *Journal of biophotonics,* vol. 3, no. 5-6, pp. 385-407, 2010.

[12] L. E. Savastano and E. J. Seibel, "Scanning fiber angioscopy: A multimodal intravascular imaging platform for carotid atherosclerosis," *Neurosurgery,* vol. 64, no. CN_suppl_1, pp. 188-198, 2017.

[13] C. J. Engelbrecht, R. S. Johnston, E. J. Seibel, and F. Helmchen, "Ultra-compact fiber-optic two-photon microscope for functional fluorescence imaging in vivo," *Optics express,* vol. 16, no. 8, pp. 5556-5564, 2008.

[14] F. Prati *et al.*, "Expert review document on methodology, terminology, and clinical applications of optical coherence tomography: physical principles, methodology of image acquisition, and clinical application for assessment of coronary arteries and atherosclerosis," *European heart journal,* vol. 31, no. 4, pp. 401-415, 2010.

[15] L. E. Savastano *et al.*, "Multimodal laser-based angioscopy for structural, chemical and biological imaging of atherosclerosis," *Nature biomedical engineering,* vol. 1, no. 2, pp. 1-15, 2017.

[16] P. Z. McVeigh, T. Moloney, B. C. Wilson, and M. Wheatcroft, "High-Resolution Scanning Fiber Angioscopy as an Adjuvant to Fluoroscopy During Endovascular Interventions," *Journal of Endovascular Therapy,* vol. 25, no. 5, pp. 617-623, 2018.

[17] J. P. Ehlers *et al.*, "Evaluation of contrast agents for enhanced visualization in optical coherence tomography," *Investigative ophthalmology & visual science,* vol. 51, no. 12, pp. 6614-6619, 2010.
[18] U. Navaneethan, J. H. Moon, and T. Itoi, "Biliary interventions using single-operator cholangioscopy," *Digestive Endoscopy,* vol. 31, no. 5, pp. 517-526, 2019.
[19] A. K. Gore *et al.*, "Prospective comparison between saline and radiocontrast for intracoronary imaging with optical coherence tomography," *Cardiovascular Imaging,* vol. 13, no. 9, pp. 2060-2062, 2020.
[20] V. G. Patel *et al.*, "Angiographic Success and Procedural Complications in Patients Undergoing Percutaneous Coronary Chronic Total Occlusion Interventions," *A Weighted Meta-Analysis of 18,061 Patients From 65 Studies,* vol. 6, no. 2, pp. 128-136, 2013, doi: 10.1016/j.jcin.2012.10.011.
[21] A. Kalniņš, I. Strēle, I. Kurcalte, A. Lejnieks, and A. Ērglis, "Chronic Total Coronary Artery Occlusion Recanalisation with Percutaneous Coronary Intervention—Single Centre 10-Year Experience," in *Proceedings of the Latvian Academy of Sciences. Section B. Natural, Exact, and Applied Sciences.*, 2018, vol. 72, no. 1: Sciendo, pp. 1-8.
[22] J. A. Suero *et al.*, "Procedural outcomes and long-term survival among patients undergoing percutaneous coronary intervention of a chronic total occlusion in native coronary arteries: a 20-year experience," *Journal of the American College of Cardiology,* vol. 38, no. 2, pp. 409-414, 2001.
[23] J. P. Fernandez *et al.*, "Beyond the balloon: excimer coronary laser atherectomy used alone or in combination with rotational atherectomy in the treatment of chronic total occlusions, non-crossable and non-expansible coronary lesions," *EuroIntervention: journal of EuroPCR in collaboration with the Working Group on Interventional Cardiology of the European Society of Cardiology,* vol. 9, no. 2, pp. 243-250, 2013.
[24] Y. Kawase *et al.*, "In vivo volumetric analysis of coronary stent using optical coherence tomography with a novel balloon occlusion-flushing catheter: a comparison with intravascular ultrasound," *Ultrasound in medicine & biology,* vol. 31, no. 10, pp. 1343-1349, 2005.
[25] Z. J. Shen, H. M. García-García, C. Schultz, M. Van Der Ent, and P. W. Serruys, "Crossing of a calcified “balloon uncrossable” coronary chronic total occlusion facilitated by a laser catheter: A case report and review recent four years' experience at the Thoraxcenter," *International journal of cardiology,* vol. 145, no. 2, pp. 251-254, 2010.
[26] A. Sakes, M. van der Wiel, D. Dodou, and P. Breedveld, "Endovascular crossing of chronic total occlusions using an impulse: an explorative design study," *Cardiovascular Engineering and Technology,* vol. 8, no. 2, pp. 145-163, 2017.
[27] G. W. Stone *et al.*, "Percutaneous recanalization of chronically occluded coronary arteries: procedural techniques, devices, and results," *Catheterization and cardiovascular interventions,* vol. 66, no. 2, pp. 217-236, 2005.
[28] M. R. Selmon, G. Hansen, and C. Milo, "Intravascular catheter system for treating a vascular occlusion," ed: Google Patents, 2000.
[29] J. I. Levatter, "Fiber optic laser catheter and method of using it," ed: Google Patents, 2006.
[30] C. Kittrell, R. M. Cothren Jr, and M. S. Feld, "Catheter for laser angiosurgery," ed: Google Patents, 1990.
[31] G. S. Abela, S. E. Friedl, and E. D. Mathews, "Cardiac ablation catheters and method," ed: Google Patents, 1995.
[32] T. R. Winston and J. M. Neet, "Expandable laser catheter," ed: Google Patents, 2000.
[33] S. K. Morcos, "Prevention of contrast media–induced nephrotoxicity after angiographic procedures," *Journal of vascular and interventional radiology,* vol. 16, no. 1, pp. 13-23, 2005.

[34] T. H. Au, A. Bruckner, S. M. Mohiuddin, and D. E. Hilleman, "The prevention of contrast-induced nephropathy," *Annals of Pharmacotherapy,* vol. 48, no. 10, pp. 1332-1342, 2014.
[35] T. Simard *et al.*, "Pre-clinical comparison of saline and contrast for intravascular imaging using optical coherence tomography," *Canadian Journal of Cardiology,* vol. 33, no. 10, p. S188, 2017.
[36] N. K. Mahesh, A. Gupta, P. Barward, R. Vijayvergiya, P. Sharma, and A. Mahesh, "Study of saline optical coherence tomography–guided percutaneous coronary intervention (SOCT-PCI Study)," *Indian Heart Journal,* vol. 72, no. 4, pp. 239-243, 2020.
[37] A. Gupta *et al.*, "Saline as an alternative to radio-contrast for optical coherence tomography guided percutaneous coronary intervention: A prospective comparison," *Cardiovascular Revascularization Medicine,* 2021.
[38] P. Patwari *et al.*, "Assessment of coronary plaque with optical coherence tomography and high-frequency ultrasound," *The American journal of cardiology,* vol. 85, no. 5, pp. 641-644, 2000.
[39] L. Hermus, G. Van Dam, and C. Zeebregts, "Advanced carotid plaque imaging," *European Journal of Vascular and Endovascular Surgery,* vol. 39, no. 2, pp. 125-133, 2010.
[40] N. Ghata, R. C. Aldredge, J. Bec, and L. Marcu, "Computational analysis of the effectiveness of blood flushing with saline injection from an intravascular diagnostic catheter," *International journal for numerical methods in biomedical engineering,* vol. 30, no. 11, pp. 1278-1293, 2014.
[41] A. K. Chin, "Endoscopic Techniques and Technology in Cardiac Surgery," *Cardiovascular Engineering and Technology,* vol. 1, no. 1, pp. 66-76, 2010.
[42] V. Hou, D. Levin, C. Hagen, W. L. Lombardi, E. Seibel, and J. Petersen, "High-resolution angioscopy of proximal chronic total occlusion microchannels using the scanning fiber endoscope," *Journal of the American College of Cardiology,* vol. 71, no. 11S, pp. A1051-A1051, 2018.
[43] T. Yamaguchi *et al.*, "Safety and feasibility of an intravascular optical coherence tomography image wire system in the clinical setting," *The American journal of cardiology,* vol. 101, no. 5, pp. 562-567, 2008.
[44] H. Wolinsky and S. N. Thung, "Use of a perforated balloon catheter to deliver concentrated heparin into the wall of the normal canine artery," *Journal of the American College of Cardiology,* vol. 15, no. 2, pp. 475-481, 1990.
[45] M. Sadeghi *et al.*, "Total resuscitative endovascular balloon occlusion of the aorta causes inflammatory activation and organ damage within 30 minutes of occlusion in normovolemic pigs," *BMC surgery,* vol. 20, no. 1, pp. 1-11, 2020.
[46] K. Mitsuzuka *et al.*, "A Parametric Study of Flushing Conditions for Improvement of Angioscopy Visibility," *Journal of Functional Biomaterials,* vol. 13, no. 2, p. 69, 2022.
[47] R. Piper, P. J. Carr, L. J. Kelsey, A. C. Bulmer, S. Keogh, and B. J. Doyle, "The mechanistic causes of peripheral intravenous catheter failure based on a parametric computational study," *Scientific reports,* vol. 8, no. 1, pp. 1-12, 2018.
[48] A. Rajiv, Y. Zhou, J. Ridge, P. G. Reinhall, and E. J. Seibel, "Electromechanical model-based design and testing of fiber scanners for endoscopy," *Journal of Medical Devices,* vol. 12, no. 4, 2018.
[49] B. Roe, E. Swenson, S. Hepps, and D. Bruns, "Total body perfusion in cardiac operations: use of perfusate of balanced electrolytes and low molecular weight Dextran," *Archives of surgery,* vol. 88, no. 1, pp. 128-134, 1964.
[50] M. R. Rees and L. K. Michalis, "Activated-guidewire technique for treating chronic coronary artery occlusion," *Lancet (London, England),* vol. 346, no. 8980, pp. 943-944, 1995.
[51] V. Filipce, P. Pillai, O. Makiese, H. Zarzour, M. Pigott, and M. Ammirati, "Quantitative and qualitative analysis of the working area obtained by endoscope and microscope in various approaches to the anterior communicating artery complex using computed tomography-based frameless stereotaxy: a cadaver study," *Neurosurgery,* vol. 65, no. 6, pp. 1147-1153, 2009.

[52] A. Zaman, G. Helft, S. Worthley, and J. Badimon, "The role of plaque rupture and thrombosis in coronary artery disease," *Atherosclerosis,* vol. 149, no. 2, pp. 251-266, 2000.

[53] A. P. Burke, A. Farb, G. T. Malcom, Y.-h. Liang, J. E. Smialek, and R. Virmani, "Plaque rupture and sudden death related to exertion in men with coronary artery disease," *Jama,* vol. 281, no. 10, pp. 921-926, 1999.

[54] M. J. Davies and A. C. Thomas, "Plaque fissuring--the cause of acute myocardial infarction, sudden ischaemic death, and crescendo angina," *British heart journal,* vol. 53, no. 4, p. 363, 1985.

[55] C. M. Flory, "Arterial occlusions produced by emboli from eroded aortic atheromatous plaques," *The American journal of pathology,* vol. 21, no. 3, p. 549, 1945.

[56] P. W. Weber, C. A. Coursey, L. E. Howle, R. C. Nelson, E. B. Nichols, and S. T. Schindera, "Modifying peripheral IV catheters with side holes and side slits results in favorable changes in fluid dynamic properties during the injection of iodinated contrast material," *American Journal of Roentgenology,* vol. 193, no. 4, pp. 970-977, 2009.

[57] A. Saxena, E. Y. K. Ng, and S. T. Lim, "Imaging modalities to diagnose carotid artery stenosis: progress and prospect," *Biomedical engineering online,* vol. 18, no. 1, pp. 1-23, 2019.

[58] P. Velagapudi *et al.*, "Role of coronary computed tomography angiography in percutaneous coronary intervention of chronic total occlusions," *Current Cardiovascular Imaging Reports,* vol. 13, no. 7, pp. 1-10, 2020.

[59] M. C. Williams, D. E. Newby, and E. D. Nicol, "Coronary atherosclerosis imaging by CT to improve clinical outcomes," *Journal of cardiovascular computed tomography,* vol. 13, no. 5, pp. 281-287, 2019.

[60] A. J. Nelson, M. Ardissino, and P. J. Psaltis, "Current approach to the diagnosis of atherosclerotic coronary artery disease: more questions than answers," *Therapeutic Advances in Chronic Disease,* vol. 10, p. 2040622319884819, 2019.

[61] C. R. Pasarikovski, J. Cardinell, and V. X. Yang, "Perspective review on applications of optics in cerebral endovascular neurosurgery," *Journal of Biomedical Optics,* vol. 24, no. 3, p. 030601, 2019.

[62] R. D. Madder, D. H. Steinberg, and R. D. Anderson, "Multimodality direct coronary imaging with combined near-infrared spectroscopy and intravascular ultrasound: Initial US experience," *Catheterization and Cardiovascular Interventions,* vol. 81, no. 3, pp. 551-557, 2013.

[63] H. M. Garcia-Garcia, V. Azizi, and A. H. Kajita, "Cardiovascular devices: Potent angioscopy for weak plaques," *Nature Biomedical Engineering,* vol. 1, no. 2, pp. 1-2, 2017.

[64] A. Gupta *et al.*, "Saline as an alternative to radio-contrast for optical coherence tomography-guided percutaneous coronary intervention: a prospective comparison," *Cardiovascular Revascularization Medicine,* vol. 34, pp. 86-91, 2022.

[65] F. Fracassi, M. Roberto, and G. Niccoli, "Current interventional coronary applications of excimer laser," *Expert review of medical devices,* vol. 10, no. 4, pp. 541-549, 2013.

[66] P. Z. McVeigh *et al.*, "High-resolution angioscopic imaging during endovascular neurosurgery," *Neurosurgery,* vol. 75, no. 2, pp. 171-180, 2014.

[67] S. Faisal, E. J. Seibel, and A. Aliseda, "Optimization Study of the Hemodynamics of Saline Flushing in Endoscopic Imaging of Chronic Total Occlusions (CTOs)," *Cardiovascular Engineering and Technology,* vol. 12, no. 5, pp. 541-555, 2021.

[68] C. Luo *et al.*, "Predictors of interventional success of antegrade PCI for CTO," *JACC: Cardiovascular Imaging,* vol. 8, no. 7, pp. 804-813, 2015.

[69] A. Rolf *et al.*, "Preprocedural coronary CT angiography significantly improves success rates of PCI for chronic total occlusion," *The international journal of cardiovascular imaging,* vol. 29, no. 8, pp. 1819-1827, 2013.

[70] T. Takayama, "System and Procedure of Nonocclusion Type of Angioscopy," in *Coronary Angioscopy*: Springer, 2015, pp. 57-65.
[71] A. S. Levey and J. Coresh, "Chronic kidney disease," *The lancet,* vol. 379, no. 9811, pp. 165-180, 2012.
[72] A. S. Levey, C. Becker, and L. A. Inker, "Glomerular filtration rate and albuminuria for detection and staging of acute and chronic kidney disease in adults: a systematic review," *Jama,* vol. 313, no. 8, pp. 837-846, 2015.
[73] A. C. Webster, E. V. Nagler, R. L. Morton, and P. Masson, "Chronic kidney disease," *The lancet,* vol. 389, no. 10075, pp. 1238-1252, 2017.
[74] G. Eknoyan *et al.*, "KDIGO 2012 clinical practice guideline for the evaluation and management of chronic kidney disease," *Kidney Int,* vol. 3, no. 1, pp. 5-14, 2013.
[75] J. S. Thurlow *et al.*, "Global epidemiology of end-stage kidney disease and disparities in kidney replacement therapy," *American journal of nephrology,* vol. 52, no. 2, pp. 98-107, 2021.
[76] T. Liyanage *et al.*, "Worldwide access to treatment for end-stage kidney disease: a systematic review," *The Lancet,* vol. 385, no. 9981, pp. 1975-1982, 2015.
[77] B. M. Robinson, T. Akizawa, K. J. Jager, P. G. Kerr, R. Saran, and R. L. Pisoni, "Factors affecting outcomes in patients reaching end-stage kidney disease worldwide: differences in access to renal replacement therapy, modality use, and haemodialysis practices," *The Lancet,* vol. 388, no. 10041, pp. 294-306, 2016.
[78] A. J. Collins, R. N. Foley, D. T. Gilbertson, and S.-C. Chen, "United States Renal Data System public health surveillance of chronic kidney disease and end-stage renal disease," *Kidney international supplements,* vol. 5, no. 1, pp. 2-7, 2015.
[79] K. P. McCullough, H. Morgenstern, R. Saran, W. H. Herman, and B. M. Robinson, "Projecting ESRD incidence and prevalence in the United States through 2030," *Journal of the American Society of Nephrology,* vol. 30, no. 1, pp. 127-135, 2019.
[80] G. L. Queeley and E. S. Campbell, "Comparing treatment modalities for end-stage renal disease: a meta-analysis," *American health & drug benefits,* vol. 11, no. 3, p. 118, 2018.
[81] R. Saran *et al.*, "US renal data system 2017 annual data report: epidemiology of kidney disease in the United States," *American Journal of Kidney Diseases,* vol. 71, no. 3, p. A7, 2018.
[82] R. Saran *et al.*, "US renal data system 2016 annual data report: epidemiology of kidney disease in the United States," *American journal of kidney diseases,* vol. 69, no. 3, pp. A7-A8, 2017.
[83] C. Ronco, M. Neri, A. Lorenzin, F. Garzotto, and W. R. Clark, "Multidimensional classification of dialysis membranes," *Expanded Hemodialysis,* vol. 191, pp. 115-126, 2017.
[84] A. Davenport, V. Gura, C. Ronco, M. Beizai, C. Ezon, and E. Rambod, "A wearable haemodialysis device for patients with end-stage renal failure: a pilot study," *The Lancet,* vol. 370, no. 9604, pp. 2005-2010, 2007.
[85] K. Leivaditis, S. Panagoutsos, A. Roumeliotis, V. Liakopoulos, and V. Vargemezis, "Vascular access for hemodialysis: postoperative evaluation and function monitoring," *International urology and nephrology,* vol. 46, no. 2, pp. 403-409, 2014.
[86] P. W. Eggers, "Has the incidence of end-stage renal disease in the USA and other countries stabilized?," *Current opinion in nephrology and hypertension,* vol. 20, no. 3, pp. 241-245, 2011.
[87] R. Saran *et al.*, "Longer treatment time and slower ultrafiltration in hemodialysis: associations with reduced mortality in the DOPPS," *Kidney international,* vol. 69, no. 7, pp. 1222-1228, 2006.
[88] F. Tentori *et al.*, "Longer dialysis session length is associated with better intermediate outcomes and survival among patients on in-center three times per week hemodialysis: results from the Dialysis Outcomes and Practice Patterns Study (DOPPS)," *Nephrology Dialysis Transplantation,* vol. 27, no. 11, pp. 4180-4188, 2012.

[89] S. M. Brunelli, G. M. Chertow, E. D. Ankers, E. G. Lowrie, and R. Thadhani, "Shorter dialysis times are associated with higher mortality among incident hemodialysis patients," *Kidney international,* vol. 77, no. 7, pp. 630-636, 2010.

[90] J. P. Kooman, J. A. Joles, and K. G. Gerritsen, "Creating a wearable artificial kidney: where are we now?," *Expert review of medical devices,* vol. 12, no. 4, pp. 373-376, 2015.

[91] L.-A. Topfer, "Wearable artificial kidneys for end-stage kidney disease," *CADTH Issues in Emerging Health Technologies,* 2017.

[92] J. Himmelfarb and T. A. Ikizler, "Hemodialysis," *New England Journal of Medicine,* vol. 363, no. 19, pp. 1833-1845, 2010.

[93] J. E. Flythe, G. C. Curhan, and S. M. Brunelli, "Shorter length dialysis sessions are associated with increased mortality, independent of body weight," *Kidney international,* vol. 83, no. 1, pp. 104-113, 2013.

[94] J. E. Flythe, S. E. Kimmel, and S. M. Brunelli, "Rapid fluid removal during dialysis is associated with cardiovascular morbidity and mortality," *Kidney international,* vol. 79, no. 2, pp. 250-257, 2011.

[95] S.-H. S. Huang, L. E. Crowley, H. J. Jefferies, M. T. Eldehni, A. Odudu, and C. W. McIntyre, "The impact of hemodialysis on segmental and global longitudinal myocardial strain," *Canadian Journal of Cardiology,* vol. 30, no. 11, pp. 1422-1428, 2014.

[96] H. J. Jefferies, B. Virk, B. Schiller, J. Moran, and C. W. McIntyre, "Frequent hemodialysis schedules are associated with reduced levels of dialysis-induced cardiac injury (myocardial stunning)," *Clinical journal of the American Society of Nephrology,* vol. 6, no. 6, pp. 1326-1332, 2011.

[97] H. J. Jefferies, J. O. Burton, and C. W. McIntyre, "Individualised dialysate temperature improves intradialytic haemodynamics and abrogates haemodialysis-induced myocardial stunning, without compromising tolerability," *Blood purification,* vol. 32, no. 1, pp. 63-68, 2011.

[98] N. I. o. D. a. D. a. K. Diseases. "Kidney disease statistics for the United States . December 2016." https://www.niddk.nih.gov/health-information/health-statistics/kidney-disease (accessed.

[99] N. Kontodimopoulos and D. Niakas, "An estimate of lifelong costs and QALYs in renal replacement therapy based on patients' life expectancy," *Health Policy,* vol. 86, no. 1, pp. 85-96, 2008.

[100] M. L. Unruh *et al.*, "Effects of 6-times-weekly versus 3-times-weekly hemodialysis on depressive symptoms and self-reported mental health: Frequent Hemodialysis Network (FHN) Trials," *American journal of kidney diseases,* vol. 61, no. 5, pp. 748-758, 2013.

[101] F. O. Finkelstein *et al.*, "At-home short daily hemodialysis improves the long-term health-related quality of life," *Kidney international,* vol. 82, no. 5, pp. 561-569, 2012.

[102] F. T. Group, "In-center hemodialysis six times per week versus three times per week," *New England Journal of Medicine,* vol. 363, no. 24, pp. 2287-2300, 2010.

[103] A. Bonenkamp *et al.*, "Home haemodialysis in the Netherlands: State of the art," *Neth J Med,* vol. 76, no. 4, pp. 144-157, 2018.

[104] S. W. Klarenbach, M. Tonelli, B. Chui, and B. J. Manns, "Economic evaluation of dialysis therapies," *Nature Reviews Nephrology,* vol. 10, no. 11, pp. 644-652, 2014.

[105] W. G. Couser, G. Remuzzi, S. Mendis, and M. Tonelli, "The contribution of chronic kidney disease to the global burden of major noncommunicable diseases," *Kidney international,* vol. 80, no. 12, pp. 1258-1270, 2011.

[106] J. W. Agar, "Understanding sorbent dialysis systems," *Nephrology,* vol. 15, no. 4, pp. 406-411, 2010.

[107] F. Meng *et al.*, "MXene sorbents for removal of urea from dialysate: A step toward the wearable artificial kidney," *ACS nano,* vol. 12, no. 10, pp. 10518-10528, 2018.

[108] A. Gordon, M. A. Greenbaum, L. B. Marantz, M. J. McArthur, and M. H. Maxwell, "A sorbent based low volume recirculating dialysate system," *ASAIO Journal,* vol. 15, no. 1, pp. 347-352, 1969.

[109] R. Stephens, S. Jacobsen, E. Atkin-thor, and W. Kolff, "Portable/wearable artificial kidney (WAK)-initial evaluation," *Proceedings of the European Dialysis and Transplant Association. European Dialysis and Transplant Association,* vol. 12, pp. 511-518, 1976.

[110] R. Smakman and A. van Doorn, "Urea removal by means of direct binding," *Clinical Nephrology,* vol. 26, pp. S58-62, 1986.

[111] T. Alizadeh, "Preparation of molecularly imprinted polymer containing selective cavities for urea molecule and its application for urea extraction," *Analytica chimica acta,* vol. 669, no. 1-2, pp. 94-101, 2010.

[112] M. Kaneko, H. Ueno, R. Saito, S. Suzuki, J. Nemoto, and Y. Fujii, "Biophotochemical cell (BPCC) to photodecompose biomass and bio-related compounds by UV irradiation with simultaneous electrical power generation," *Journal of Photochemistry and Photobiology A: Chemistry,* vol. 205, no. 2-3, pp. 168-172, 2009.

[113] P. Bombelli *et al.*, "Quantitative analysis of the factors limiting solar power transduction by Synechocystis sp. PCC 6803 in biological photovoltaic devices," *Energy & Environmental Science,* vol. 4, no. 11, pp. 4690-4698, 2011.

[114] B. Liu and E. S. Aydil, "Growth of oriented single-crystalline rutile TiO2 nanorods on transparent conducting substrates for dye-sensitized solar cells," *Journal of the American Chemical Society,* vol. 131, no. 11, pp. 3985-3990, 2009.

[115] G. Wang *et al.*, "Hydrogen-treated TiO2 nanowire arrays for photoelectrochemical water splitting," *Nano letters,* vol. 11, no. 7, pp. 3026-3033, 2011.

[116] J. Balajka *et al.*, "High-affinity adsorption leads to molecularly ordered interfaces on TiO2 in air and solution," *Science,* vol. 361, no. 6404, pp. 786-789, 2018.

[117] G. Shao, Y. Zang, and B. J. Hinds, "TiO2 nanowires based system for urea photodecomposition and dialysate regeneration," *ACS Applied Nano Materials,* vol. 2, no. 10, pp. 6116-6123, 2019.

[118] G. Shao, J. Himmelfarb, and B. J. Hinds, "Strategies for optimizing urea removal to enable portable kidney dialysis: A reappraisal," *Artificial Organs,* 2022.

[119] G. Shao *et al.*, "Dialysate Regeneration with Urea Selective Membrane Coupled to Photoelectrochemical Oxidation System," *Advanced Materials Interfaces,* p. 2102308, 2022.